The University of Sheffield
Department of Mechanical Engineering

Shaken Baby Syndrome:- Simulation via Computational and Physical Modelling

---

PhD Thesis

By J. Cheng

Supervised by Professor I. C. Howard, Dr. A. Yoxall

May 2008

The University of Sheffield
Department of Mechanical Engineering

Shaken Baby Syndrome:- Simulation via Computational and Physical Modelling

PhD Thesis

By Jingjing Cheng

Supervised by Professor Ian C. Howard, Dr. Alaster Yoxall

May 2008

APPENDIX A: *ACCELEROMETER*

Accelerometer is a small device that measure acceleration. Figure A illustrates its principal of operation. It is attached on the target object with a small mass on a cantilever beam inside. The tiny deflection of the beam is related to the acceleration of the mass and can be detected by a set of strain gauges on the beams nearby while the target accelerating, and an electrical signal is produced and record for the deflection.

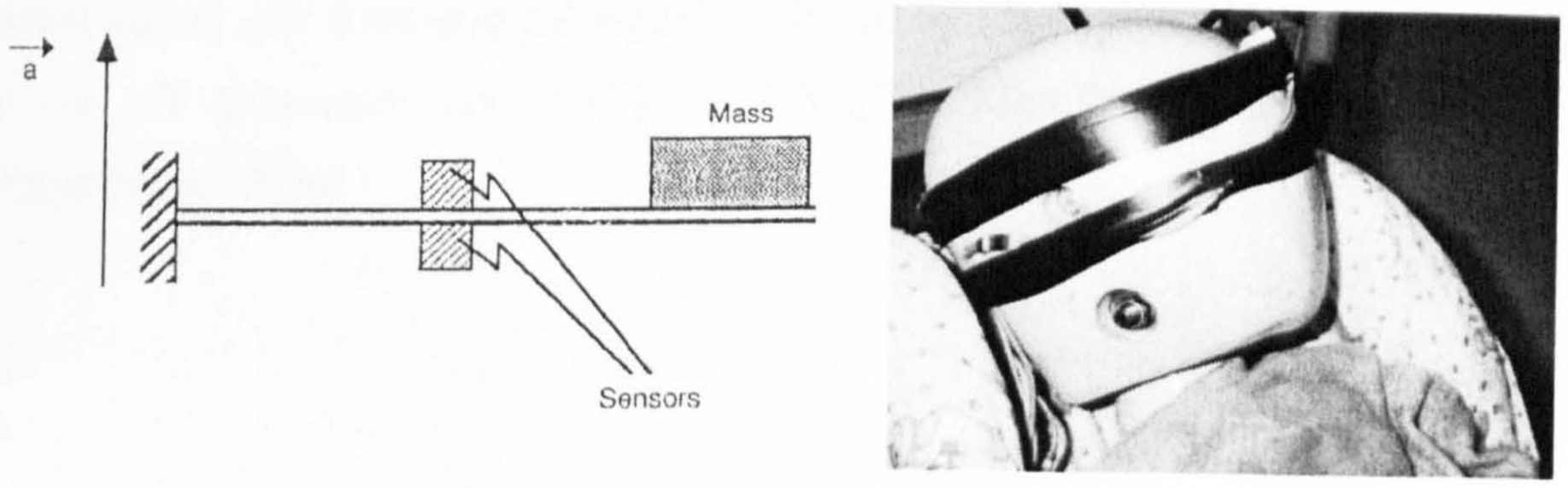

Figure A. Left, the principle of accelerometer. Right, the accelerometer's attachment on the dummy is demonstrated.

It always records the acceleration in local coordinate, which is fix on the object and moves with it.

Time integration of the acceleration signal yields the momentary velocity of the point. And a second time integration will lead to the spatial displacement of that point.

Accelerometer produces an alternative measurement for rigid body's position besides a whole position measurement system, with the advantages that it is easier to be operated and also reduces experiment cost.

However, four practical limitations of accelerometer have to be considered to prevent and reduce the inaccuracy for the experiment.

- The determination of the segment's initial conditions
- The effect of the field of gravity
- The segment rotational degrees of freedom
- Low-frequency drift

According to the TRL dummy, accelerometers sit in 4 positions with 8 direction measurements in local frame fixed on corresponding segments. Figure 4.1 and Table 4.1

give the position and measurements separately. The initial values of each segment's velocity and position are set to zero according to the digital camera that captures each full period motion of the shakes. The field of gravity does not be considered as it is supposed not to play an important role. The rotational degree of freedom of each segment is defined by the 8 measurements by the 4 place accelerometers with 2 significant assumptions made (Chapter 3). The low-frequency drift is detected in each output signal, and each original signal is filtered by Chebyshev high pass filter at 0.8 Hz as cut off frequency via MATLAB 6.5 (The MathWorks, Massachusetts, USA) (Oppenheim 1975).

APPENDIX B: *DESIGN OF A VIDEO RECOGNITION SYSTEM*

B.1. INTRODUCTION

Chapter 6 discussed the reconstruction of gelatine motion by analysing webcam images. The position of paper marker was defined by target the pixel in the centre of the marker manually via pixel picking software ImageTool 3.0 (*UTHSCSA*). Horizontal displacement dx and vertical displacement *dy* was reconstructed with the peak value of 2mm and 0.5 mm separately. The *dy* , with the variation of 1 pixel between its maximum value and zero position, was not accurate enough. This can be caused by either the illumination of the image or the size and the low detection of the marker by the software. The improving method is going to be taken based on these two main causations.

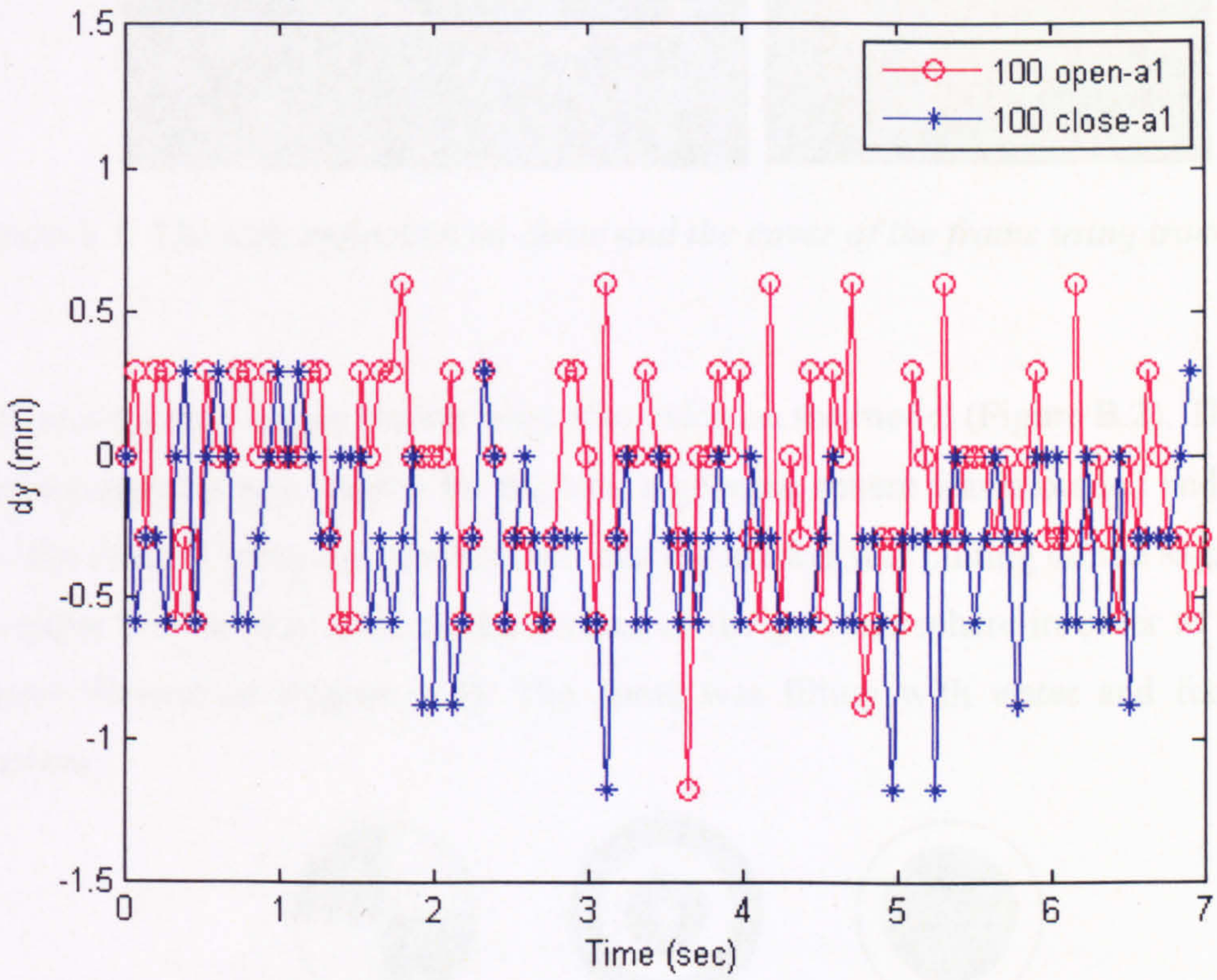

Figure B.1 The vertical gelatine displacement dy reconstructed from webcam by ImageTool 3.0 (UTHSCSA) of 100mm dome.

An attempt was made to investigate and design a video recognition system, which was also a final year undergraduate project (Schunck, 2007).

B.2. METHOD

Several improvements were given to the current motion capturing system. The existing video camera was kept while the image resolution increased to 640×480 instead of previous 320×240 pixel to increase the number of pixel within the same detection area. Custom developed video recognition software by University of Sheffield was introduced. It required the image captured by webcam with better contrast without able to be adjusted by setting the different parameter in Logitech software, and light reflection was blocked by the using the tracing paper to cover the frame (Figure B.1).

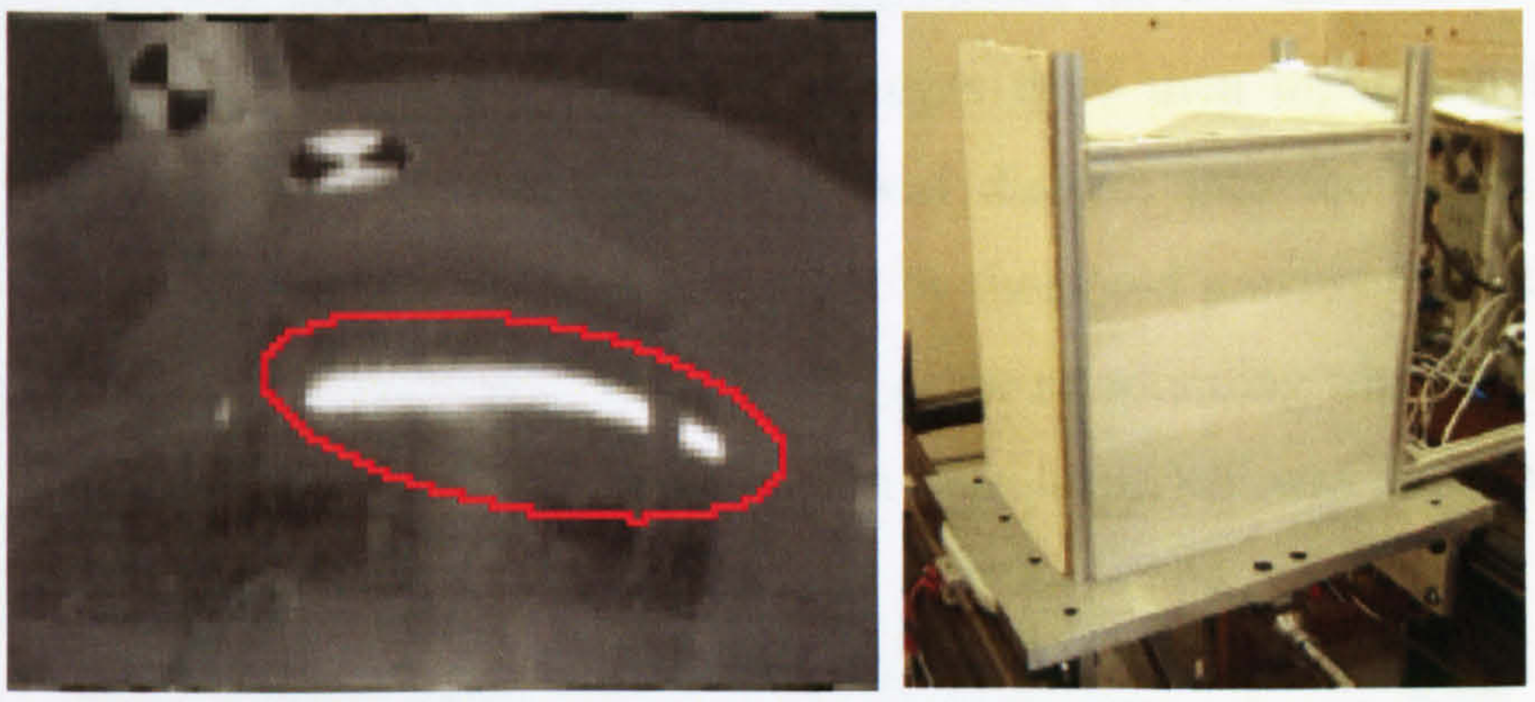

Figure B.1. The light reflection on dome and the cover of the frame using tracing paper.

Two new types of paper marker were also using on the model (Figure B.2). The 100mm closed top dome was chosen for the test, a gelatine sphere was moulded and assembly into the dome. Unlike the previous test that the marker was putting on the sagittal plane, the paper marker was stick on the surface of the gelatine sphere in order to obtain the clearer illustration (Figure B.4). The dome was filling with water and fixed on the platform.

Figure B.2. From left to right: The previous marker in Chapter 5, the second marker, and the third marker using for current video recognition system.

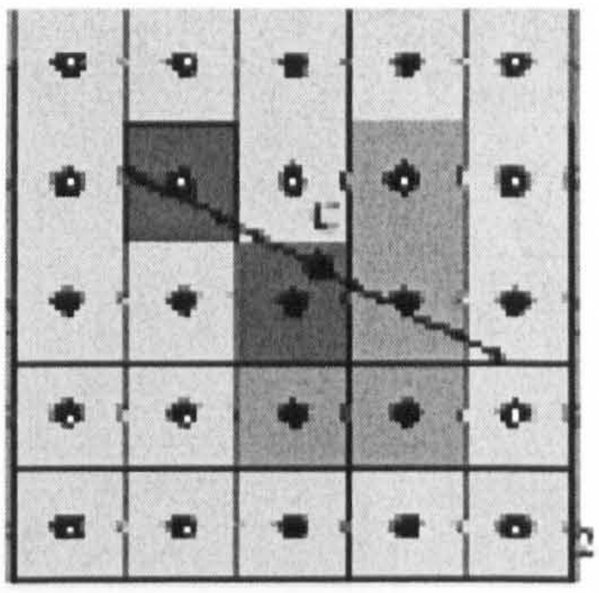

Figure B.3. The edge tracing method.

A constant repetitive shaking was applied to the model, the top and lateral views were captured separately by two webcams. The images were then input into the custom designed software. The images information was discrete into the black and white contrast pixel. The edging tracking was applied by threshold processing in the imaging analysis to selecting the black area while get rig of the surrounding white area by setting up threshold (Figure B.3). The centre position of the marker was calculated and its position was able to be defined.

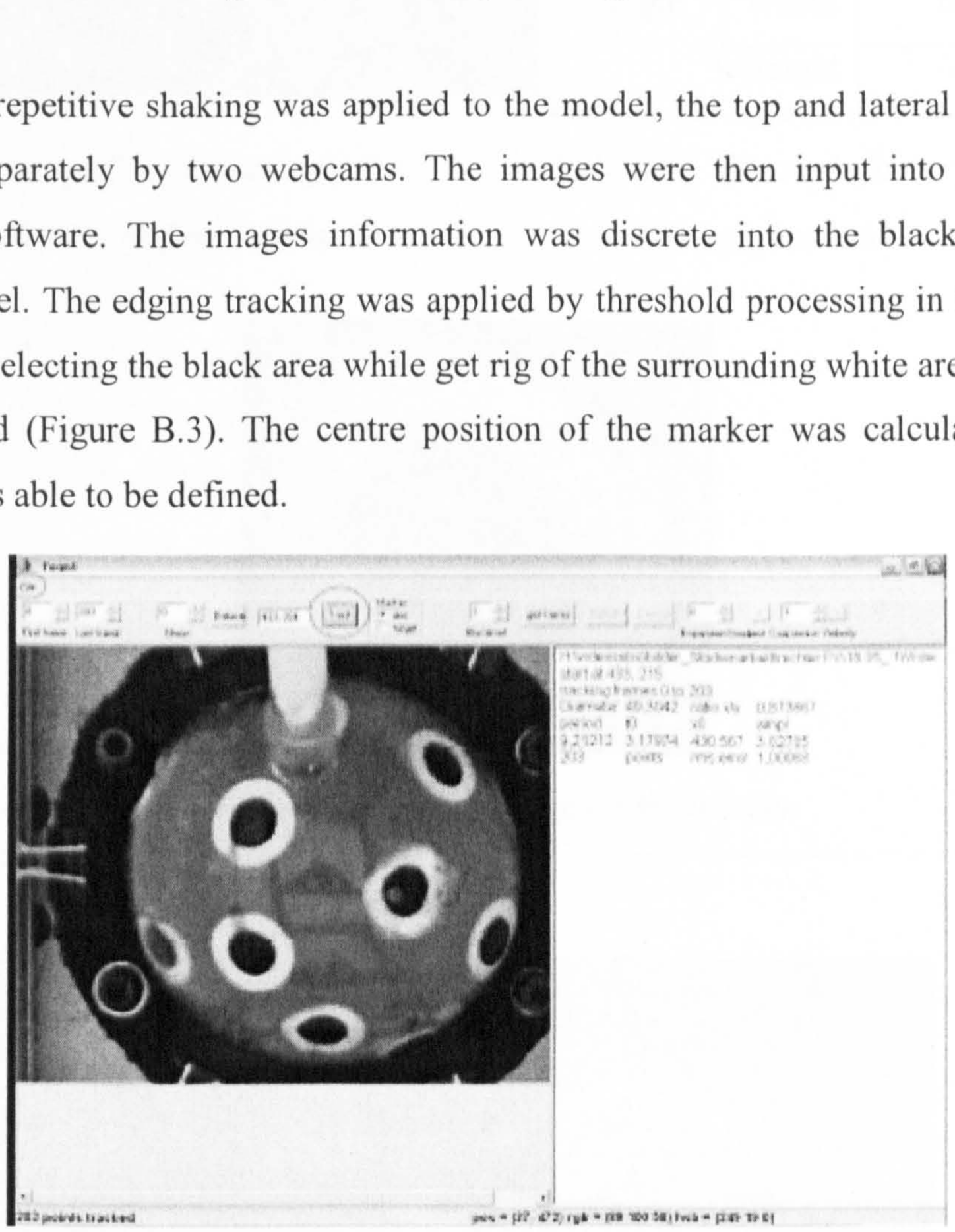

Figure B.4. Screenshot of the custom designed software

B.3. Result And Discussion

The scale factor between pixels and real distance in was calculated (Figure B.5). Table B.1 demonstrated the scale factor of three webcams. Figure B.6-B7 shows the tracing result of top view marker position during on shaking test on closed dome model.

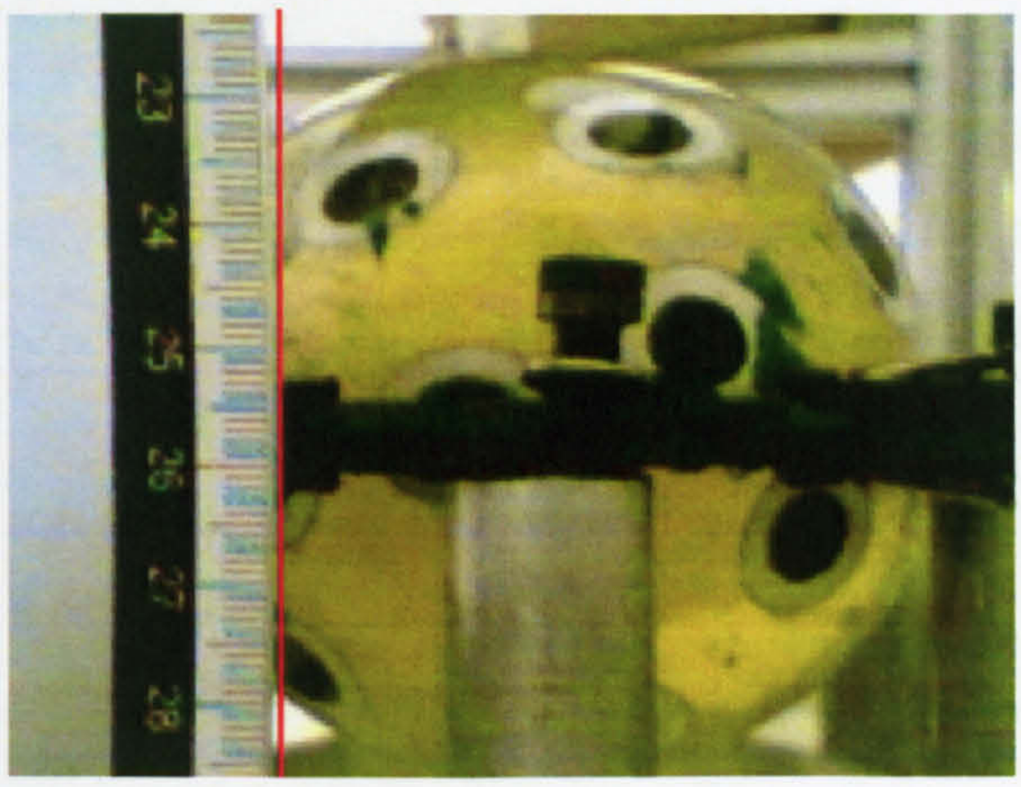

Figure B.5. The scale factor between pixel and dimension.

Camera		Scale Factor (mm/pixel)
Top	Width	0.178
	Height	0.177
Lateral	Width	0.129
	Height	0.100
Angle	Width	0.078
	Height	0.098

Table B.1. The scale factor for three camera view.

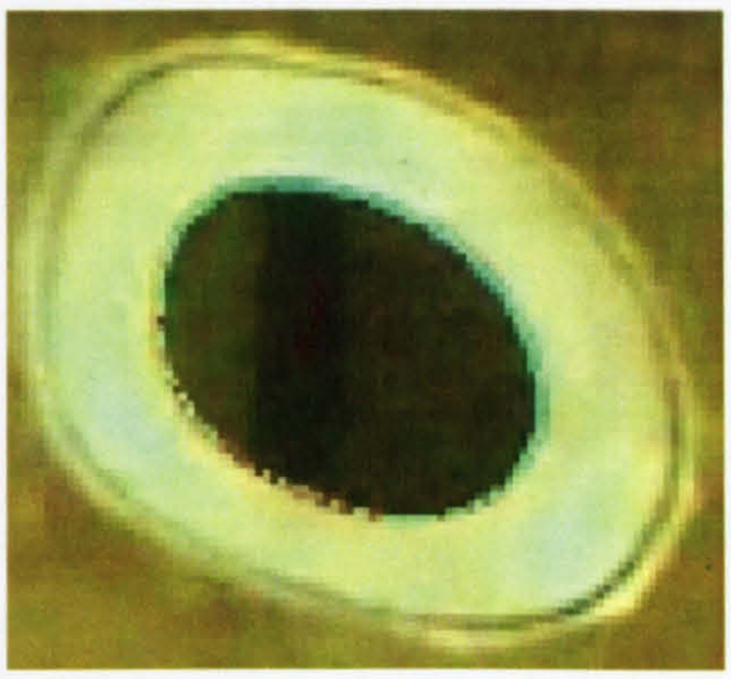

Figure B.6. The edge tracing on the marker.

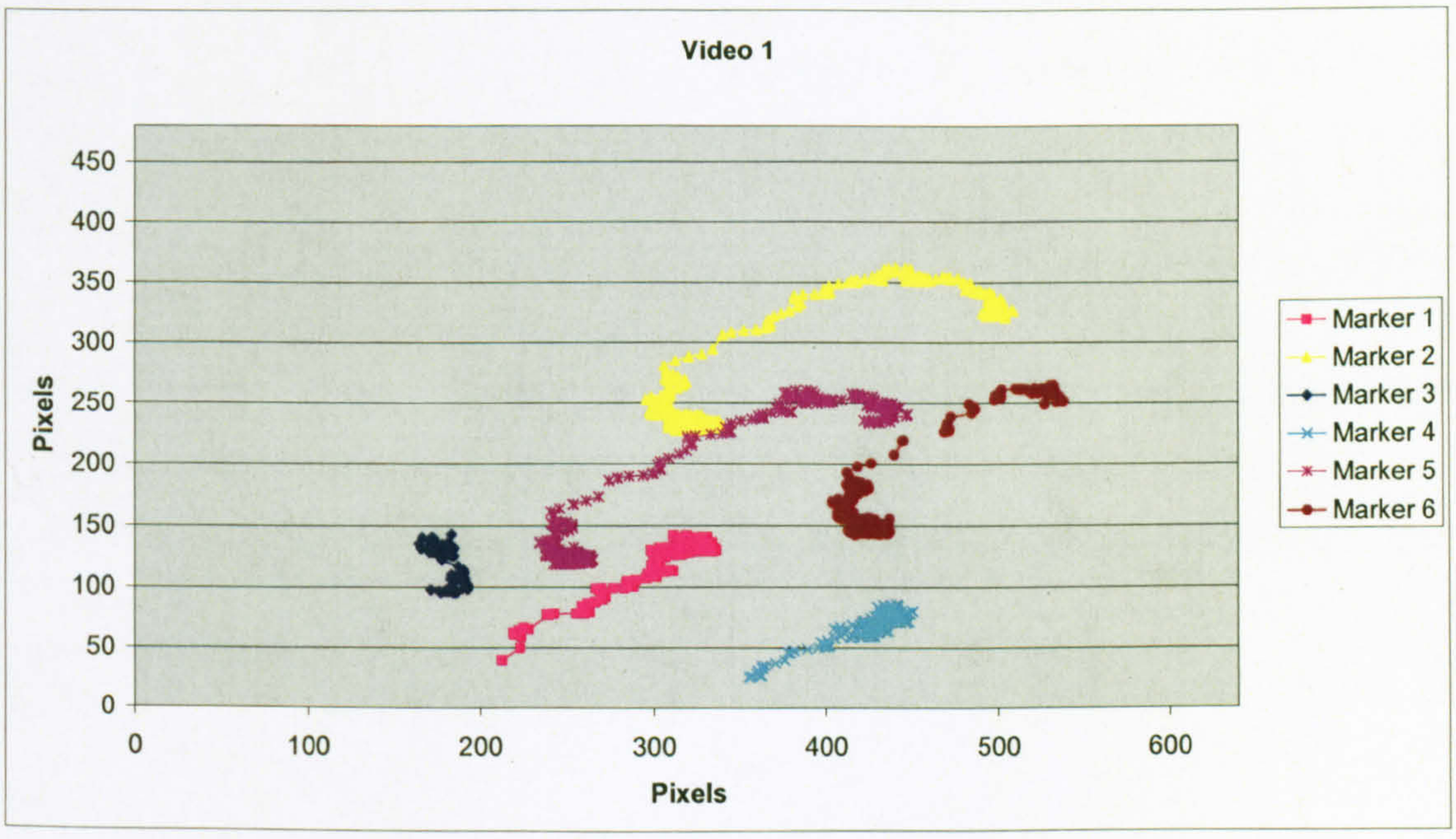

Figure B.7. The position of seven markers from the top view.

The shape of the position trace shows the jelly's motion was not only along a straight line in shaking direction, but also whiplash in the other side.

The edging tracing method shows a good competency to capture the centre marker position, and was also able to process the large amount of image data more effectively than manual picking. This test for the first time shows the possibility that to introduce the custom designed software into image analysis for shaking test rig. The jelly and soft membrane in physical head model requires high quality imaging recognition to reconstruct its deformation in both 2D and 3D direction, the custom designed software was considered to be one of the possible approaches. Future experiments are needed to study these cases.

APPENDIX C: *ANTHROPOMETRY OF INFANT SKULL MEASUREMENT*

C.1. INTRODUCTION

Measurements of infant skull from newborn to 12 months was made by normal physical measurement as well as photograph on several models to acquire two dimensional morphologic information (Hall, Froster-iskenius et al. 1995). A three dimensional CT scan afterward was given on one standard model to collect three dimensional morphologic information, in preparation for 3D numerical reconstruction (Hildebolt, Vannier et al. 1990).

C.2. BACKGROUND

Head injury is the most frequent cause of death in the paediatric population, of which under 1 year age (Geddes, Hackshaw et al. 2001), non accidental injury is the leading cause of injury deaths (Ommaya, Goldsmith et al. 2002). Investigation in paediatric head injury area has been carried on through both physical and biomechanical methodology. However, the disagreement rose between physician observation and biomechanician reconstruction is highly suspected due to the failure by some to acknowledge and incorporate known morphologic data and models into hypotheses regarding causes (Goldsmith and Plunkett 2004).

Three-dimensional information in high degree of precision on paediatric skull is urgent to be obtained in order to apply on both mechanical and computational model for further analysis (Spoor, Jeffery et al.; Levihn 1967; Vannier, Conroy et al. 1985; Hildebolt, Vannier et al. 1990).

C.3. GOALS

1. To get the measurement of six infant skull with normal physical anthropometric method (Hall, Froster-iskenius et al. 1995; Sinclair 1998).
2. To collect the morphologic information with high precision with 3D CT scan measurement.

C.4. METHOD

1. To get the normal measurements of head circumference, head length, head width, skull height, upper facial height, lower facial height, facial height, facial width by digital callipers.
2. To record two-dimensional morphologic information by taking the photograph through different degree of view e.g. top, lateral, anterior, posterior inside the calibration frame by digital camera.
3. To measure the anterior fontanelle size (the sum of the longitudinal and transverse diameters of the anterior fontanelle along the sagittal and coronal sutures) with ruler and the top view photograph.
4. To define the skull's age by the teeth.
5. Three-dimensional CT scan will apply on one or more models, and save the 3D morphologic information.

C.5. STAFF

- An executive student with mechanical engineering background to design and operate the progress.
- A staff from Department of Medical Physics to give the anatomical background knowledge support and validate the data during model measurement procedure.
- A staff from Department of Biomedical Sciences: to help to identify the skull age by the teeth, and validate the data during model measurement procedure.
- A radiographer from Academic Unit of Radiology, Division of Clinical Sciences to provide the technical assistant on CT scanner.

C.6. RESOURCES

- Equipment

  Digital camera, calibration frame (used for the background with calibration when taking pictures), micrometer, digital callipers, ruler, tape measure/calibrated metal tape, 3D CT scanner.

C.7. NOTES FOR MEASUREMENTS [FIGURE C.1]

- HEAD CIRCUMFERENCE C (MM)

From just above the galbella[1] area to opisthocranion[2], usually horizontal just above the eyebrow ridges when the patient looks straight ahead.

- HEAD LENGTH L (MM)

Maximum dimension of the sagittal axis of the skull, between the glabella and the opisthocranion.

- HEAD WIDTH W (MM)

Maximal biparietal diameter, between the most lateral points of the parietal bones (eurion) on each side of the head.

- SKULL HEIGHT H (MM)

Distance from nasion[3] to vertex[4]. Measure from the depth of the nasal root to the superior-most point of the skull in the vertical plane.

- FACIAL HEIGHT h_1 (MM)

Distance from nasion to menton[5] or gnathion[6], measure from the root of the nose to the inferior border of the mandible in a vertical plane.

- UPPER FACIAL HEIGHT h (MM)

Distance from nasion to subnasion[7], measure from the deepest part of the nasal root to the deepest point of concavity at the base of the nose, in a vertical plane.

- LOWER FACIAL HEIGHT h_2 (MM)

Length of the lower one-third of the craniofacies, measure from the base of the nose (subnasion) to the lowest median landmark on the lower border of the mandible.

---

[1] Galbella-The most prominent point on the grontal bone above the root of the nose, between the eyebrows.
[2] Opisthocranion-The most prominent portion of the occiput, close to the midline on the posterior rim of the foramen magnum.
[3] Nasion-The root of the nose.
[4] Vertex-The highest point of the head.
[5] Menton-The lowest median landmark on the lower border of the mandible.
[6] Gnathion-the most inferior point of the mandible in the midline.
[7] Subnasion-The base of the nose.

- FACIAL WIDTH W_f (MM)

The maximal distance between the most lateral points on the zygomatic arches[8] (zygion). Measure between the most lateral points of the zygomatic arches (zygion), localized by palpation.

- ANTERIOR FONTANELLE SIZE AC+BX(MM)

The sum of the longitudinal and transverse diameters of the anterior fontanelle along the sagittal and coronal sutures. The index finger should be placed as far as possible into each of the four corners of the anterior fontanelle, the positions may be marked with a dot distal to the finger tip. The longitudinal and transverse diameters may be measured directly or on a piece of white paper firmly pressed over the fontanelle. The points are joined to form a quadrilateral and the sum of the longitudinal and transverse diameters along the sagittal and coronal sutures can be measured.

C.8. RESULT AND DISCUSSION

Figure C.2 shows the skull sample that is under the measurement. Six skulls was given measurement follow the procedure and method mentioned in previous section. Each skull was taken photos after measuring. Table C.1 gives the skull dimension for all six models and its predicted gestation week. Table C.2 gives the measurement of anterior fontanelle of three skull samples. Table C.3 shows the thickness of the skull bone and dehydration dura of three skull samples. The result supports the geometrical construction of the finite element model discussed in this thesis.

Name	Head Circumference (C/mm)	Head Length (L/mm)	Head Width (W/mm)	Gestational age(weeks)			
				C	L	W	Average
S37	302	96.28	83.04	32.2	32.3	34.2	32.9
MEA	297	92.29	86.65	31.6	31.2	35.3	32.7
S3	335	97.78	86.15	38.4	32.5	35.2	35.3
S6	332	107.12	90.36	37.7	34.6	37.0	36.4
S7	332	112.27	91.28	37.7	40.0	37.8	38.5
S5	333	109.80	95.69	37.8	37.8	41.0	38.9

Table C.1 Skull measurement.

[8] Zygomatic arches- the slender arch formed by the temporal process of the cheekbone that bridges to the zygomatic process of the temporal bone.

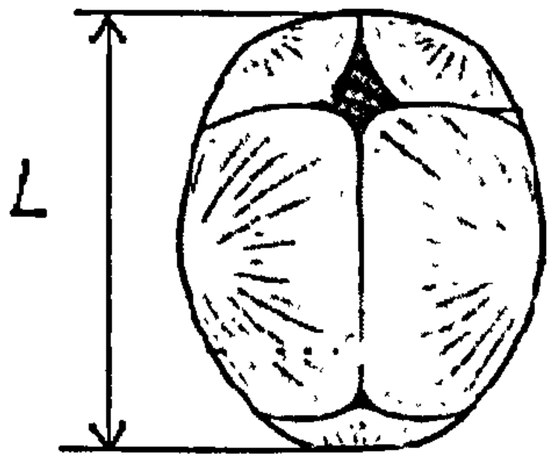

Head Length L(mm)

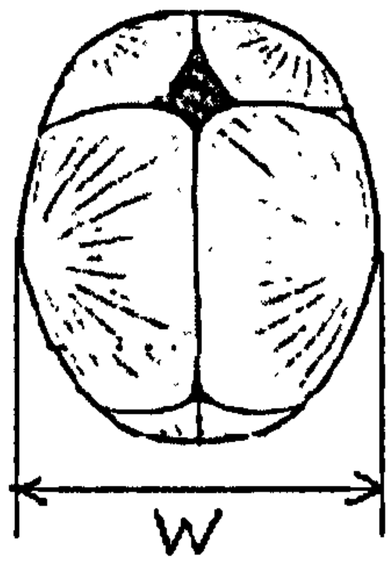

Head Width W(mm)

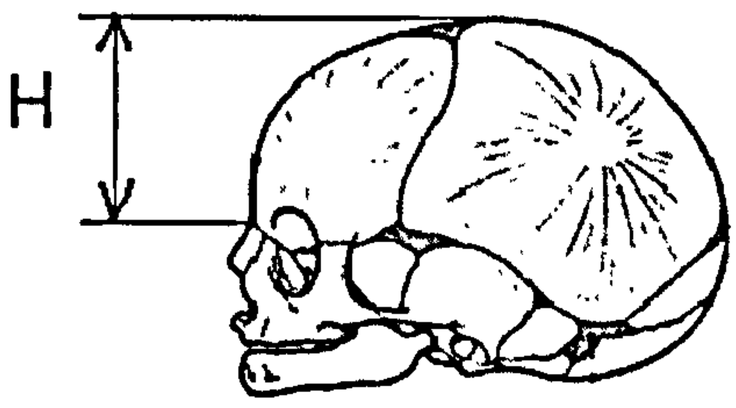

Skull Height H(mm)

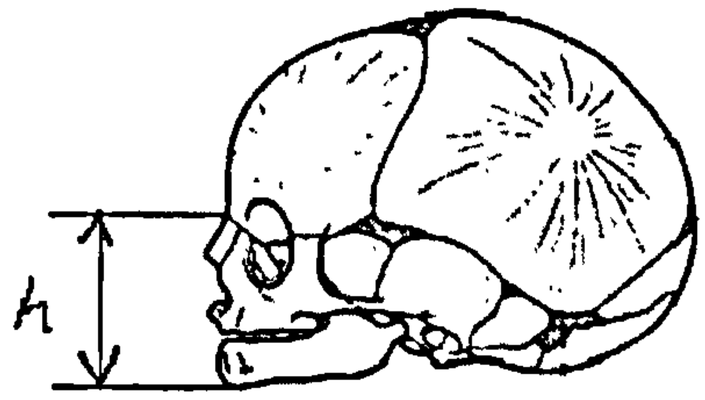

Facial Height h(mm)

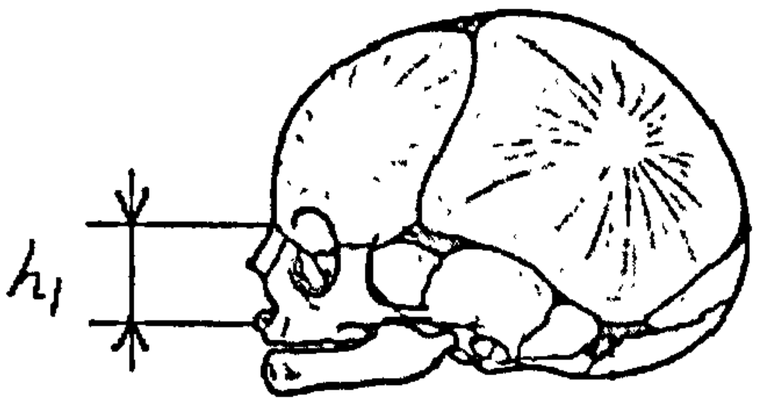

Upper Facial Height h_1(mm)

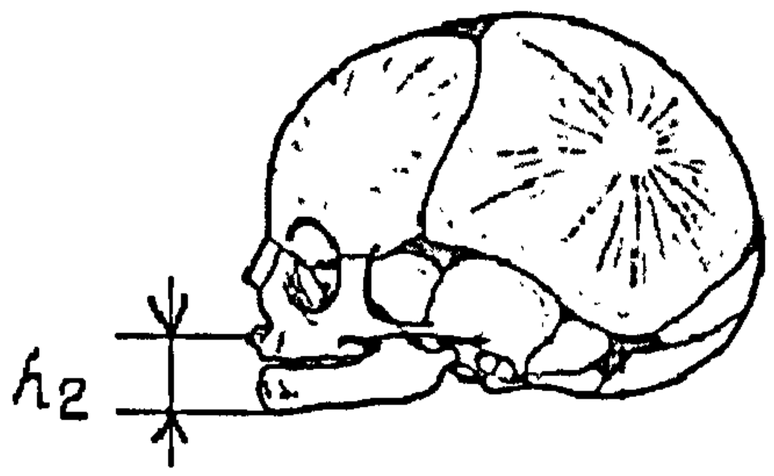

Lower Facial Height h_2(mm)

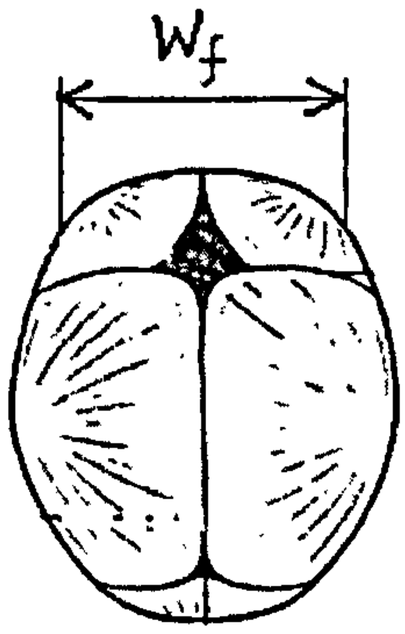

Facial Width W_f(mm)

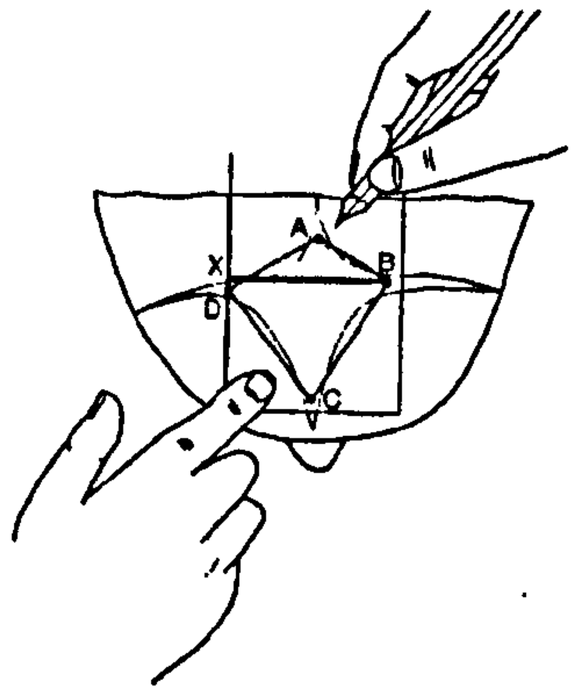

Anterior Fontanelle Size AC+BX(mm)

Figure C.1. The measurement diagram of the infant skull.

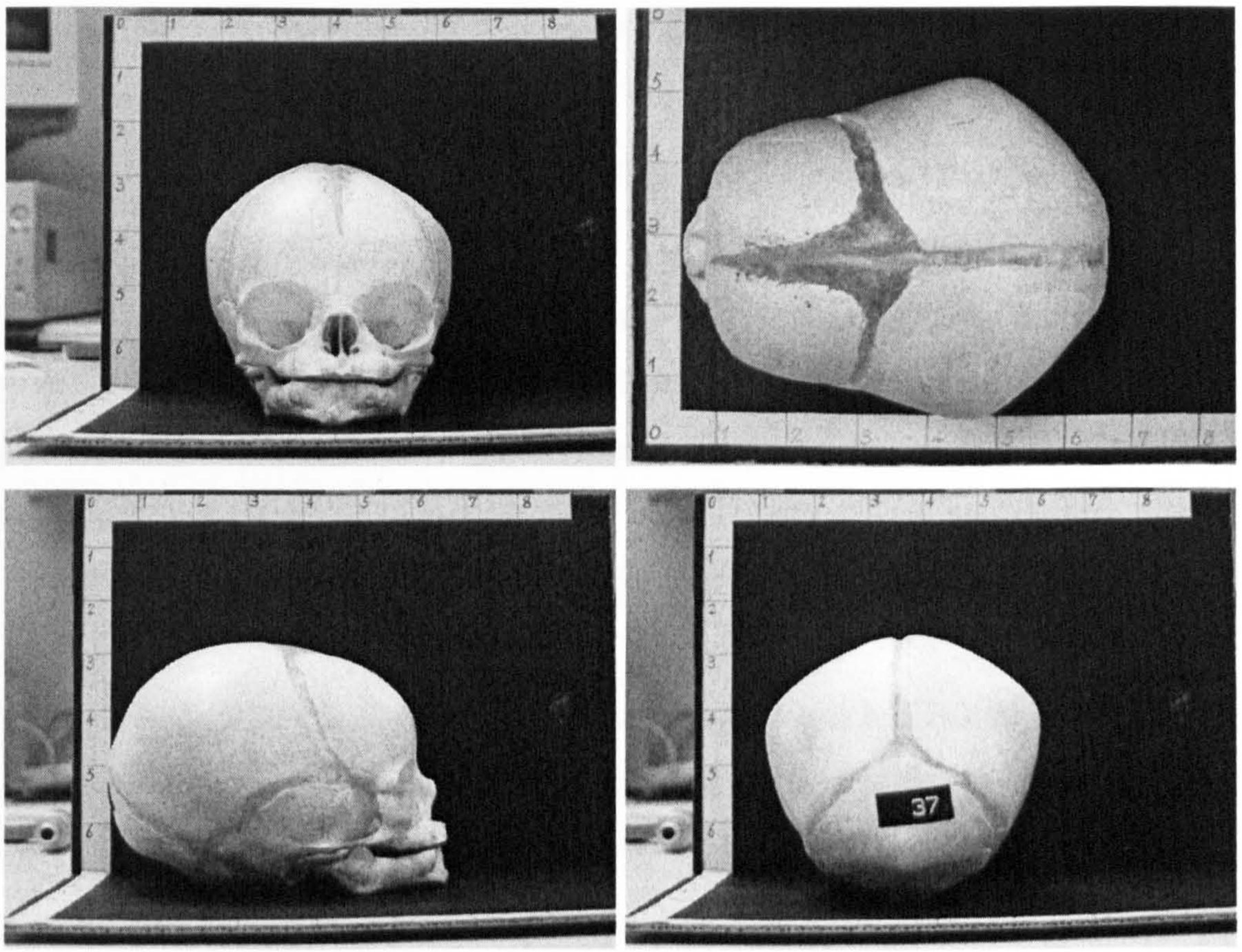

Figure C.2. Photo of the skull sample S37.

Name	AD	BX	AD+BX
S37	32.36	26.30	58.66
MEA	13.40	15.11	28.51
S3	9.86	8.82	18.68

Table C.2 Fontanelle measurement.

No.	Skull (T_{sk}/mm)	Dura (T_d/mm)
1	1.415	0.48
2	1.000	0.42
3	1.415	0.53

Table C.3 Skull and dural thickness measurement.

APPENDIX D: *HUMAN HEAD ANATOMY AND TISSUE MATERIAL PROPERTY*

D.1. THE CRANIAL CAVITY (McMinn et al. 1994; Schwartz 1995; Berkovitz and Moxham 1998)

The cranial cavity contains the centre nervous system of brain, the cranial nerves, meninges, and CSF. It can be divided into three distinct regions called fossae: The anterior fossae, middle fossae and posterior cranial fossae with marked step-like appearance (Figure D.1).

The anterior cranial fossae, which is formed by the orbital parts of the frontal bone, contains mainly the cerebral hemispheres of the brain.

The middle cranial fossae consist of a central, a right and left lateral parts. The central part is occupied mainly by the pituitary gland and the lateral parts contain the temporal lobes of the cerebral hemispheres of the brain.

The posterior cranial fossa is formed by parts of the occipital bone. Unlike the other two cranial fossae, the posterior cranial fossa has a well-defined roof, which is formed by a fold or septum of dura mater called the tentorium cerebelli. It contains the lowest part of the midbrain and the pons, cerebellum and medula oblongata. The region of the cranial cavity immediately above the tentorium cerebelli contains the occipital lobes of the cerebral hemispheres of the brain.

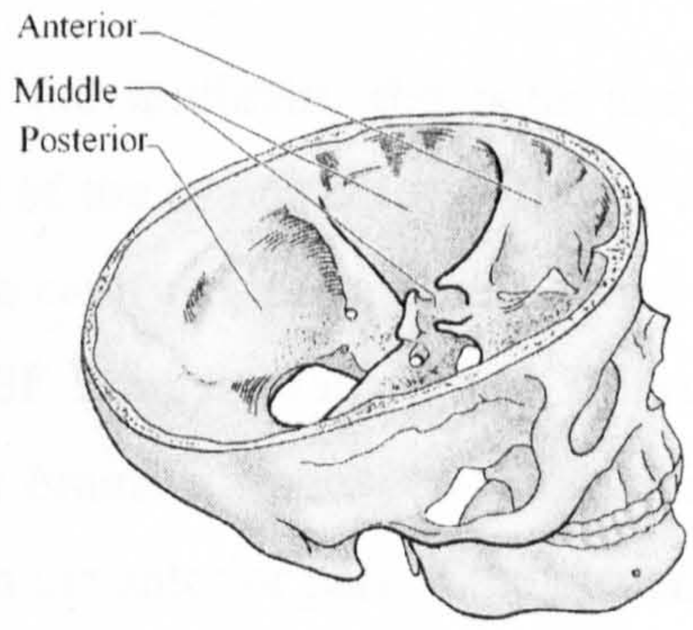

Figure D.1. *Superolateral view of the cranial fossa.*

D.2. THE BRAIN TISSUE (Moore 1999)

The brain is a complex rheological substance that is lodged in the cranial cavity with the premeated CSF and pervasive vasculature system. It is composed of the cerebrum, cerebellum, and brainsterm (Figure D.2).

The cerebral hemispheres and diencephalon construct the cerebrum. The cerebral hemisphere, which is occupying the anterior and middle cranial fossae and extending posteriorly over the cerebella tentorium and cerebellum, is the largest part of the brain. It consists of frontal, parietal, occipital and temporal lobes and in each cerebral hemisphere, there is a cavities called lateral ventricle that forms the most important part of the ventricular system inside the brain. The diencephalon forms the central core of the brain and surrounds the 3rd ventricle, which is the cavity that forms the cavity between the right and left halves of the diencephalon.

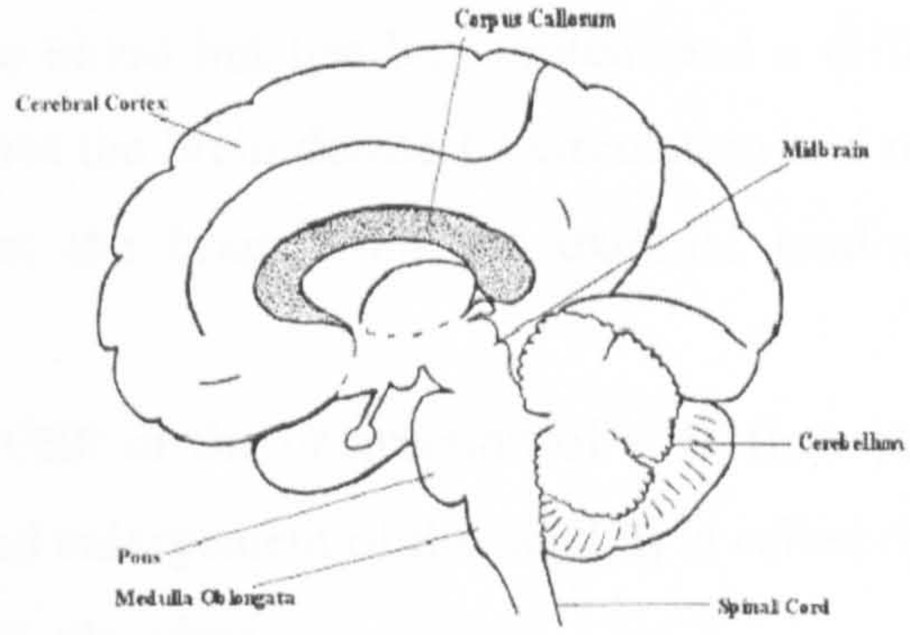

Figure D.2. *Major parts of the brain including cerebrum, cerebellum and brainstem.*

Cerebellum is the large brain mass lies beneath the cerebellar tentorium in the posterior cranial fossa. It consists of two lateral hemispheres united by a narrow middle part, the vermis.

The brainstem consists of the midbrain, the pons and the medulla oblongata. The midbrain is the rostral part of the brainstem that lies at the junction of the middle and posterior cranial fossae. The cavity of the midbrain forms the narrow canal (the cerebral aqueduct) that conducts CSF from the lateral and 3rd ventricles to the 4th ventricles. The pons is the part of the brainstem between the midbrain rostrally and the medulla oblongata caudally. It lies in the anterior part of the posterior cranial fossa. The cavity in the pons forms the superior part of the 4th ventricle. The medulla oblongata is in the posterior cranial fossa. It is the most caudal subdivision of the brainstem that is continous with the spinal cord. The cavity of the medulla forms the inferior part of the 4th ventricle. The base of the brain with the brainstem, there the medulla oblongata passes through the foramen magnum to become continuous with the spinal cord.

D.3. THE CEREBROSPINAL FLUID (CSF)

The CSF is a clear liquid enclosed in the meninges of the brain. It is secreted by the choroid plexuses of the four ventricles inside the brain, called the brain cavities. There are four cavities in total, two lateral ventricles in each cerebral hemisphere, 3rd and 4th ventricles connected by cerebral aqueduct (Figure D.3). The choroid plexuses from the lateral ventricles secreted the CSF, which passes through the 3rd and 4th ventricles with more produced joins in. It flows into the subarachnoid spaces and spinal cord, finally it is absorbed through the arachnoid granulation into the venous system. The constitution of the CSF is similar to blood but has less protein and a different ion concentration. Histologically it nourishes the brain during its circulation and mechanically it performs as a cushion to protect the brain from the external loading by either impact or acceleration.

The overproduction of CSF or the obstruction of CSF flow path will result in excess fluid in the ventricles and enlargement of the head. It is called dyhrocephalus and is one of the most common CSF disorders.

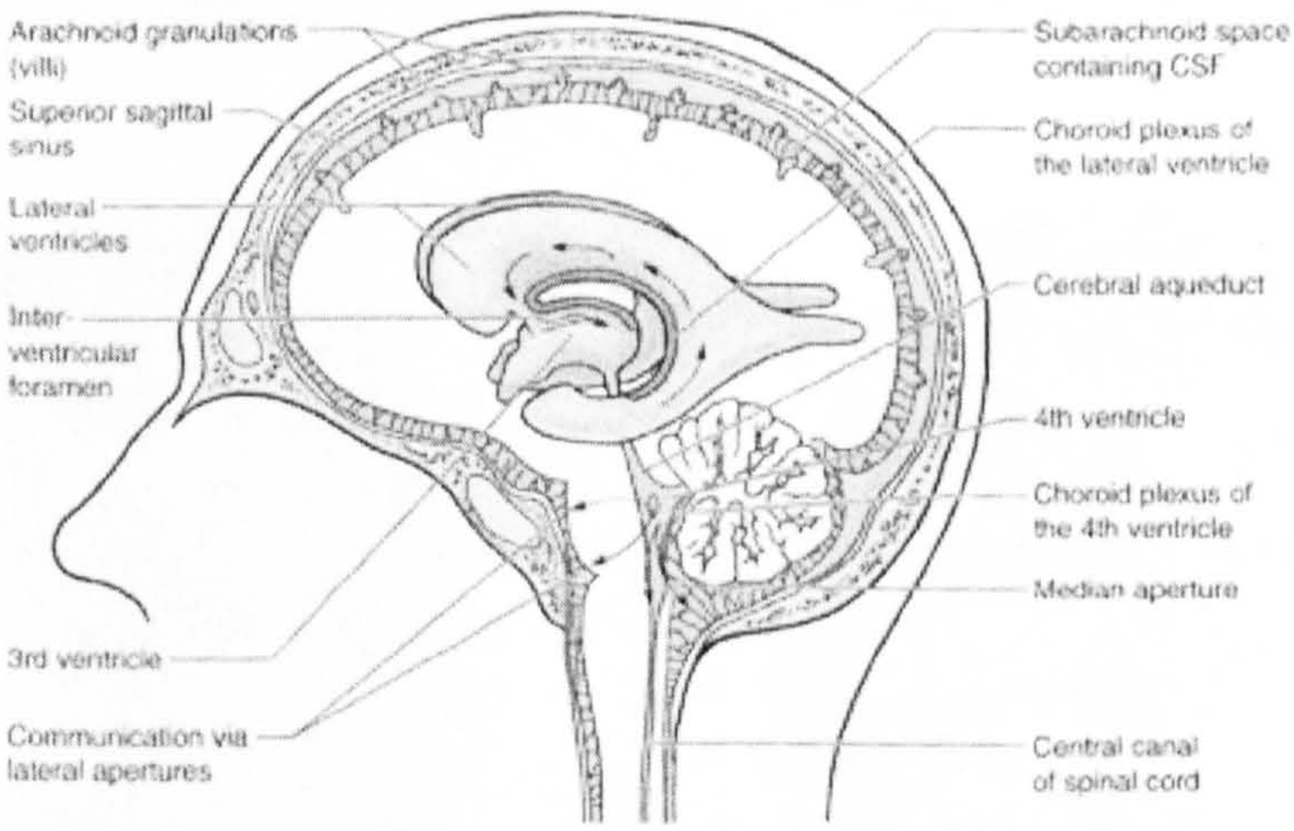

Figure D.3. *CSF circulation inside the cranium.*

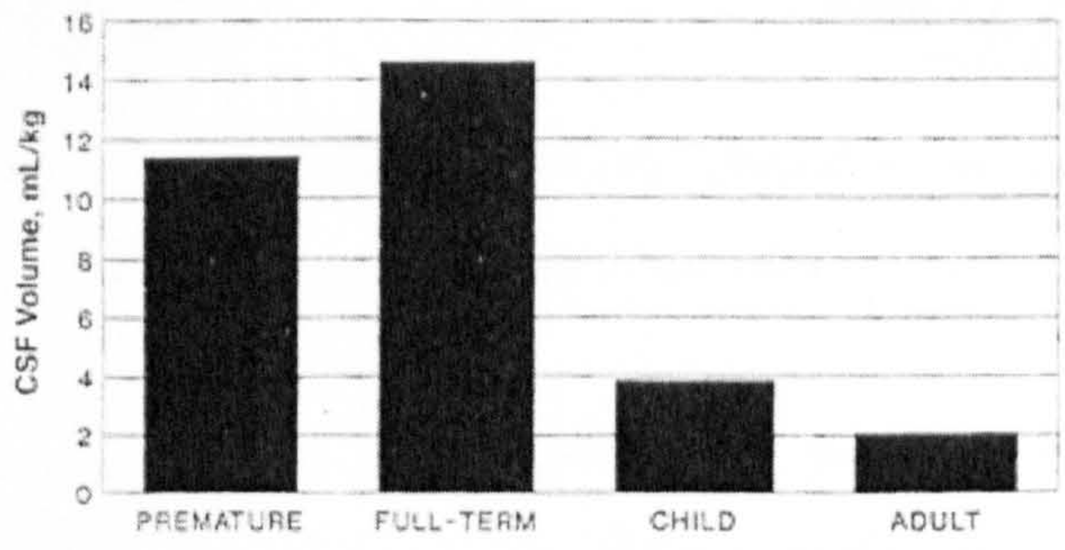

Figure D.4. *The human CSF volume per body weight is different with different age (Hayakawa, et al. 1993).*

The volume of the CSF is relative to weight and age. Premature and full-term infants have a much greater CSF volume relative to weight than a child or adult. Figure E.4 (Cote, et al. 2001) gives the human CSF volume related to weight of different age.

D.4. The Crebral Cortical Blood Vessels

The cerebral blood vessels are constituted with the cerebral arteries and the superficial cortical veins (Figure D.5). There are four major vessels entering the base of the skull, and then split into the cerebral arteries spreading over the cerebral hemisphere surface with in the subarachnoid space (Oka et al. 1985; Monson and Goldsmith2003). Similarly, the superficial cortical veins are form a net work over the cerebral hemisphere surfaces, and also these veins connect from the cerebral surfaces with the dural venous sinuses, through which the venous blood runs from the brain into the dura, and finally leaves the skull primarily through the jugular veins. Therefore, the cortical veins that embedded between cerebral cortex and the dura folds are also called "bridging veins".

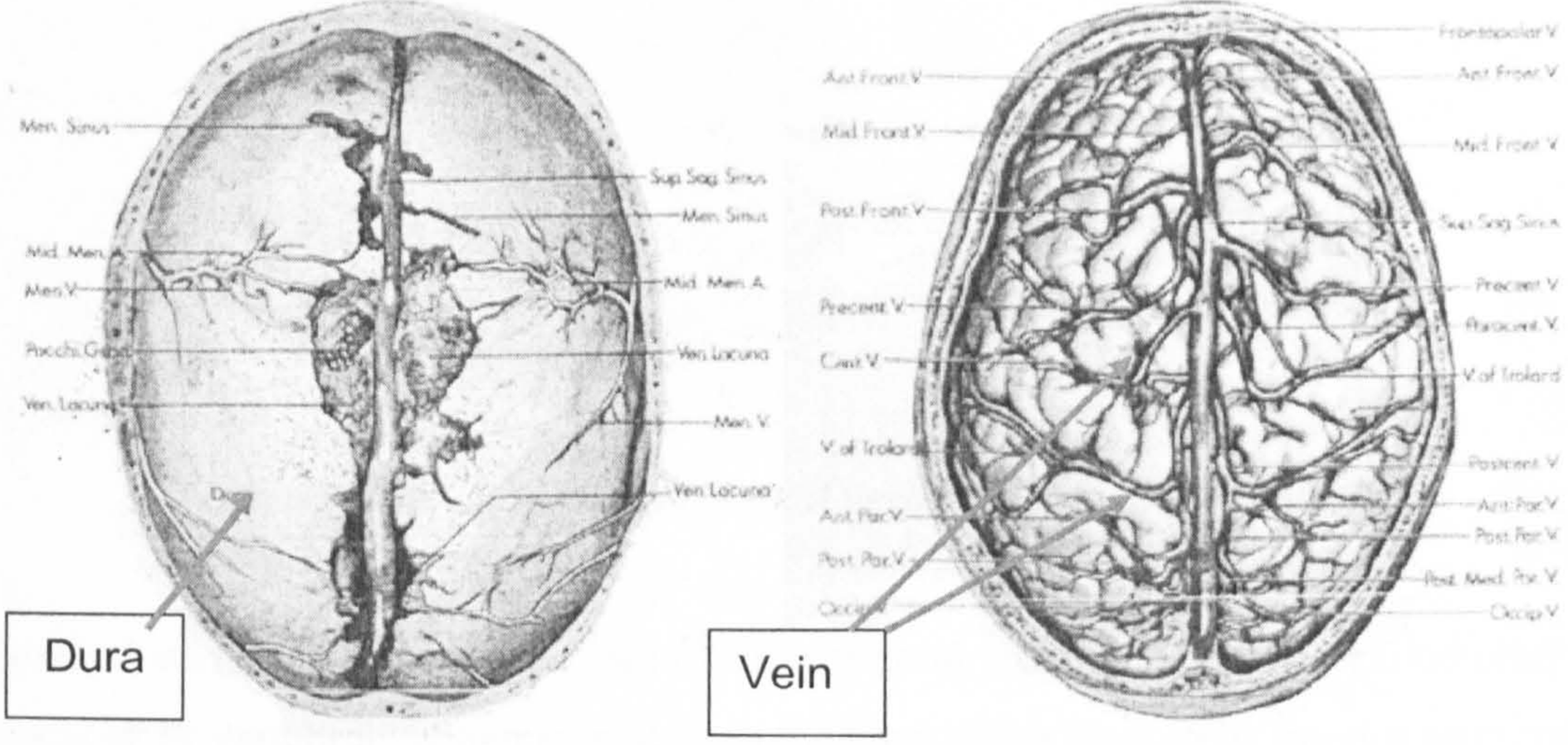

Figure D.5. *The diagram of main vasculature distributed on the dura and brain surface and connected to the supper sagittal sinus in the centre of cerebrum.*

Tearing of cerebral bridging veins is believed to be the main cause of the subdural haematoma (haemorrhage) (SDH) from the subtle to acute, with high mortality rate of 57-90% (Gennarelli and Thibault 1982). The relative motion between the brain and the skull during the rotational motion induced by either impact or impulsive loading always

causes the tearing of the bridging vessel, due to its thin thickness, circumferential arrangement of collagen fibres and lack of outer reinforcement.

Therefore the study of material properties of the human cerebral vessel was an essential biomechanical topic, not only to understand the injury limit of the vessel itself during the loading but also to learn the proper response of the brain under the rotational motion covered by the vasculature network.

D.5. THE NECK AND SPINAL CORD (Whiting 1998)

The neck is the structure link between the head and the trunk. It contains vascular, respiratory, nervous and endocrine that supported and the covered by the bones and muscles. The skeletal portion of the neck is the cervical vertebrae (Figure D.6).

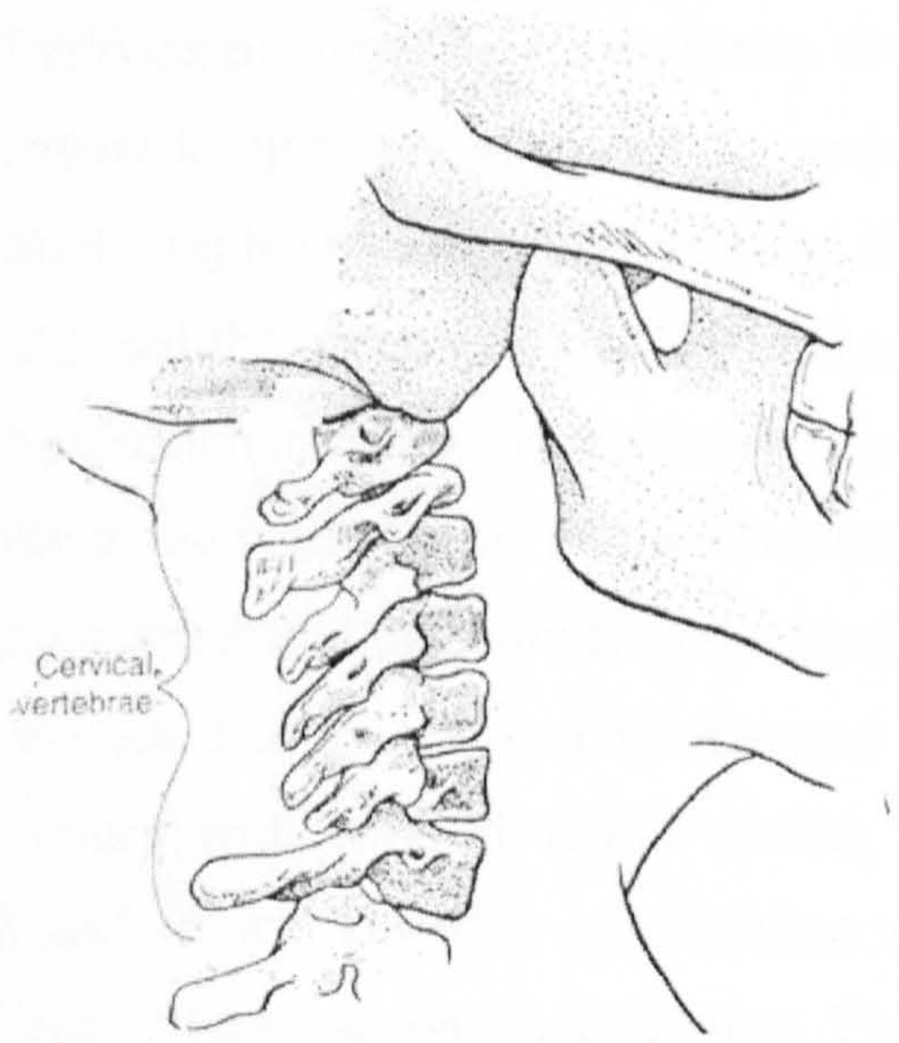

Figure D.6. *Diagram of cervical vertebrae that in human neck.*

Cervical vertebrae are the neck part of the vertebral column. The vertebral column is a group of 33 vertebrae, which extend from the base of the skull to its interior termination at the coccyx (tailbone). The five regions of the spine are: Cervical vertebrae (7), thoracic(12), lumbar(5), sacral (5 fused), coccygeal(4 fused).

The vertebral formen is an open passage that posterior to the verbral body, it houses the spinal cord. The spinal cord is the one with the greatest catastrophic potential that susceptible to injury of the cervical structures. The consequences of spinal cord damage range from mild as in neurapraxia to severe instances of paralysis or death.

D.6. THE INJURY MECHANISM OF THE NECK (Figure D.8)

Cervical spinal cord injury (SCI) may occur in many activities including motor vehicle accidents, which are considered to be the most common culpri, the falls from heights, work-related tasks, sporting activities, and shaking abusive injury. The mechanism of the cervical spine injuries can be divided into different causations by their mechanical properties: vertical compression, flexion-compression, compression-extension, tension, tension-extension, tension-flexion, torsion, horizontal shear, lateral bending, and other fractures. The flexion-compression is considered to be the most common injury mechanism. Classification of cervical injury mechanisms requires great care and precision because the possible discrepancy of the head motion related to the torso and the local motion between the spinal adjacent segments.

The whiplash injury is defined as the trauma causing cervical musculoligamental sprain or strain due to acceleration/deceleration of the head relative to the trunk in any plane. It is among the most common neck injury causation and the most misunderstood. Most of the whiplash injuries occur during the motor vehicle rear-end collision when the vehicle is violently pushed forward, and the occupant's torso is accelerated anteriorly while the head is forced into hyper-extension and then thrown forward into flexion. The direction of the whiplash is normally in the sagittal plane and is sometimes combined with lateral plane depending on different forces and the attitude of the head and neck. It is therefore a more complicated mechanism than the more straightforward impact or drop. The so-called shaking abusive injury with cervical failure during the autopsy is another example of the whiplash neck injury. The torso of the infant was gripped and shaking repetitively leaving the head suffers rotational acceleration. The weak infantile muscle, disability to control the head, and the possibly of torso-head impact always lead to fatal consequence for the infant though the loading magnitude is much smaller then vehicle collision.

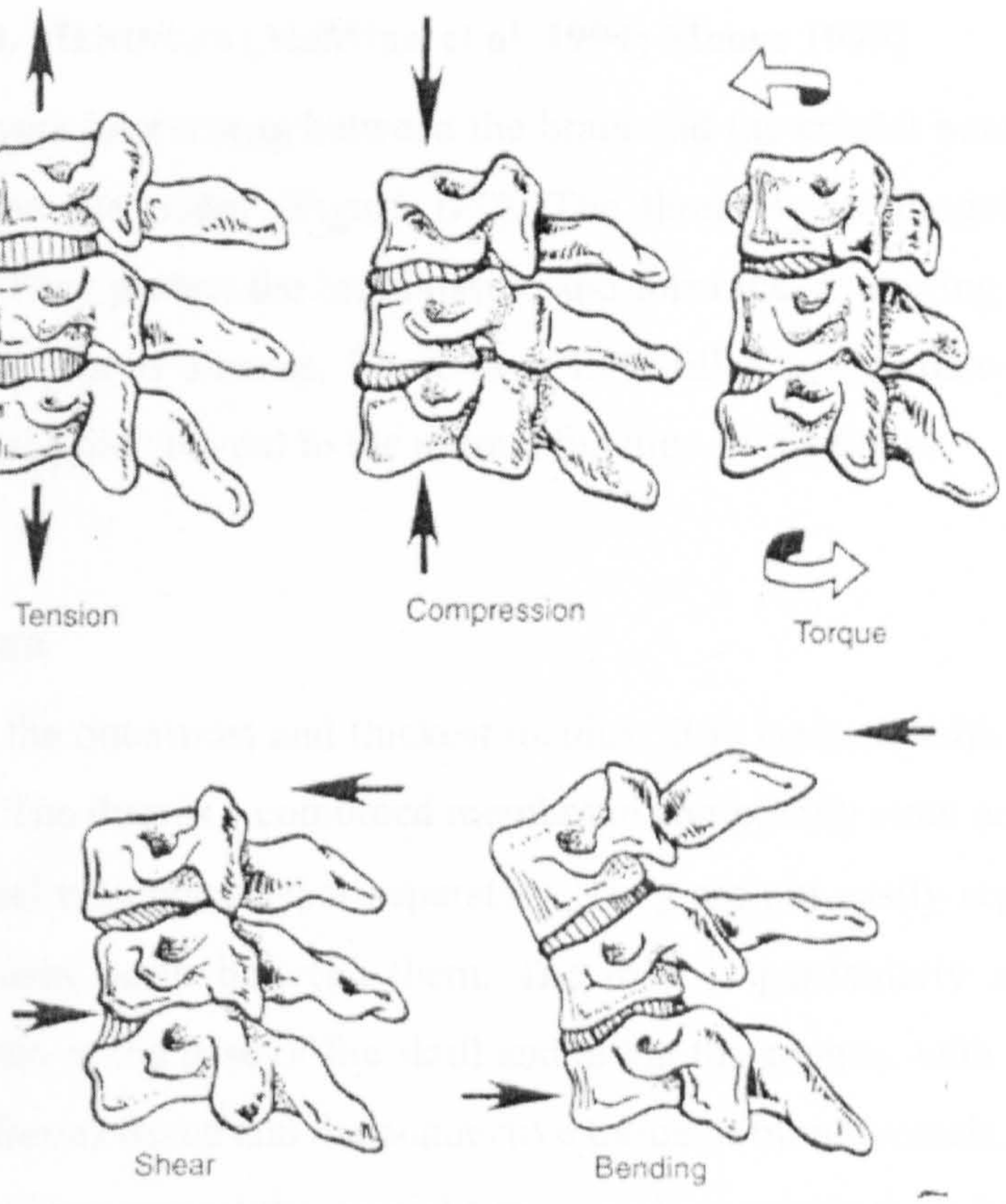

Figure D.7. *Mechanism of neck loading (Whiting 1998).*

D.7. THE MECHANICAL MODELLING OF THE HUMAN NECK

The complex structure of the neck gives no availability to construct a biofidelic neck (Wolfson 2004), especially for an infant. The anthropometrical dummy head in the biomechanical test is simplified as a solid form, rubber or kinematic hinge due to the absence of the detailed quantitative data of the infantile neck.

Duhaime (1987) constructed a one-month-old surrogate baby with stiff rubber, flexible rubber, and hinge neck separately. The acceleration from the impacts shows no difference between the necks, but the acceleration from the shake reveals an inverse relationship between the neck stiffness and time duration of a shake. The following published literature showed a very similar method to reconstruct the infantile neck. Prange (2003) used a hinged neck with negligible resistance in order to measurement a worst-case scenario. Wolfson (2004) produced a solid form neck with his dummy to collect the torso acceleration for further numerical analysis. Cory (2003) repeat Duhaime's test by using thick rubber, thin rubber, and hinge for the necks, and produced similar results with slightly hisher deformation.

D.8. THE CRANIAL MENINGES (McMinn et al. 1994; Moore 1999)

There are three layers intervening between the brain and the cranial bones: dura mater, arachoid mater, and pia mater (Figure D.9). The three layers altogether are called cranial meninges. They protect the brain tissue, and form the supporting framework for arteries, veins and venous sinuses. There is a fluid-filled cavity between called the subarachnoid space, which is vital to the normal function of the brain.

D.8.1. DURA MATER

The dura mater is the outermost and thickest meniux. It is inelastic with a high content of collagen fibres. The dura is a combined membrane comprising outer and inner layers, called endosteal and meningeal layer separately. They are not easily separable, except where venous sinuses occur between them. The dura is particularly adherent to the bones of the cranium at the base of the skull and along the sutures, with the attachment that mediated by fibrous tissue and the connective tissue of blood vessels.

The dura forms a sleeve around the cranial nerves and surrounds the whole of the optic nerve, becoming continuous with the sclera of the eyeball. The inner surface of the dura is smooth.

The meningeal layer (inner dura layer) forms four fibrous partitions or septa that broadly divide the cranial cavity. There are the large falx cerebri and tentorium cerebelli, and the smaller falx cerebelli and diaphragma sellae.

The falx cerebri is a sickle-shaped fold of dura. It lies along the median sagittal plane in the longitudinal fissure between the two cerebral hemispheres, and just above the corpus callosum. The tentorium cerebelli lies between the cerebellum and the occipital lobes of the cerebral hemispheres. The falx cerebelli is a small median fold at the back of the cranial cavity, which extends from the inferior surface of the tentorium cerebelli. Finally, the diaphragma sellae roofs the sella turcica.

D.8.2. THE ARACHNOID MATER AND SUBDURAL SPACE

The arachnoid mater closely lines the dura mater, being separated by a potential space called the subdural space. The subdural space is in continuity with the lymph spaces of the cranial and spinal nerves, and it contains a thin film of serous fluid. The arachnoid mater resembles the dura mater rather than pia mater.

D.8.3. THE SUBARACHNOID SPACE

Between the arachnoid and pia mater, there is a variable space called the subarachnoid space. It is filled with cerebrospinal fluid and contains the major arteries and veins supplying the central nervous system. The arachnoid is connected to the pia mater by a close meshwork of fine trabeculae. It forms virtually with pia mater a single membrane called pia-arachnoid due to its close to the pia mater. The subarachnoid space is in communication with the brain ventricles via the three apertures of the fourth ventricle, so that the CSF is able to drain from the ventricles into the subarachnoid spaces.

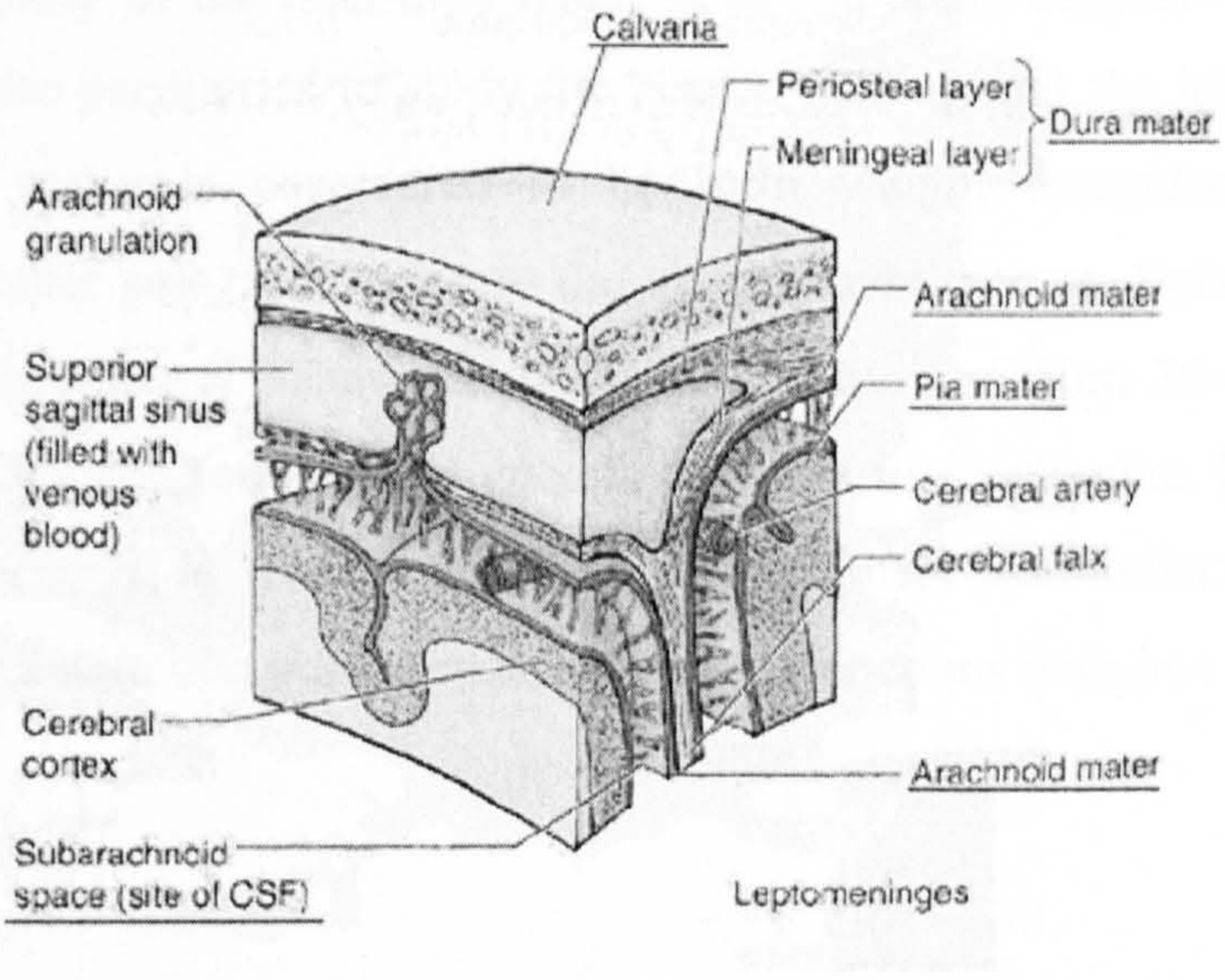

Figure D.8. *Diagram of cranial meninges including 3 major layers, Dura Mater, Arachnoid mater and Pia mater.*

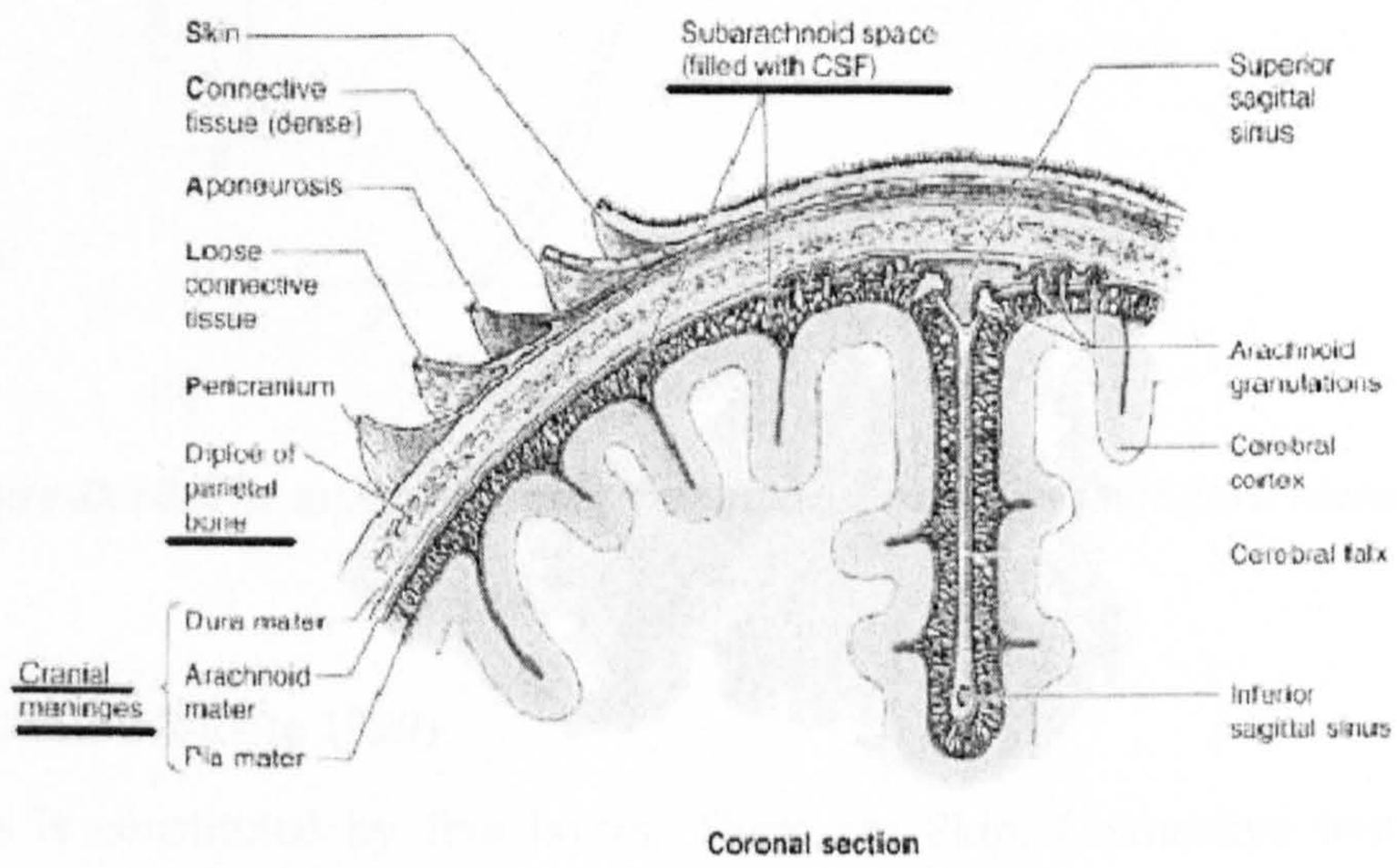

Figure D.9. *A Diagram shows the human scalp, cranium and cranial meninges.*

D.8.4. THE PIA MATER

The pia mater is a vascularised, areolar membrane that covers almost the whole external surface of the brain. It extends into every sulcus and fissure by intimate contact with the brain. The pia mater forms the roof of the third ventricle and the interior part of the fourth ventricle.

D.8.5. THE MATERIAL PROPERTY OF THE FETAL DURA MATER

The material property of the fetal dura mater is an important subject beside the fetal cranial bone for the paediatrics to study the head moulding and the injury during the birth. The dura mater is considered to be birth weight dependent, anisotropic, viscoelastic like other soft tissues due to the various publications. Bylski et al. 1986) investigated the mechanical behaviour of the fetal dura that from 30-42 weeks died infants. A biaxial tension test was designed to simulate the constraints imposed on the membrane by the cranial bones. The results reveal nonlinear load-deflection behaviour, and were compared with two published strain energy functions with one correlated well (Figure D.11).

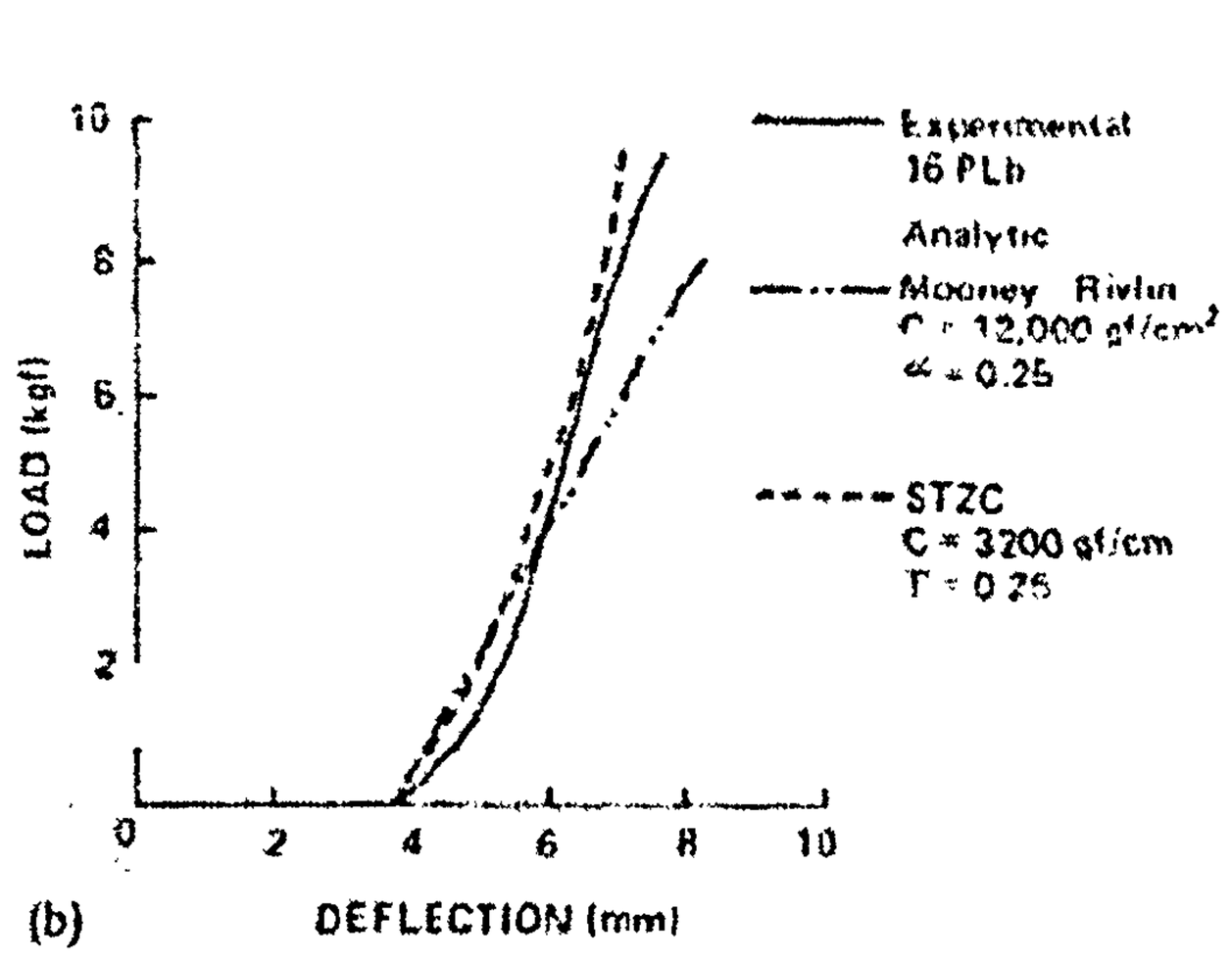

Figure D.10. The experimental and analytical model of fetal dura mater test.

D.9. THE SCALP (Moore 1999)

The scalp is constituted by five layers. There are Skin, Connective tissue (dense), Aponeurosis, Loose connective tissue, and Pericranium, standing for S-C-A-L-P (Figure D.10).

The skin is bound tightly to the epicranial aponeurosis, which is the flat intermediate tendon of the occipitofrontalis muscle. The skin and aponeurosis move freely over the pericranium and skull because of the intervening loose connective tissue.

The different layers of the scalp make it difficult to get the overall properties. However the study of the human skin properties was developed for decades. Non-intrusive testing for the human skin property is one of the most applied methods above all the other methods, see the figure for the material properties.

APPENDIX E. *THE MATERIAL PROPERTIES OF SKULL, BRAIN TISSUE AND VESSELS*

E.1. THE MATERIAL PROPERTIES OF THE SKULL

It helps to achieve a better understanding of the failure characteristics of the biological tissue, when the mechanical properties are obtained. Classical engineering structural analysis is one of the easiest ways to analyse the human bone which has elastic properties (Fung 1993) before failure. Furthermore, understanding fetal cranial bone properties helps to study the head deformation, termed mouldings, during the process of labour.

The test of the elastic modulus against age of the fetal cranial bone could be traced back to McPherson (1980). The samples included 86 specimens harvested from the gestational age group from 25 to 40 weeks fetus, with the comparison of specimens from a 6-year-old calvarium, that were tested in three-point bending method and the elastic modulus was converted from the result. The modulus was found out to be highly sensitive to gestational age and fibre orientation, with ranges from 1.65×10^3MPa for preterm bone to 3.86×10^3MPa for term bone.

Kriewall (1981, 1982)'s series of tests correlate the stiffness of the bone with the bone's material characteristics, for instance modulus of elasticity, mineral content, and bone density, with the anthropometric characteristics, for instance the size and the thickness. In the earlier 3 point bending test with 45 specimens from 25-40 weeks gestational age, with a comparison group of 5 six-year-old calvarium, the elastic modulus was derived and was shown to increase with increasing ash content. Meanwhile, the ash content of the fetal cranial bone increases with increasing gestational age, but with no significant difference between the full term and the adult bone. Therefore the conclusion is reached that the continuing increasing bone stiffness from the infant to adulthood comes from the structure differentiation rather than the material mineralization. The structure differentiation refers to a single layer of the infant skull develops into sandwich beam structure to the adult skull. The later test with 20 samples is more focusing on the correlation between bone stiffness, comes from load-deformation curve, geometrical characteristics and the birth weight. The clear conclusion was made that the anthropometrical factors should account more for the bone load-bearing capacity than do the material characteristics.

Following this profound work, Margulies and Thibault (2000) extends the published data with the comparable properties between human infantile cranial bone and one from porcine. The three point bending tests were carried on with the 4 specimens from 25 weeks-6 months human and 30 specimens of 2-3 days neonate pigs. The derived result shows the increasing elastic modulus, ultimate stress, and energy absorbed to failure and decreasing ultimate strain with the age increasing of both species The comparable bone properties between human and other animal gives one possible approach for biomechanician to scaled the porcine data into the human data in order to study the human tissue injuries, while the human tissue property is not applicable.

E.2. The Material Property Of The Brain Tissue (Metz et al. 1970; Medis et al. 1995; Gefen and Marguilies 2004)

The material property of the brain tissue was an important biomechanical subject that was studied for many years both experimentally and theoretically. An accurately defined mathematical model of the brain has advantages in various areas, for example, the medical treatment such as hydrocephalus, the neurosurgery operation and training, or the traumatic brain injury analysis (Fallenstein and Hulce 1969; Pamidi and Advani 1978; Lanir 1994; Arbogast et al. 1997; Darvish and Crandall 20010; Brands et al. 2004; Nicolle and Lounis et al. 2005).

The brain, considered as a very soft material like most of the other biological tissues, is nonlinear, anisotropic, nonhomogeneous structure with incompressible microscopic sponge, which is different from the traditional engineering material. Its compliant behaviour comes from the cell's collapsibility of the sponge-like parenchyma. Its mechanical properties can be represented by a series of constitutive equations, which contain the specific number of parameters for the loading-deformation description.

An analytical model to analyse the large elastic deformation characterisation was well set up since the classical work by Mooney (1940). Afterwards several forms of the constitutive equations were emerged based on the unique strain energy function, which is expressed as a function of three strain invariants (Pamidi and Advani 1978; Walsh and Schettini 1984). These basic constitutive equations cannot be able to represent the visco-elastic characteristics of the biological tissue, which has highly dissipative properties, therefore some modified constitutive modelling emerges for the brain tissue to give the response with different types of loading (Pamidi and Advani 1978).

There are two main approaches to represent the brain tissue: one is to consider brain as linear and non-linear viscoelastic model; the second is to treat the brain parenchyma as porous linear elastic solid with Newtonian fluid-filled pores. The second approach is based on the consolidation theory and was used to study the CSF-brain tissue interaction (Darvish and Crandall 2005; Nicolle, Lounis et al. 2005et al.2005).

The presented constitutive law should be always correlated with the physical experiments. The stress analysis based on inaccurate theory will produce erroneous results, which is especially acute when the deformations are nonhomogeneous and multidimensional, because otherwise such errors are difficult to detect.

Over the past few decades, one of the most important numerical method-finite element methods was developed quickly to investigate the human head injuries via three-dimensional modelling. The high degree of anatomical accuracy and the material characterisation of the human brain are required and essential for the accuracy of the outcome (Nicolle, Lounis et al. 2005). Furthermore, the emergence of robotic surgery and virtual reality surgery training techniques call for the close representation of the human brain tissue with the proper mathematical description. Therefore engineering testing of the brain tissue became a central subject in biomechanics and helps to determine the analytical model. However, there are many difficulties for the constitutive equations to reach a consensus with the real biological tissue. The reasons are various such as the limited performance of engineering testing methodology, the ethical restrictions preventing living or post-mortem tissue from being obtained in time, the testing performance in vitro or in vivo and the influence of the deterioration, the age dependency of the brain developing from infant to adult, the non-linear viscoelastic properties that lead to different energy dissipation with different strain rate.

The fact that the bulk modulus of brain tissue is about 10^6 times higher than the shear modulus indicates the brain can be represented as a viscoelastic material with storage and loss shear modulus under the various frequency (Thibault and Margulies 1998).

The earlier data of Estes and MeElhaney (1970)'s result was used by Pamidi and Advani (1978) to determine a non-linear constitutive equations for human brain tissue including dissipation energy rate terms. This result can be providing the data for head injury modelling analysis in high strain rate. Miller and Chinzei (1997) design an experiment for six-month-old swine brain tissue in vitro with uniaxial unconfined compression test (Figure E.1). The strain rate are $0.64s^{-1}$, $0.0064s^{-1}$, $0.0000064s^{-1}$ separately that much lower than the previous tests. With the result they determined the corresponding non-

linear viscoelastic model based on the strain energy function in polynomial form with time-dependent coefficients for surgical procedure (Figure E.3). Later based on the same result, a large deformation, hyper-viscoelastic model were evaluated by Miller et al. (1997, 1999, 2000, 2005), which is suitable for a commercially available finite element package. It contained four material constants and good for compression levels over 30% weight over five orders loading velocity. This model was then used to compare with an in vivo indentation test to a 100 day old anaesthesia swine (Figure E.2) (Miller and Chinzei 1997). The result was considered very well with the predicted forces 31% lower than experiment. In his model the linear viscoelastic model is not appropriate to simulate the brain tissue even in moderate strains. Following the compression test, Miller, Chinzei et al. (2002) conducted a uniaxial tension test with six month old swine specimen in vitro with low frequency strain rate, the tissue was found to be softer in extension than in compression and strong stress-strain rate dependence. A new hyper-viscoelastic model was then proposed, which is more adequate to explain tension and compression behaviour than the previous model. The recent test of the brain shear behaviour over large frequency range is performed by Nicolle , Lounis et al. (2005), the mean storage modulus and loss modulus covered the frequency from 0.1 to 6310Hz, with the result from 2.1±0.9kPa to 16.8±2.0kPa and from 0.4±0.2kPa to 18.7±2.3kPa respectively. Margulies, Thibault et al. (1990) and later Coats and Margulies (2006) investigated the heterogeneity of the brain between white matter and grey matter which were treated as homogeneous due to the previous limited regional data.

Thibault and Margulies (1998) investigated the age effect material properties of the porcine brain tissue, by testing 2-3 days and adult pig specimens for shear modulus. The constitutive modelling with head injury tolerance criteria specifically for paediatric population was firstly determined. The constitutive equations combining with Margulies and Thibault (2000)'s test with infantile cranial bone of both human and porcine, infantile porcine suture, become the material properties of the constructed finite element model, and demonstrated the brain deformation and force response under the impact loading that different from adults'.

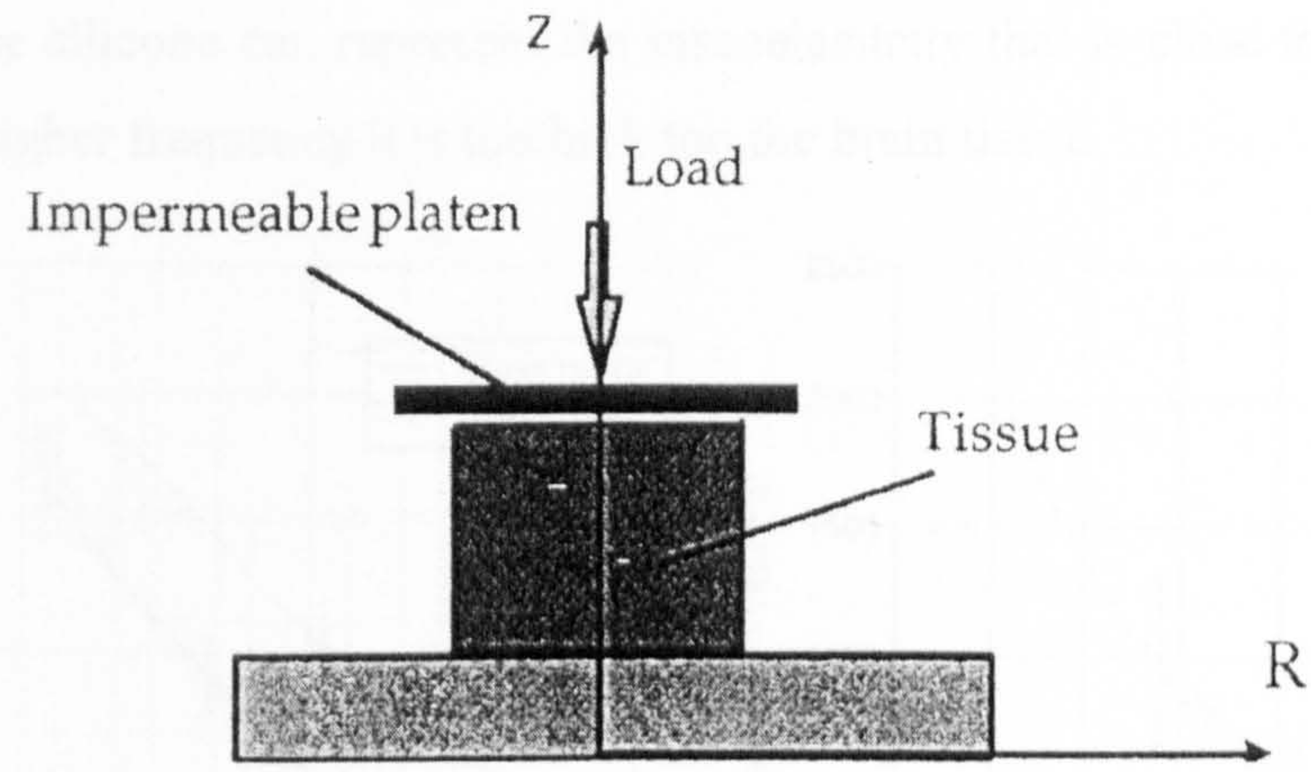

Figure E.1. *Experimental set up of porcine brain tissue testing in vitro (Miller and Chinzei 1997).*

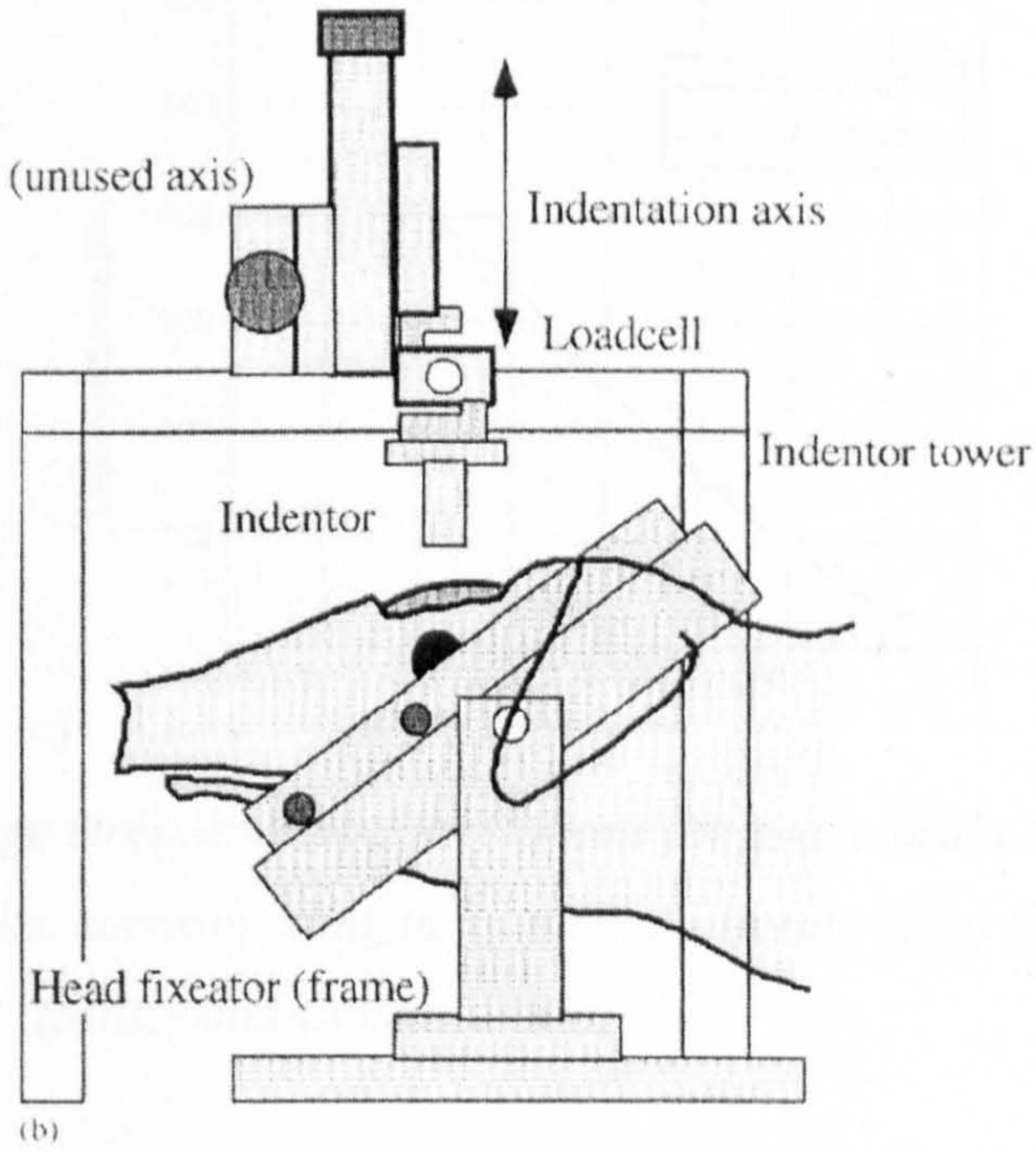

Fig. 1. In vivo indentation of swine brain-experiment configuration: (a) general view; and (b) schematic of the set-up.

Figure E.2. *Indentation of swine brain in vivo (Miller, Chinzei et al. 2000).*

The substitute material of the brain tissue is required when the physical model replica was constructed. Margulies, Thibault et al. (1990) and Kleiven and Holst (2002), and Brands (2002) choose the Dow Corning Dielectric Silicone 527 A&B® (Dow Corning Corporation 2008) as the brain substitute for its viscoelastic strain rate dependency properties. Brands (2002) test the silicone gel for the complex shear modulus and compared it with the porcine brain tissue. It was found out that under the low frequency

strain rate the silicone can represent the viscoelasitcity that is close to the brain tissue, and for the higher frequency it is too high too the brain tissue.

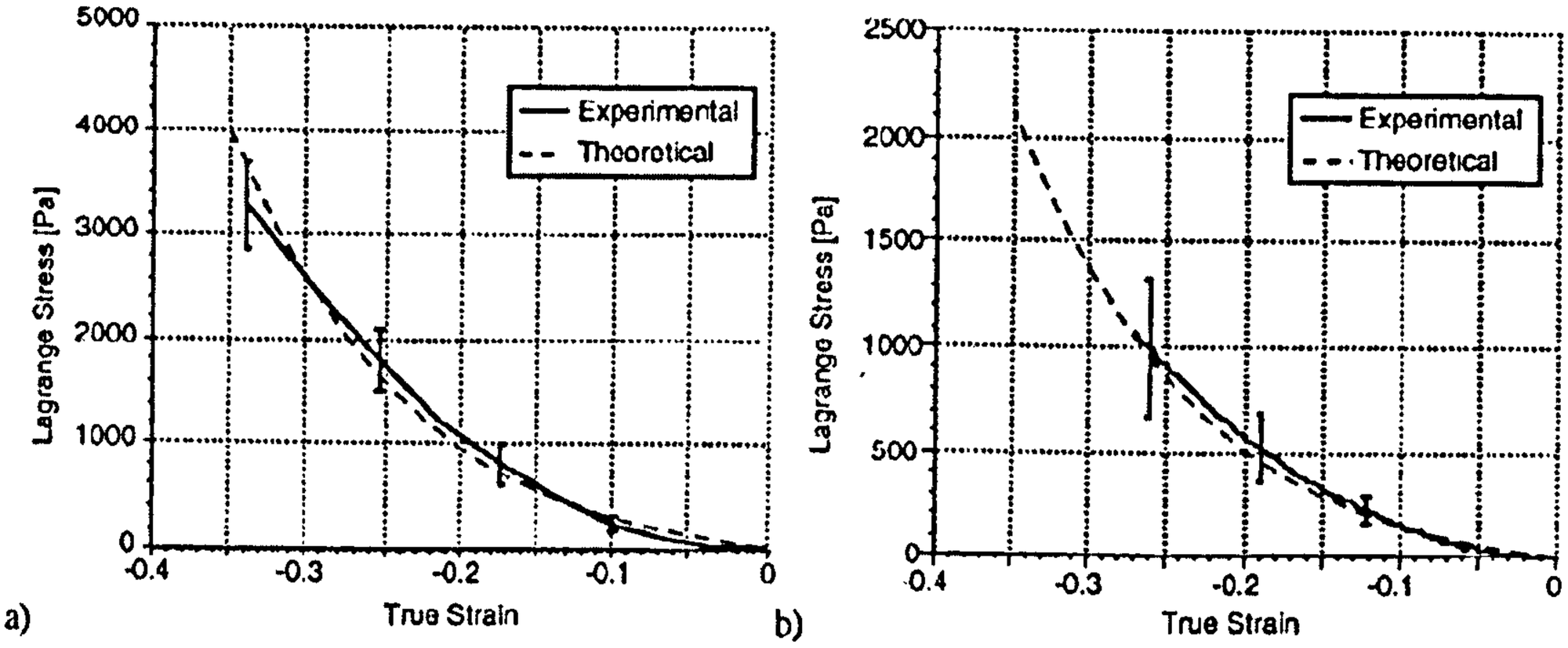

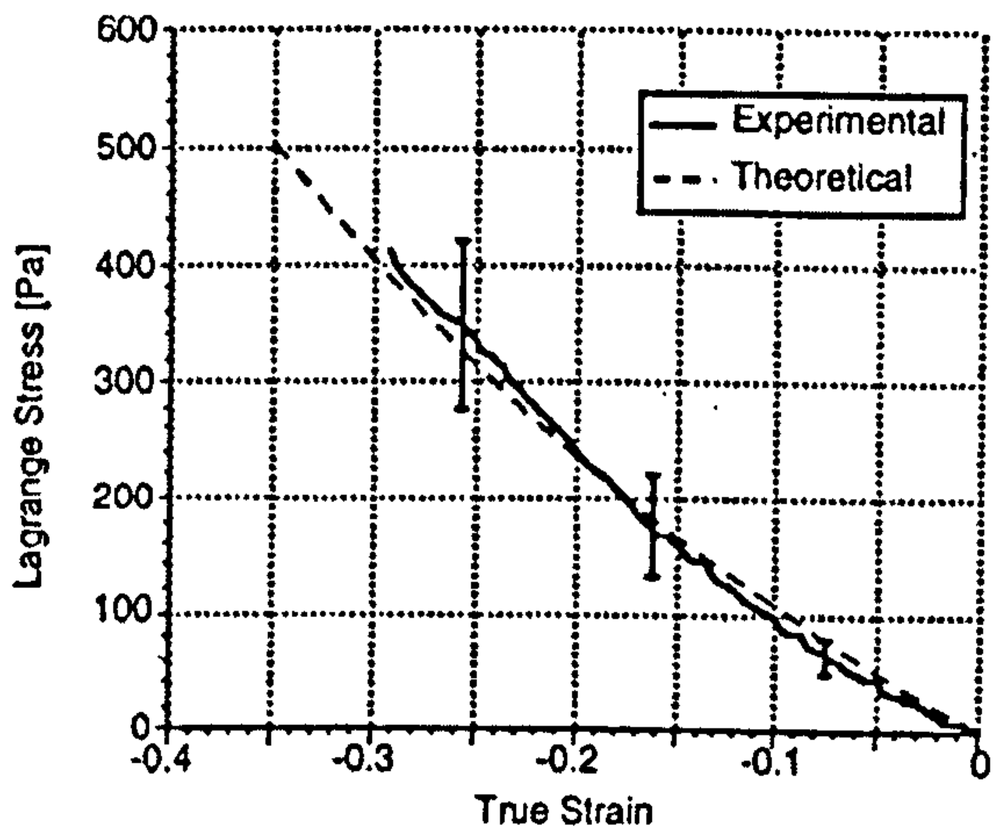

Figure E.3. *Lagrange stress-true strain relations for swine brain tissue. Experimental and theoretical results. corresponding to loading strain rate of (a) 0.64 s^{-1}; (b) 0.64×10^{-2} s^{-1}; (c) 0.64×10^{-5} s^{-1}. (Miller and Chinzei 1997).*

E.3. The Material Property Of The Cerebral Cortical Vessels

Several tests for material properties of the bridging vein were carried on for decades from animal to human corps, and to fresh human tissues. The failure stress against the stretch ratio and the strain rate are of the most interest. The earlier tests by Gennarelli and Thibault (1982) with rhesus monkey and Lõwenhielm (1974) with human parasagittal bridging veins and Van Lierde et al. (2005) with embalmed human cadavers reported a strain rate dependence property. Later Gennarelli and Thibault (1982) advocated the tolerance data of the subdural haemorrhage by the strain rate sensitivity

of the rhesus monkey. However, Lõwenhielm (1978) with bovine parasagittal bridging veins and Lee, Melvin et al. (1989) with human cadavers parasagittal bridging veins showed that the ultimate strain was independent of stretch rate, which call for the careful investigation of the strain rate account for the injury tolerance. The latest test by Monson and Goldsmith (2003) with the fresh healthy harvest human cerebral vessels demonstrated again that the strain rate has little significance on the mechanical properties of the human cortical blood vessels. Furthermore it is found out that the cortical arteries are stiffer than the cortical veins with twice failure stress and half of the stretch (Figure E.4).

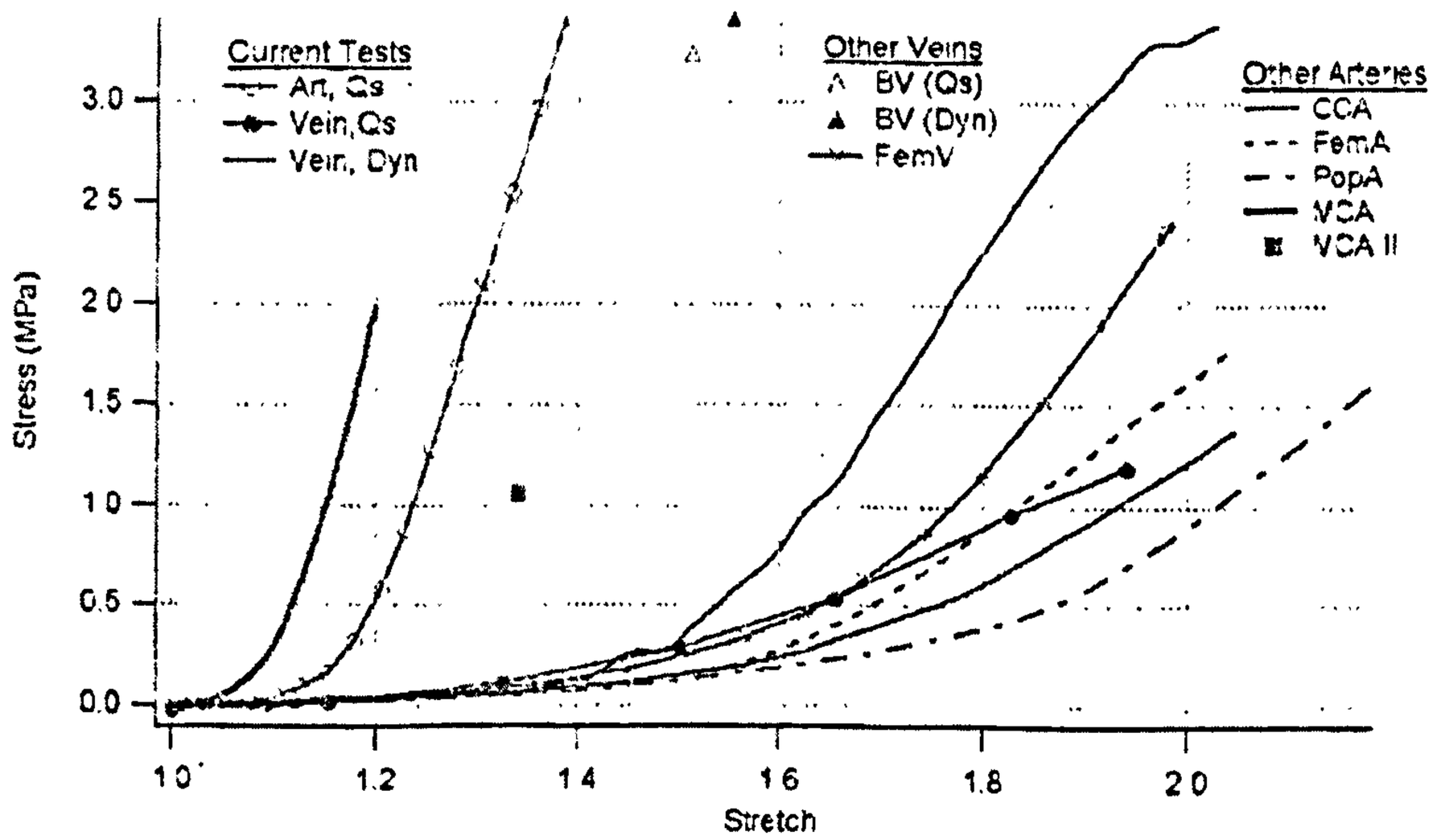

Figure E.4. *Comparison of stress-stretch behaviours from the literature of a variety of blood vessels (Monson and Goldsmith 2003).*

APPENDIX F: *DYNAMIC TEST IN VISCOANALYZER2000*

Dynamic test is a test that measures the strain (or stress) produced by a stress (or strain) as a sinusoidal function of the time, when setting up the body as an equilibrium at the time zero t_0.

The viscosity of the material with its storage modulus E' and loss modulus E'', the phase factor δ, and loss factor $tg(\delta)$ will be derived from the testing. In practice, the measurement of E′ and E" can be obtained from the force $F(\omega)$, the displacement $d(\omega)$, the phase angle δ, and the frequency f.

The pulsation ω is equals:

$$\omega = 2\pi f \text{ rad/s}$$

The relation between the theory and practical measurement can be interpreted shown in Figure F.1:

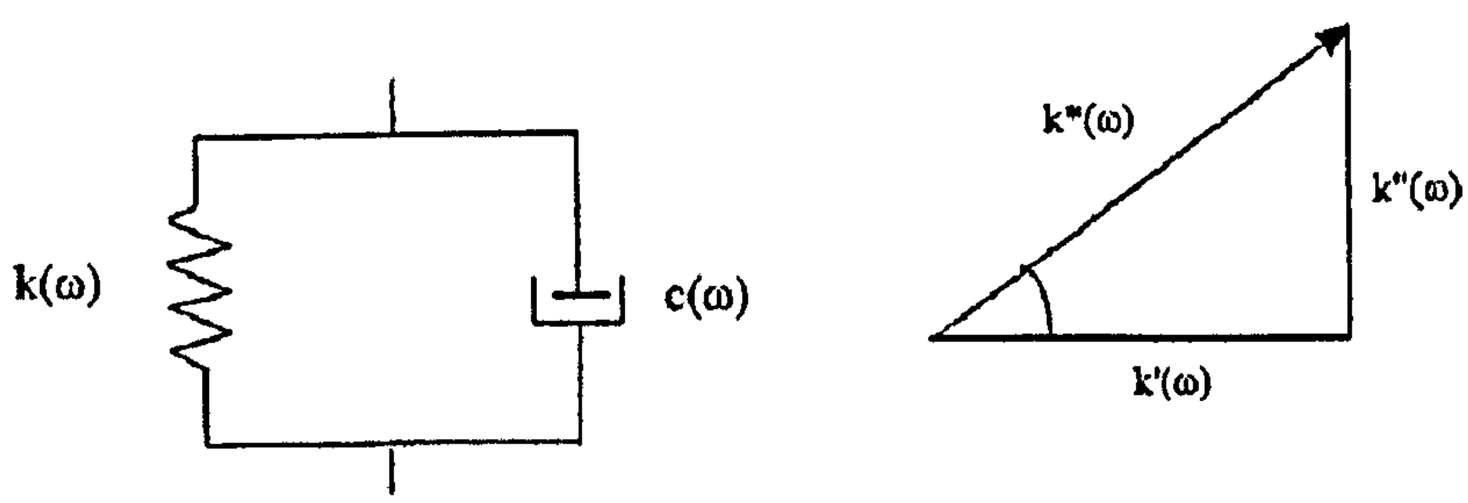

Figure F.1. *Viscoelastic analytical model and the complex modulus with its storage and loss factors.*

Therefore, the equation representing the behaviour of the material can be expressed as follows:

$$k^*(\omega) = k'(\omega) + jk''(\omega)$$

or

$$k^*(\omega) = k'(\omega)(1 + jtg\delta(\omega))$$

The real part k' is derived directly from Hooke's law generalized in relation with the ratio of a dynamic force $F(\omega)$ over a displacement $d(\omega)$.

$$k'(\omega) = \frac{F(\omega)}{d(\omega)}$$

$tg\delta(\omega)$ is the tangential of the phrase angle between $F(\omega)$ and $d(\omega)$.

It is therefore possible to obtain $k^*(\omega)$ with the equation

$$k^*(\omega) = \frac{F(\omega)}{d(\omega)}(1 + tg\delta(\omega))$$

Using these measurements, it is then possible to obtain the intrinsic characteristics of the materials directly by multiplying the components of the dynamic stiffness (k', k'') by a geometric stress concentration factor with the dimensions of the inverse of one length. Depending on the solicitation of the sample, it is possible to obtain to the complex tension modulus, complex shear modulus or the complex viscosity, respectively.

$$E^* = E'(\omega)(1 + j\tan\delta) = E' + jE''$$

APPENDIX G: *THE STUDY OF THE SIMPLE FE MODEL*

A 2D Finite element Finite Element (FE) geometry of a simplified infant head sagittal plane was constructed (Figure G.1). The model is consisted of 960 solid elements and 63 shell elements, of 6328 nodes in total. The model includes the biological tissues of 4-node-shell skull, scalp, 8-nodel-solid brain and the CSF representative between the skull and brain. The skull has average diameter of 102.7mm, and the thickness of the sagittal plane is 5mm. The width of the scalp is 40mm to represent the anterior fontanelle underneath the skin.

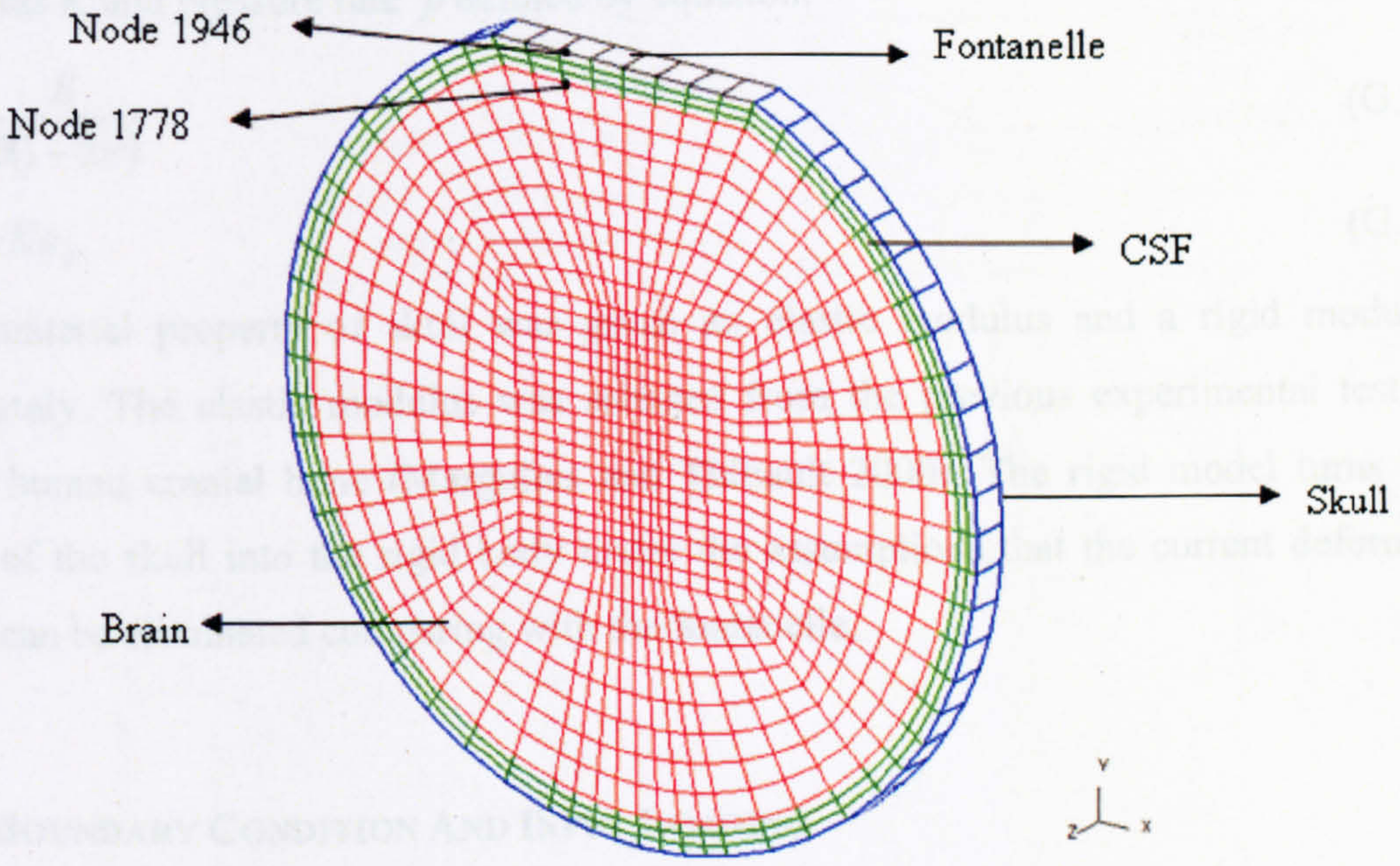

Figure G.1. *Boundary condition model testing.*

G.1. THE MATERIAL PROPERTY

The material characteristics are studied with a range of variation of the material properties according to the simulation in order to find out the most realistic model of the biological tissue.

Two material models were selected for the brain tissue, the elastic model from Miller and Chinzei (1997) of the tension-compression test on porcine brain tissue, and the linear viscoelastic model from Margulies and Thibault (2000) three point bending test on porcine brain tissue.

$$\sigma = E\varepsilon \tag{G.1}$$

$$G(t) = G_{\infty} + (G_0 - G_{\infty})e^{-\beta t} \tag{G.2}$$

For the elastic model, the elastic module E were defined as the slope of the linear regression in elastic regime of the Miller's stress strain curve with $E=2.5\times10^{-3}$MPa in low strain rate tension-compression test. The viscoelastic modulus has short term modulus $G_0=5.99\times10^{-3}$MPa, and long term modulus $G_\infty=2.32\times10^{-3}$MPa, decay factor $\beta=0.09248s^{-1}$.

$$G=\frac{E}{2(1+\nu)} \tag{G.3}$$

The elastic fluid model is defined specifically in non-linear explicit finite element code LS-DYNA, where the fluid like behaviour is defined in solid elements with the bulk modulus K and pressure rate p defined by equation.

$$K=\frac{E}{3(1-2\nu)} \tag{G.4}$$

$$\dot{p}=-K\dot{\varepsilon}_{ij} \tag{G.5}$$

The material property of skull was given an elastic modulus and a rigid modulus separately. The elastic modulus was selected from the previous experimental test of adult human cranial bone (Margulies and Thibault 2000). The rigid model turns the shell of the skull into the rigid body under the assumptions that the current deformed skull can be eliminated comparing with the fontanelle.

G.2. Boundary Condition And Input Loading

The boundary conditions between the fluid and structure part is merging nodes between the fluid solid and structure solid elements, instead of involving contact surfaces to avoid the separation between the two components while the relative motion is not large enough to cause the mesh failure. This assumption is consistent with the findings with the result of Wittek and Omori (2003).

Two linear input curves were applied to the model. One is the original torso movement reconstructed from the TRL test with the peak acceleration of 4g (39.24mm/s^2) (Figure G.2(a)). The second is the scaled value with the peak acceleration up to 20g (196.2mm/s^2) (Figure G.2(b)), which is coincident with the maximum value collected from the dummy's head due to the TRL test (Chapter 3).

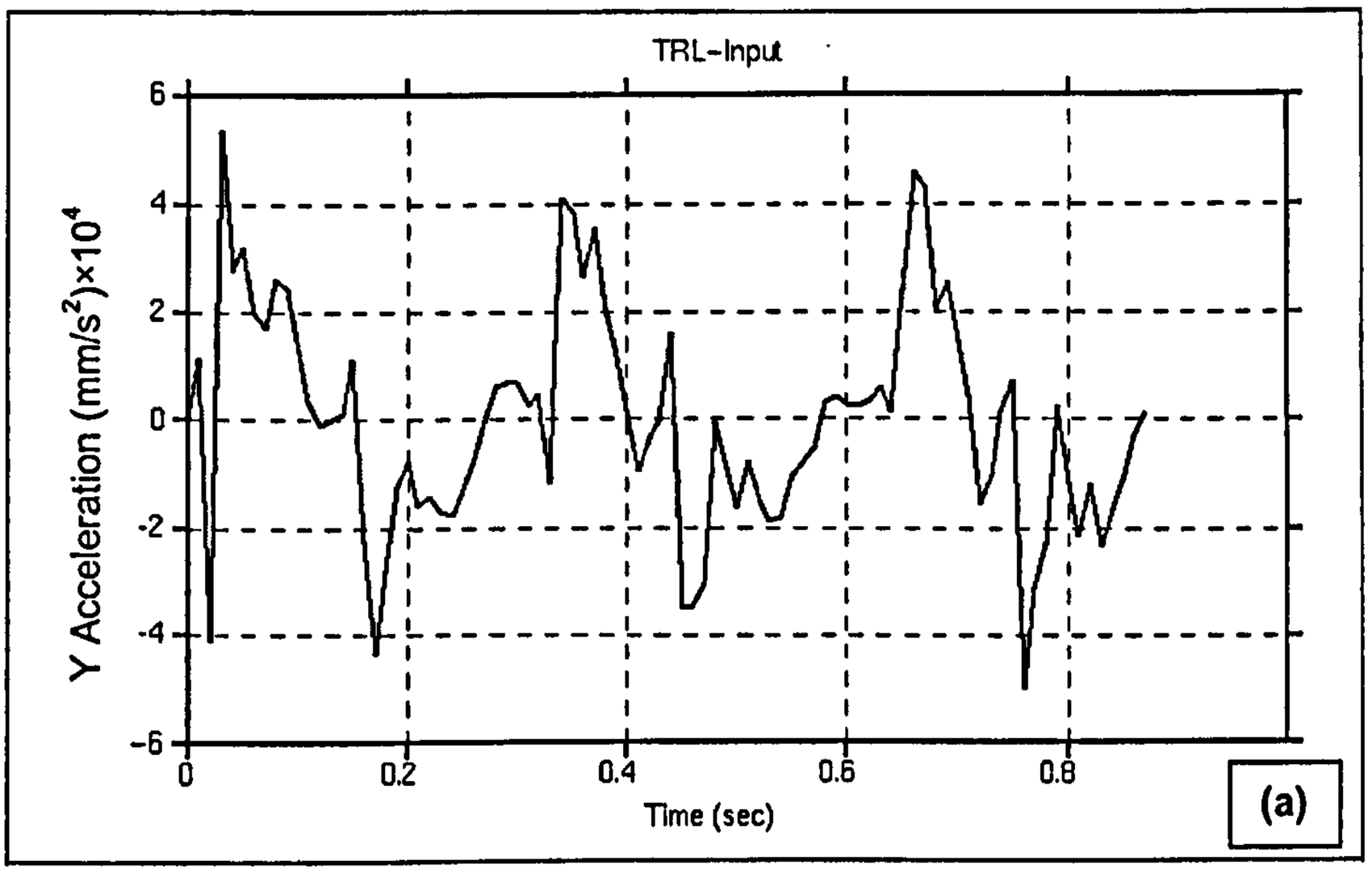

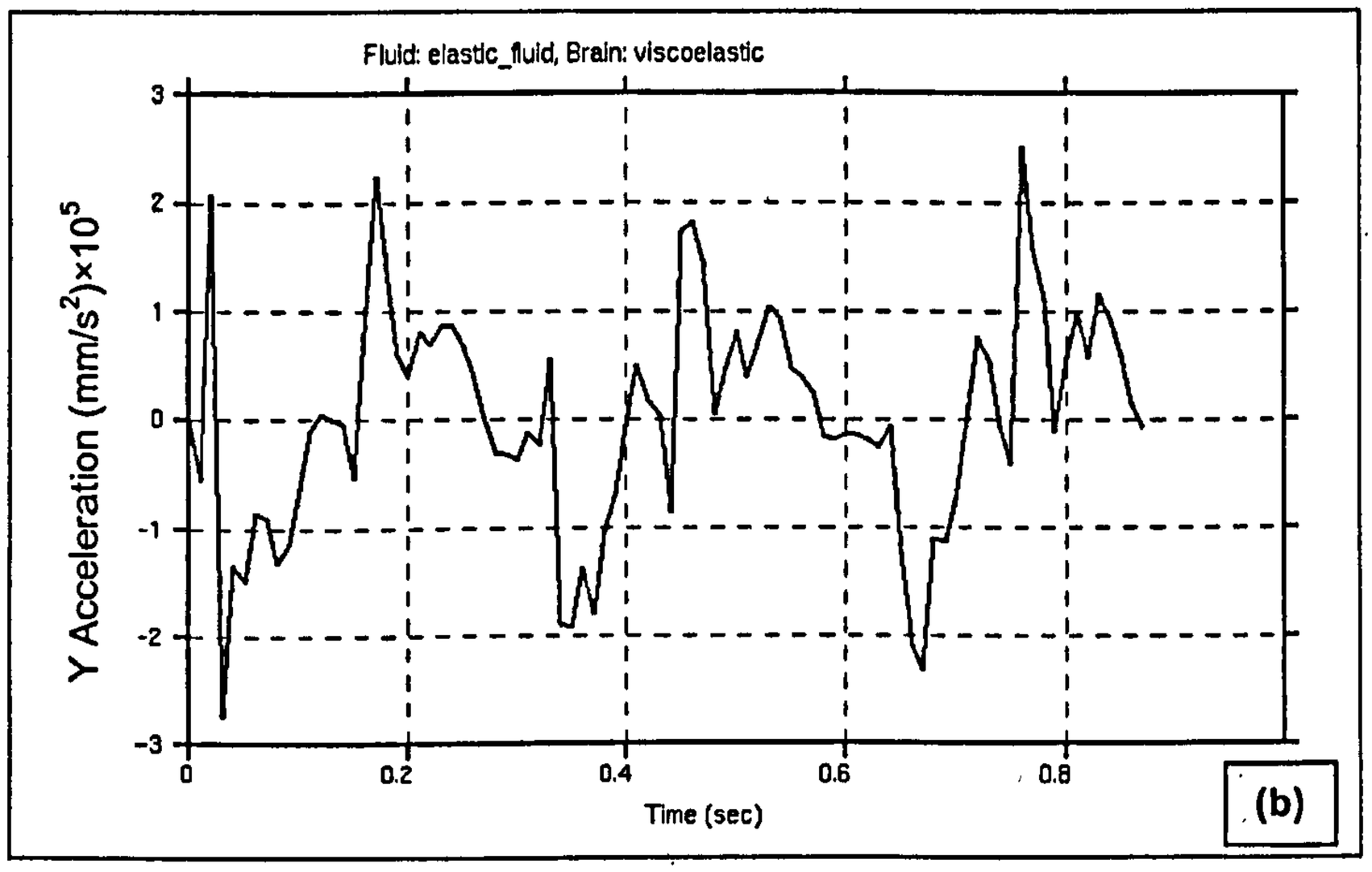

Figure G.2. *Input linear acceleration of (a) TRL output with peak value of 4g, (b) scaling result with peak value of 20g.*

G.3. RESULT

The deformation and shear stress contour are presented in Figure G.3. The FE model demonstrates the deformation of the brain tissue and the resulting shear stress was highly sensitive to the softness of the top skull structure, the fontanelle. The shear stress in between the space of brain and fontanelle inside CSF is significantly higher than the other parts of the model. The brain experiences deformation with the influence from the fontanelle. These results, however, are only aimed to study the characteristic properties

of different modelling of the human tissue and further discussion of the shaking brain injury will be carried on into Chapter 8.

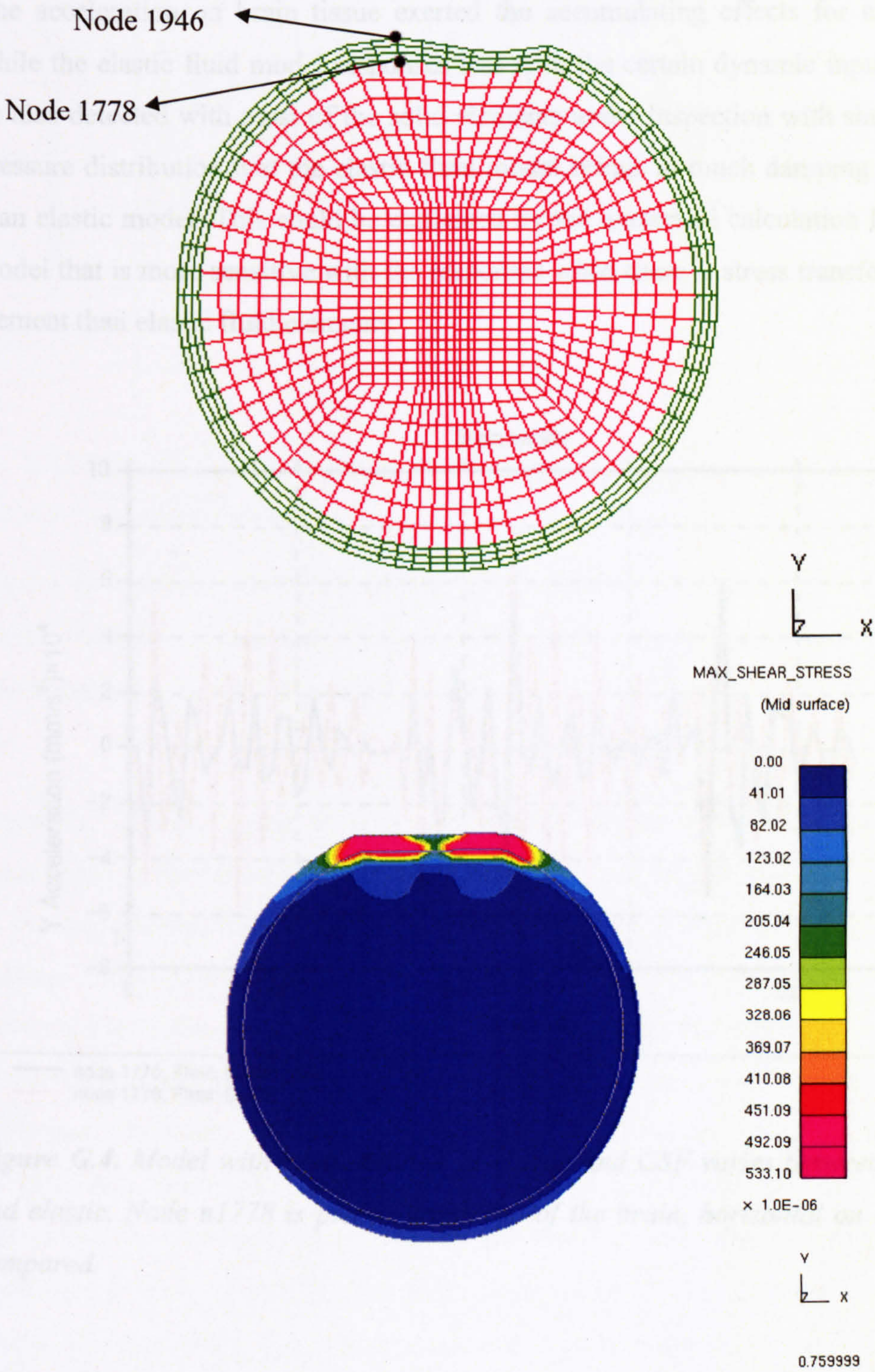

Figure G.3. *The mesh of deformed model and contour of shear stress during simulation at its maximum deformation during the shaking.*

In order to study the acceleration of the specific area, several nodes were selected from the top of the brain elements and CSF element underneath the fontanelle area, among

them the acceleration is similar therefore node n1778 and n1946 were plotted in Figure G.4 with the comparison between brain tissue with Elastic model and Elastic-Fluid model.

The acceleration on brain tissue exerted the accumulating effects for elastic model, while the elastic fluid model responses less with the certain dynamic input. This could be also detected with most of the solid elements under inspection with shear stress and pressure distribution that the elastic fluid model brings in much damping phenomenon than elastic model. This could be explained by the numerical calculation for the elastic model that is more sensitive with the responses when there is stress transfer through the element than elastic fluid elements.

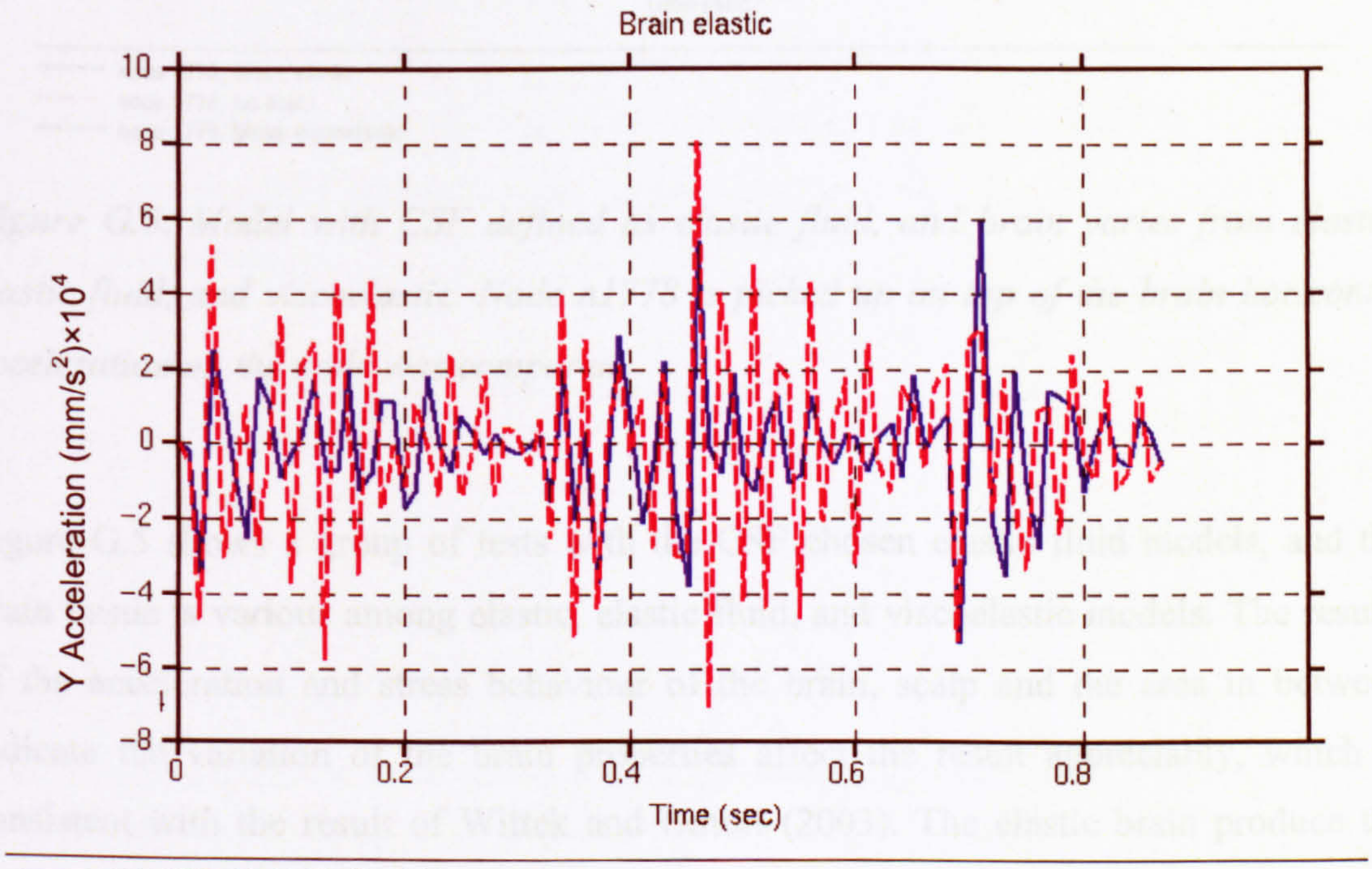

Figure G.4. *Model with brain defined as elastic and CSF varies between elastic fluid and elastic. Node n1778 is picked up on top of the brain, horizontal on the node was compared.*

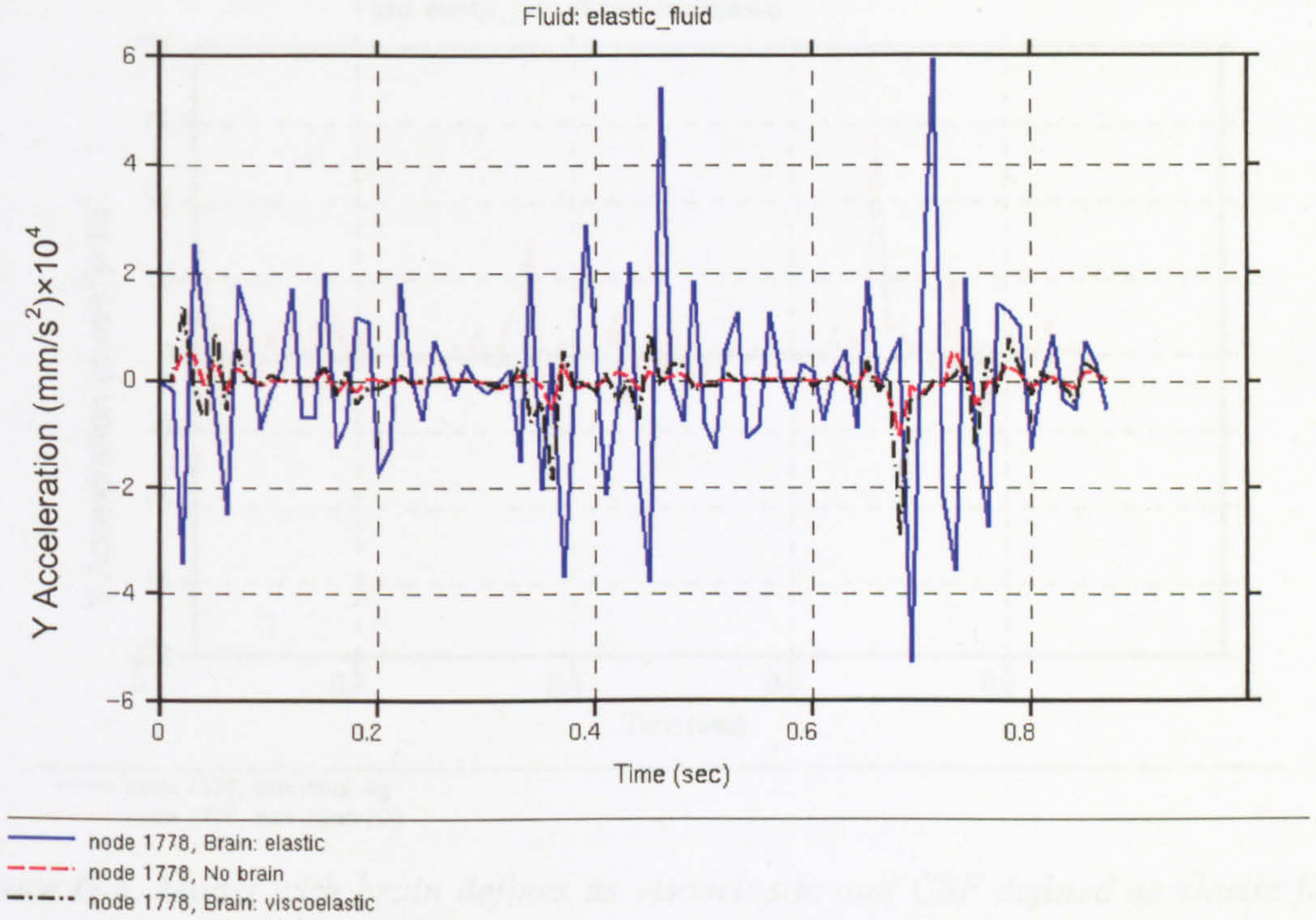

Figure G.5. *Model with CSF defined as elastic fluid, and brain varies from elastic, elastic fluid, and viscoelastic. Node n1778 is picked up on top of the brain horizontal acceleration on the node was compared.*

Figure G.5 shows a group of tests with the CSF chosen elastic fluid models, and the brain tissue is various among elastic, elastic fluid, and viscoelastic models. The results of the acceleration and stress behaviour of the brain, scalp and the area in between indicate the variation of the brain properties affect the result appreciably, which is consistent with the result of Wittek and Omori (2003). The elastic brain produce the acceleration most vigorous while the elastic fluid and viscoelastic model generate less responses. The stress difference was accumulated for the area than that far away from the brain area, while the interaction of the brain and fluid has the smaller stress.

Figure G.6 shows a comparison between the linear input movement with its maximum acceleration from 4g to 20g, for given brain tissue model of viscolelastic, and CSF model of elastic fluid. The calculated acceleration is respected to the magnitude of the dynamic loading.

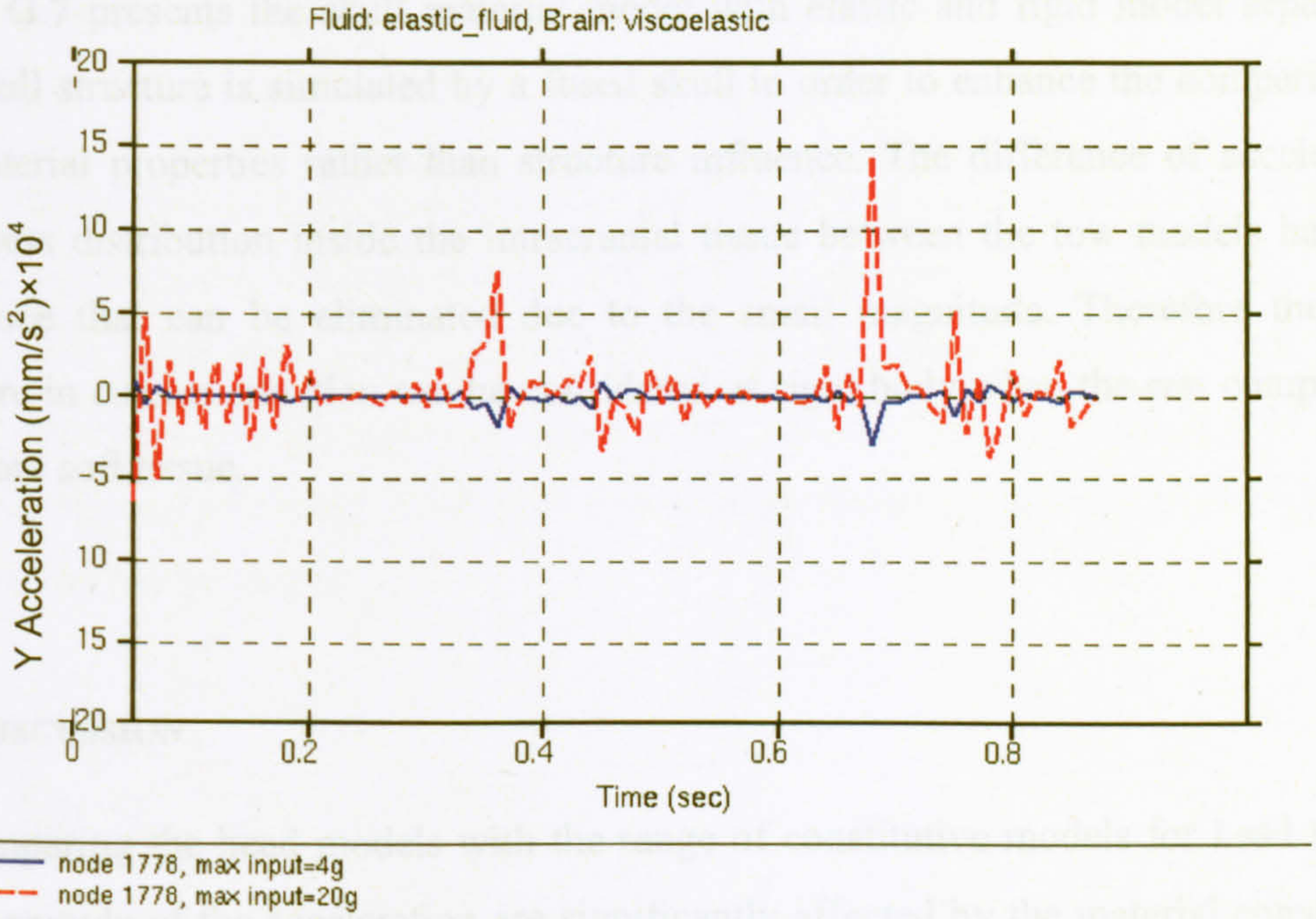

Figure G.6. *Model with brain defines as viscoelastic and CSF defined as elastic fluid, the input acceleration varies between 4g and 20g for peak value. Node n1778 is picked up on top of the brain.*

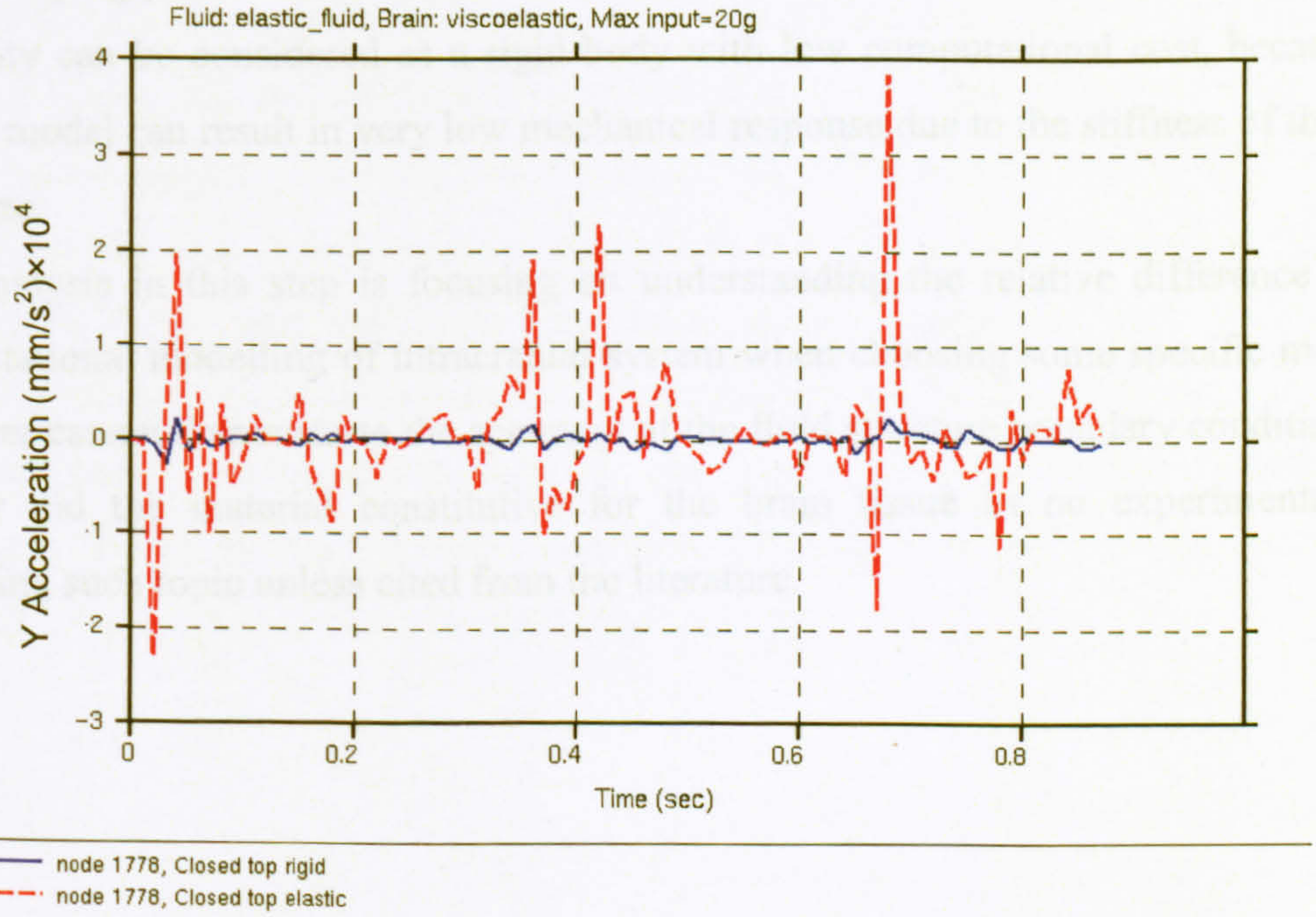

Figure G.7. *Model with brain defined as viscoelastic and CSF defined as elastic fluid, the fontanelle varies between rigid and elastic. Node n1778 is picked up on top of the brain.*

Figure G.7 presents the skull material model with elastic and rigid model separately. The skull structure is simulated by a fused skull in order to enhance the comparison of the material properties rather than structure influence. The difference of acceleration and stress distribution inside the intracranial tissue between the tow models have the difference that can be eliminated due to the small magnitude. Therefore the skull structure in current situation can be considered as rigid body when the rest components inside are soft tissue.

G.4. DISCUSSION

By comparing the head models with the range of constitutive models for head tissues, the magnitude of the acceleration are significantly affected by the material constitutive model as well as its properties. For the CSF, the elastic model produces a more vigorous response than elastic fluid formula, while for brain the elastic model generates higher force and stress than elastic fluid and viscoelastic model. The elastic fluid generates the most damping phenomenon inside the system. The skull with its histological property as elasticity can be considered as a rigid body with low computational cost, because the elastic model can result in very low mechanical response due to the stiffness of the skull structure.

The analysis in this step is focusing on understanding the relative difference in the computational modelling of intracranial system when choosing some specific model, it however cannot demonstrate the accuracy of the fluid structure boundary condition, and neither did the material constitutive for the brain tissue as no experimental data regarding such topic unless cited from the literature.

APPENDIX H: *THE MADYMO SIMULATION WITH THE TRL SIGNAL*

The reconstruction of head motion can be performed using a computational multi-body modelling simulation with software MADYMO (Mathematical Dynamic Models) (TNO Automotive, Delft, Holland)[1]. MADYMO offers multi-body modelling simulation to design and optimise automotive occupant safety system. It has a database with a wide range of human body models and provided a comprehensive approach to reconstructed 3D head motion by shaking.

H.1. THE METHOD

Two human body models from the MADYMO database were chosen, with one 9 months old and the other 18 months old. The neck was given as an default in MADYMO that allows the head moves extensively with lag phenomenon behind the torso. A linear torso displacement along x axis from TRL data was collected and input into the MADYMO model. Global acceleration from the horizontal (X axis, Chapter 3 Figure 3.1, page 52) and the vertical (perpendicular to horizontal plane) directions of the model was collected, and input into two simplified finite element models (Figure H.1). The FE model was constructed for a 1 month old infant head by eight noded solid element for brain and CSF and four noded shell elements for skull and skin. A paediatric feature, anterior fontanelle was produced with the absent of the skull on the top (open model), while a comparison one was made by fused skull (closed model).
The material property and boundary condition is similar with the FE model discussed in Appendix G, and will not be described here in detail.

[1] The shaken baby injury via MADYMO simulation is a MSc student project supervised by Dr Alaster Yoxall, Sheffield Hallam University, S11 8UZ, a.yoxall@shu.ac.uk

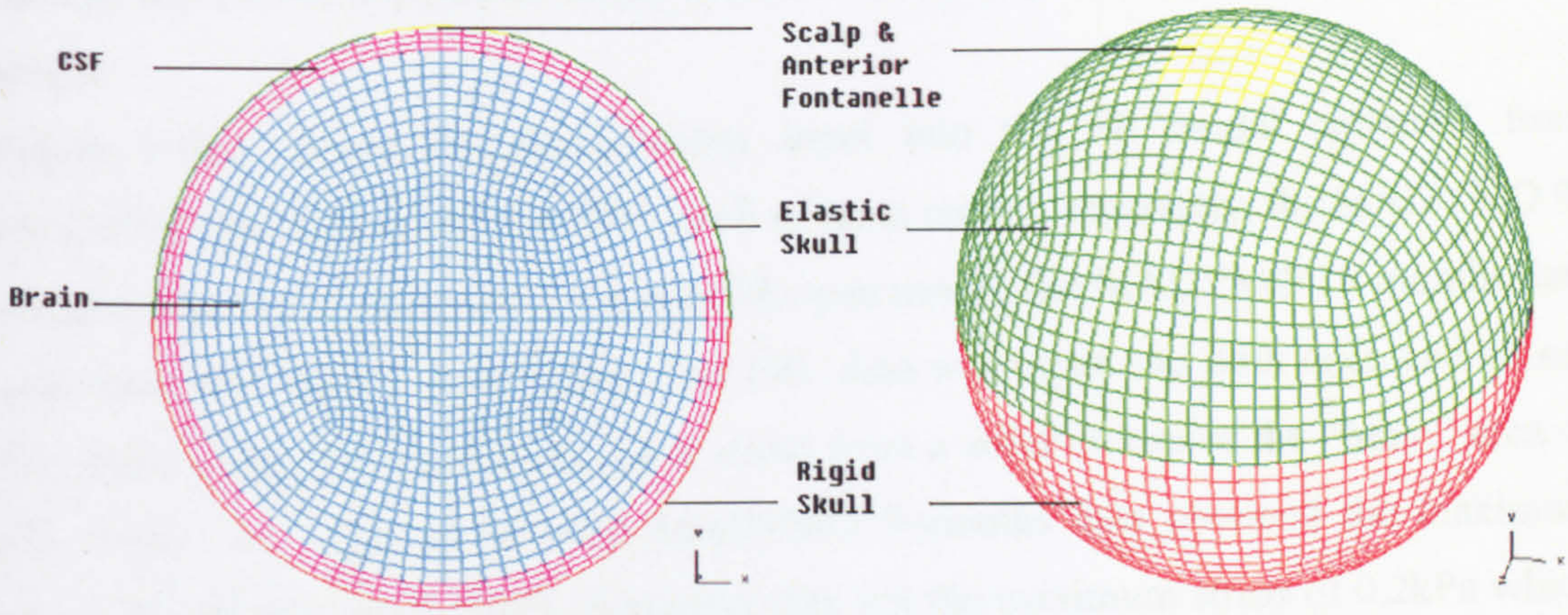

Figure H.1. *A simple geometric model with fined meshed element for a one-month-old infant head.*

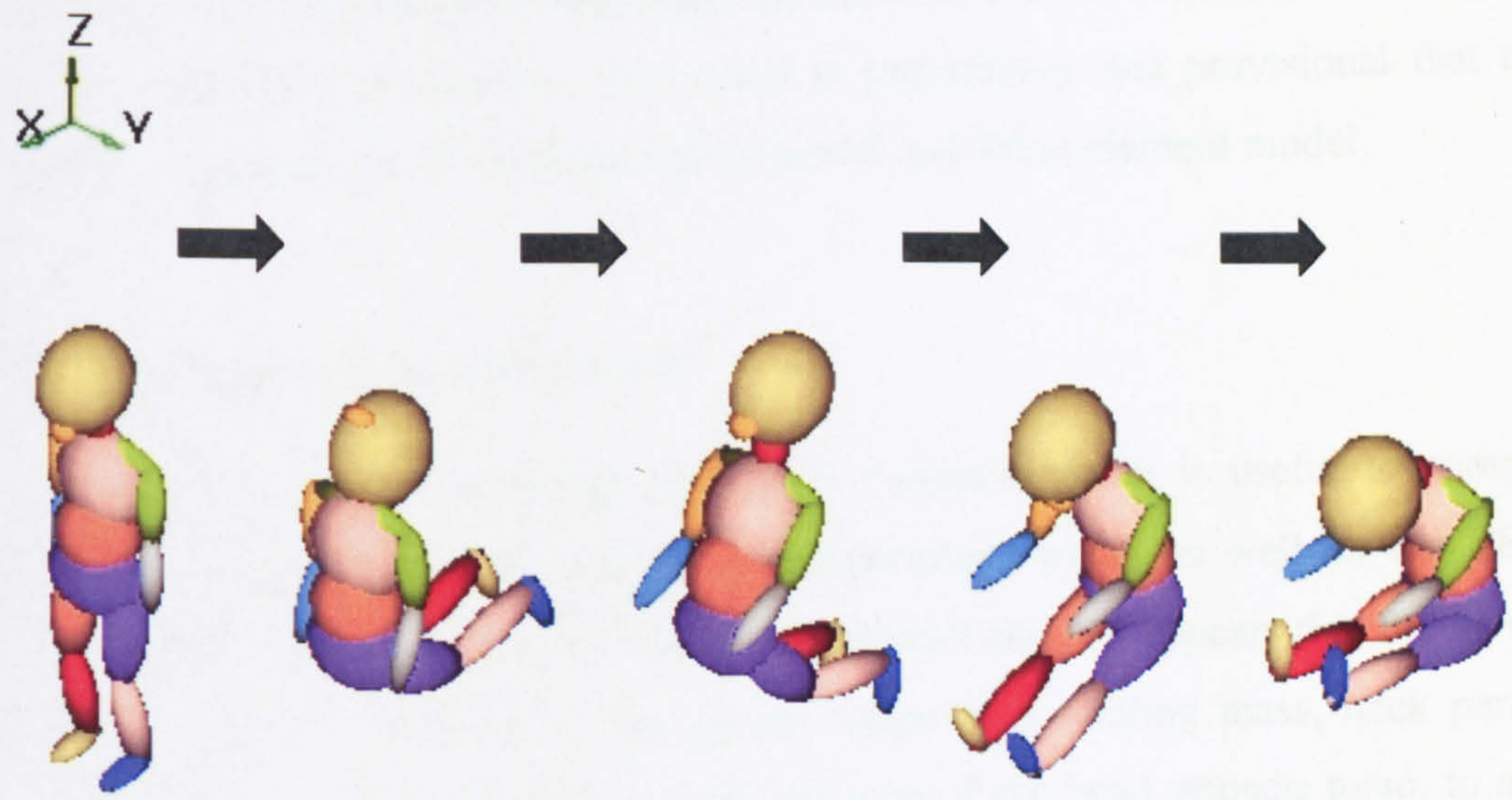

Figure H.2. *MADYMO simulation of shaking a 9 months model.*

H.2. THE RESULT

Figure H.2 gives the MADYMO simulation, and Figure H.3 depicts the global acceleration collected from the head of the model in horizontal and vertical direction. In horizontal direction, the maximum load for 9 months dummy is 15g and for 18 months is 20g. There is no significant difference between the two models. In vertical direction, the maximum load for 9 months dummy is 20g, and for 18 months dummy is 15g, the 9

months old model experience larger critical load during shaking than the 18 months model.

Figure H.4(a) shows the accelerations input into the FE model collected from MADYMO simulation and the TRL result of torso motion separately, the MADYMO 9-months data was applied into a 1 month FE open model, the MADYMO 18-months data was input into the FE close model. The TRL data was input into both open and closed FE model. Figure H.4 gives the shear stress from a solid on top of the "brain" area of FE model. The open model with MADYMO 9-months data obtained the maximum stress of 0.42kPa. MADYMO 18-months data got the maximum stress of 0.2kPa which half of the 9-months data. The TRL data, with the input data slightly smaller than the MADYMO result, had 0.2kPa maximum shear stress for open model, and 0.08kPa stress for closed model. The overall shear stress of TRL open model is below the MADYMO 18-months model. The result qualitatively shows the model with fontanelle obtained more deformation underneath the fontanelle under the similar loading than the model without these features. The result is preliminary and provisional that requires further improvement for both rigid body model and finite element model.

H.3. Discussion And Conclusion

The application of MADYMO rigid body dynamic model is useful to compare the results with the analytical method and experiment work, as well as the FE model comparison between the model with loose and stiff skull. It appears that the MADYMO simulation can be adjusted in the proper range of modelling mass, neck parameters, contact surface property between head and torso if the head impacts torso, to acquire a certain useful value of the head motion trajectory. Combining with the analysis work was done for angular acceleration analysis of a human head, MADYMO is a powerful and effective tool to obtain the shaking characteristics of head motion. The current experiment is preliminary and provisional, future analysis will be focused on reproducing the accurate 3D shaking motion and the biofedelic neck properties of the infant.

The analysis method between MADYMO and FE model is one of an effective approach for the biomechanician to systematically understand the head injury.

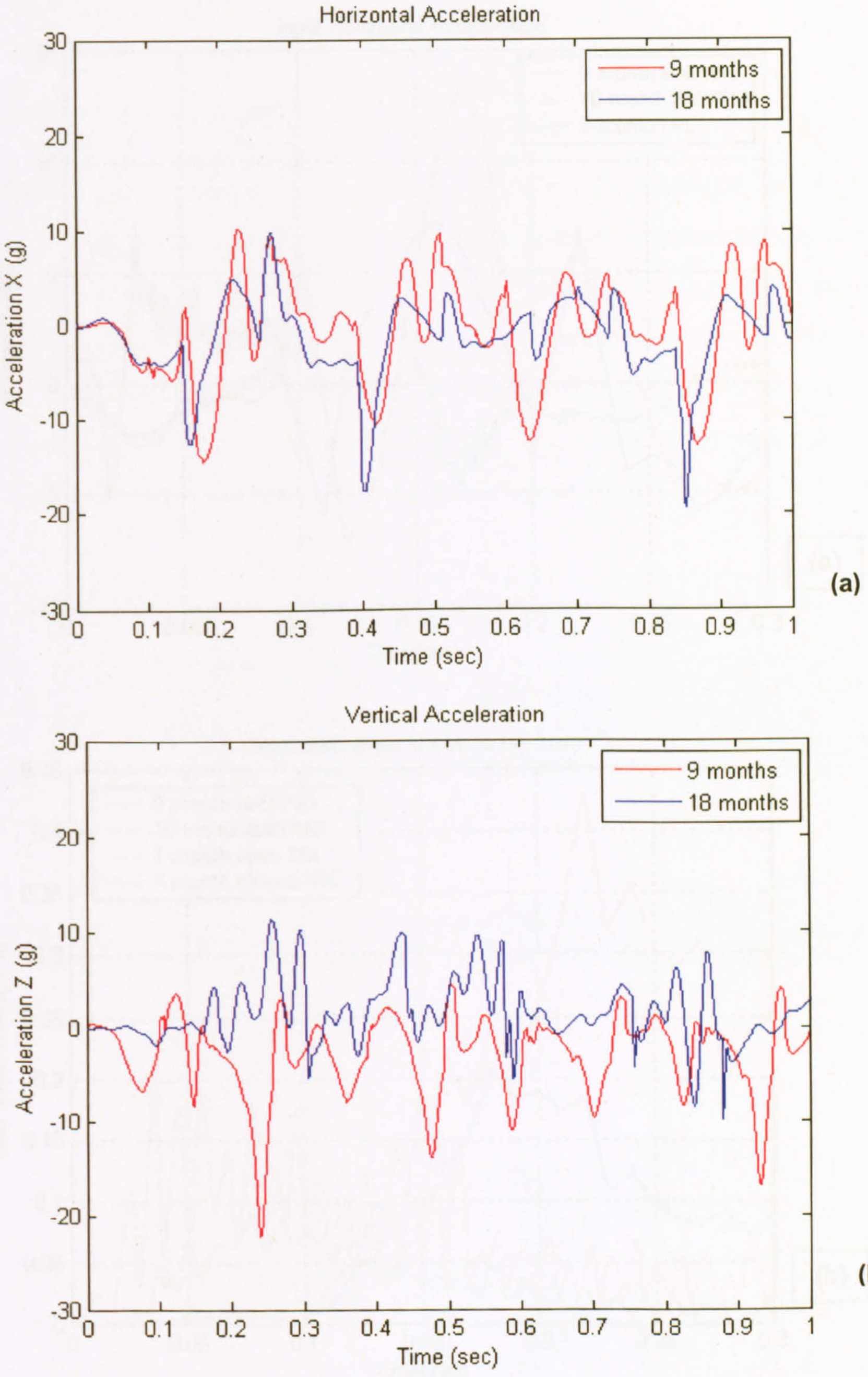

Figure H.3. *The acceleration collected from both 9 months and 18 months MADYMO model. (a) the horizontal acceleration; (b) the vertical acceleration.*

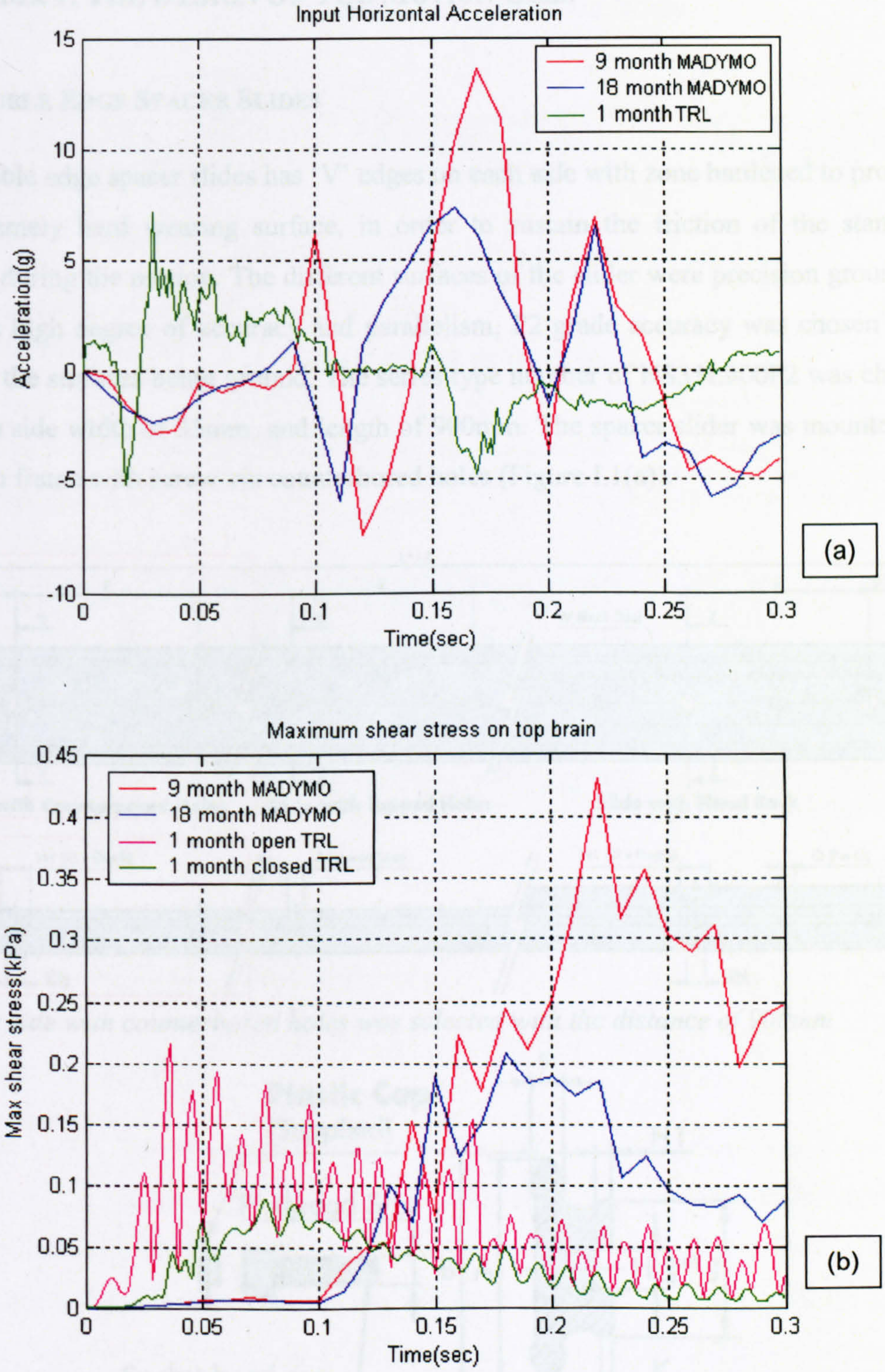

Figure H.4. *The comparison of the FE model between the excited motion from the MADYMO simulation and the TRL reconstruction. (a), the input data from MADYMO 9-months, MADYMO 18 months and TRL 9 months linear motion. (b), the shear stress on top of the brain in FE model.*

APPENDIX I: *THE DESIGN OF THE MOTION CELL*

I.1. DOUBLE EDGE SPACER SLIDES

The double edge spacer slides has 'V' edges on each side with zone hardened to provide an extremely hard wearing surface, in order to sustain the friction of the standard bearing during the motion. The different surfaces of the slider were precision ground to obtain a high degree of accuracy and parallelism, P2 grade accuracy was chosen with most of the surfaces being ground. The series type number of NS35L900P2 was chosen with the side width of 35mm, and length of 900mm. The spacer slider was mounted on the main frame with screw via counterbored holes (Figure I.1(a)).

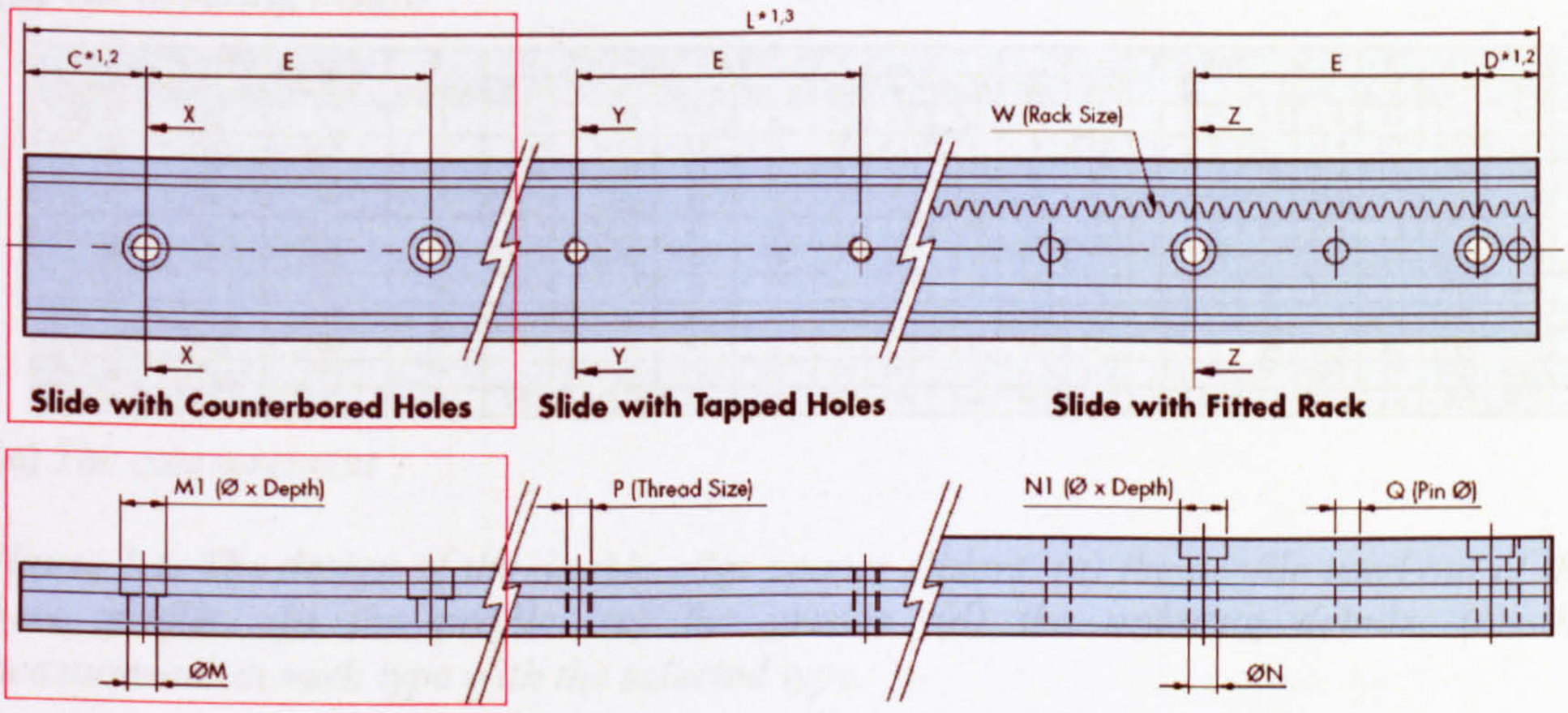

(a) *The side with counterbored holes was selected with the distance of 900mm*

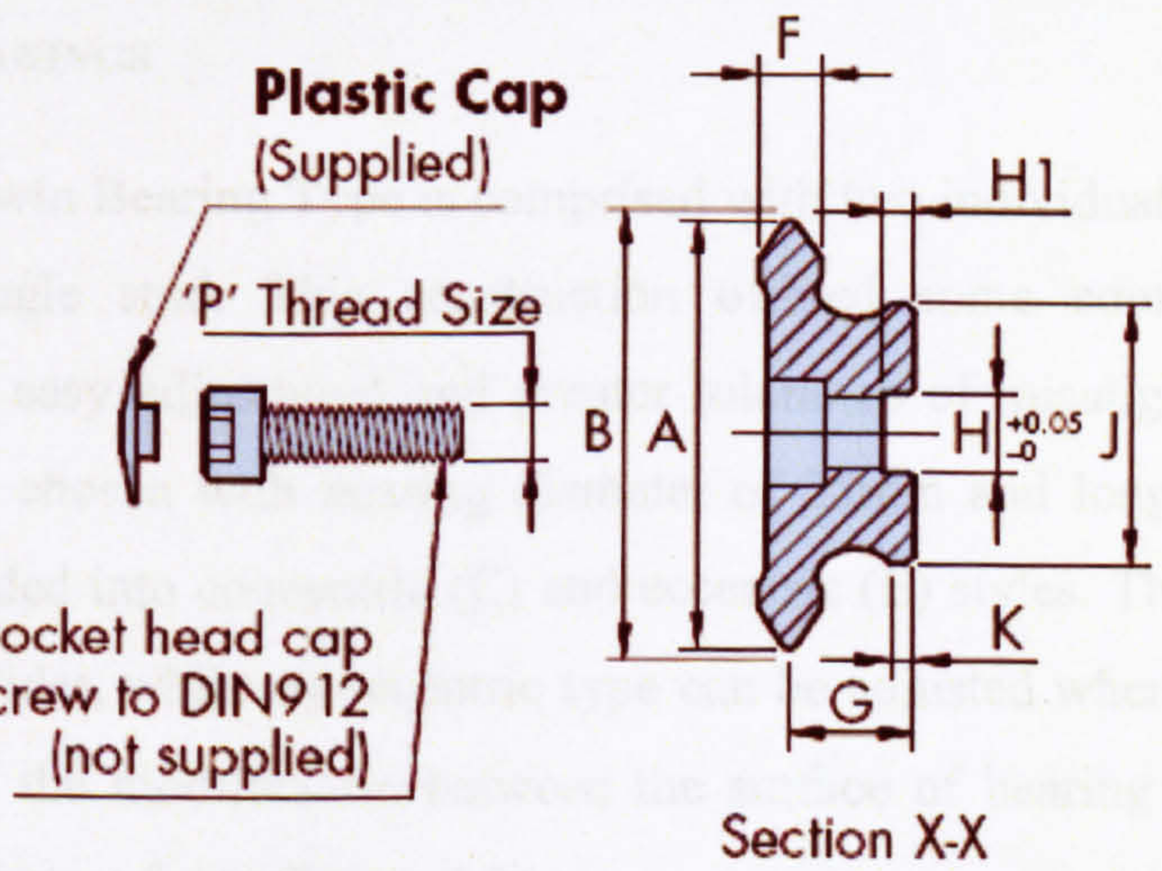

(b) *The cross section of double edge spacer sliders.*

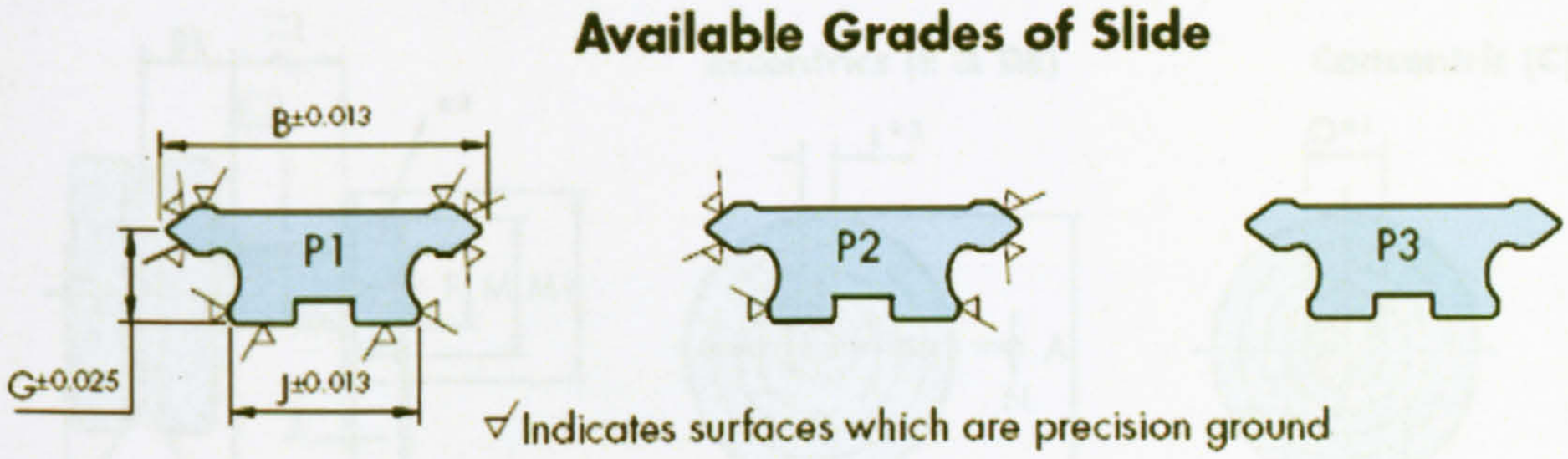

(c) *The available grades of slide, P2 is chosen.*

Ordering Details

NS35 L1290 P1 (R) (T) (C15) (D15)

Part Number
Slide Length 'L' = **1290** mm
Precision grade: options are **P1**, **P2** & **P3**
R - Rack mounted on Slide (not available on NMS12)
Leave blank if not required
Fixing hole style: **T** - tapped fixing holes; **N** - no holes
leave blank for counterbored holes (Options **T** & **N** are only available with Rack option to special order)
Bespoke values of 'C' & 'D' dimensions
Leave blank if standard*1,2

(d) *The ordering details*

Part Number	Use With Bearings*4		A	B		C & D*1,2		E	F		G		H	H1	J		K	L Max*1,3	
	Standard	Slimline	-Slide Width	P1 & P2	P3	Slide only	with rack	±0.2	P1	P2 & P3	P1	P2 & P3			P1 & P2	P3	Ø	P1 & P2	P3
NMS 12...	...J13...	-	12	12.37	13.25	20.5	-	45	3.0	3.2	6.2	6.4	4	1.8	8.5	8.9	1.7	1976	1976
NV 20...	...J18...	...J195...	20	20.37	21.01	43	15	90	4.21	4.42	8	8.2	5	2	12	12.4	1.75	4020	4020
NV 28...	...J18...	...J195...	28	28.37	29.01	43	15	90	4.21	4.42	8	8.2	6	2.5	20	20.4	1.75	4020	4020
NS 25...	...J25...	...J265...	25	25.74	26.58	43	15	90	4.71	4.93	10	10.2	6	2.5	15	15.4	2.6	4020	4020
NS 35...	...J25...	...J265...	35	35.74	36.38	43	15	90	4.71	4.93	10	10.2	8	3	25	25.4	2.6	4020	4020
NS 50...	...J25...	...J265...	50	50.74	51.38	43	15	90	4.71	4.93	10	10.2	10	3.5	40	40.4	2.6	4020	4020
NM 44...	...J34...	...J360...	44	44.74	45.58	43	15	90	6.21	6.42	12.5	12.7	8	3	26	26.4	2.3	4020	6000
NM 60...	...J34...	...J360...	60	60.74	61.38	43	15	90	6.21	6.42	12.5	12.7	10	3.5	42	42.4	2.3	4020	6000
NM 76...	...J34...	...J360...	76	76.74	77.38	43	15	90	6.21	6.42	12.5	12.7	12	4	58	58.4	2.3	4020	6000
NL 76...	...J54...	...J580...	76	76.74	77.58	88	30	180	9.21	9.43	19.5	19.7	15	5	50	50.4	4.8	4020	6000
NL 120...	...J54...	...J580...	120	120.74	121.38	88	30	180	9.21	9.43	19.5	19.7	45	9.5	94	94.4	4.8	4020	6000

(e) *The measurement*

Figure I.1. *The design of the double edge spacer sliders. (a) the profile used out of the three profile, (b) the profile, (c) the grades, (d) the ordering details, (e) the measurement in each type with the selected type.*

I.2. THE TWIN BEARINGS

The Hepco GV3 Twin Bearing Type is comprised with two individual deep groove ball bearings on a single stud. This construction offered some compliance allowing smoother running, easy adjustment and greater tolerance of misalignment. LJ25C(E) series bearing was chosen with bearing diameter of 25mm and long stud of 13mm. Each size was divided into concentric (C) and eccentric (E) styles. The concentric type was fixed on the slider, while an eccentric type can be adjusted when contact with the slider. This allows the modification between the surface of bearing and the slider to obtain the proper contact force (Figure I.2).

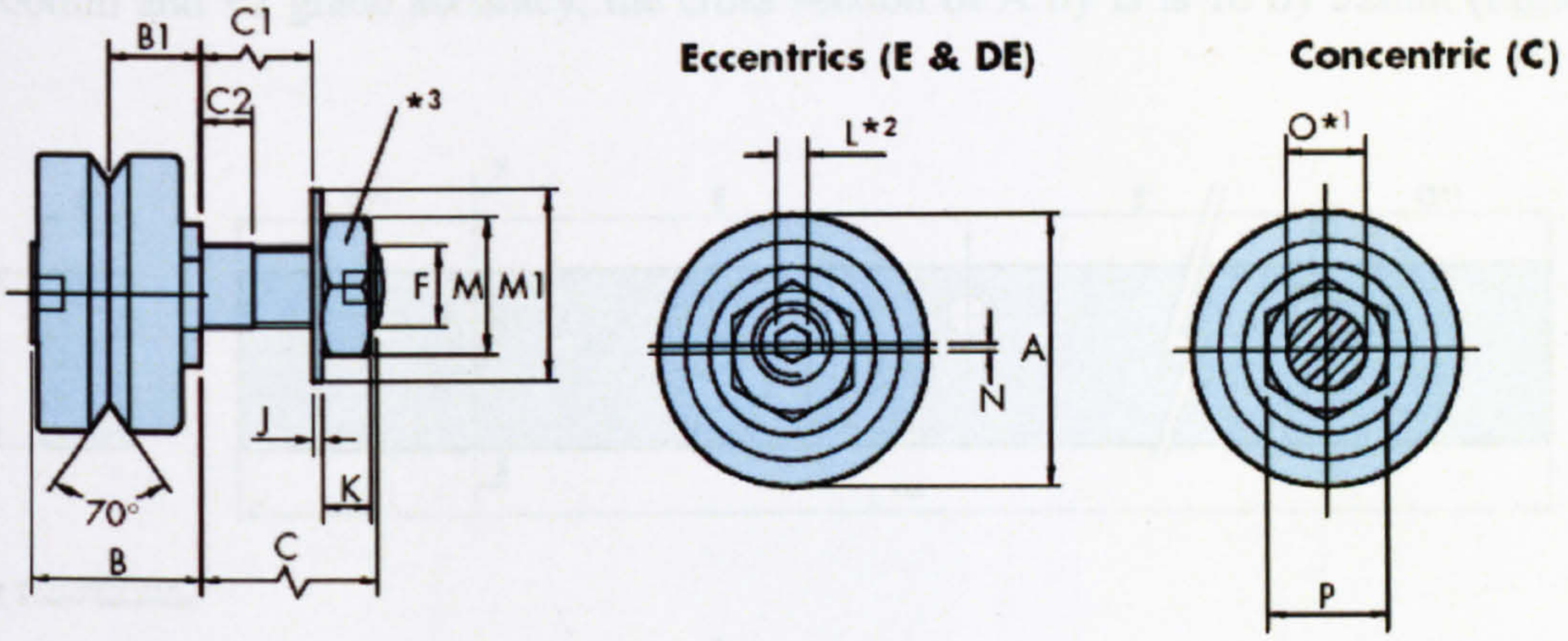

(a) *The profile of the twin bearings with eccentric and concentric type.*

Ordering Details

LJ 25 C (DR) (NS) (CH)

Fixing type. Choose from:
SJ = Short Stud, **LJ** = Long Stud
& **BHJ** = Blind Hole Fixing
Part Number (~ Bearing Diameter in mm)
C = Concentric (fixed), **E** = Eccentric (adjustable)
or **DE** = Double Eccentric (for disengagement purposes)

Controlled Height[*7]
Leave blank if not required
Nitrile Sealed Bearing
Leave blank if metal shields are required
Double Row Bearing
Leave blank if **Twin Bearing** is required

(b) *The ordering details*

Part Number	Use With Slide Section[*9]	A	B	±0.025 B1	C		C1		C2		±0.025 D	D1
					Short Stud	Long Stud	Short Stud	Long Stud	Short Stud	Long Stud		
...J13...	MS & NMS	12.7	10.1	5.47	5.8	9.5	3	6.7	2.2	2.4	9.51	4.76
...J18...	V & NV	18	12.4	6.75	7.4	14	3.4	10	2.4	2.5	14.0	7.0
...J25...	S & NS	25	16.6	9	9.8	19	3.8	13	3.4	4.9	20.27	10.13
...J34...	M & NM	34	21.3	11.5	13.8	22	6.6	14.8	5.2	5.9	27.13	13.56
...J54...	L & NL	54	34.7	19	17.8	30	8.2	20.4	5.7	7.9	41.76	20.88

S1	T	T1	T2	±0.1 U	U1	V	W	X	Y	Z	Weight ~g SJ...	LJ...	BHJ...C	BHJ...E
6.6	8.5	3.75	6.75	30	47.5	8	20	M3	5.5	8	8	8	7	27
10.5	10	4	8	38	54	11	24.5	M4	7	7	19	20	18	45
9	12	5	10	50	72	14	32	M5	8.5	10	48	51	43	105
8.5	17.5	6.5	12.5	60	90.5	17	42	M6	10	14	115	120	105	235
16.4	23.5	10.5	18.5	89.5	133	25	62	M8	13	20	415	425	390	800

(c) *The measurement*

Figure I.2. *The design of the standard bearing, (a) the profile, (b) the ordering details, (c) the measurement and the selected type.*

I.3. THE FLAT TRACKS

Hepco GV3 Flat Tracks are made from high quality carbon steel and are hardened on all four faces to provide an extremely durable running surface. They were designed to be used with the Hepco range of Track Rollers. Flat Tracks are often used in conjunction with Hepco V slidings in large systems where the design can eliminate the requirement to set slides accurately parallel. The type of FT3216L 900P2 is chosen with the length

of 900mm and P2 grade accuracy, the cross section of A by B is 16 by 32mm (Figure I.3).

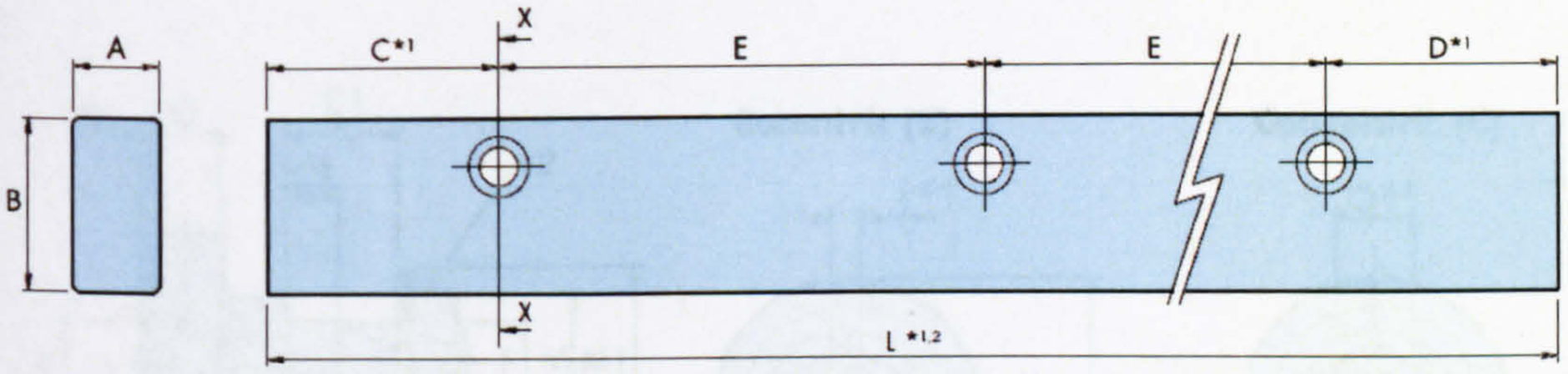

(a) *The profile of the flat tracks*

Ordering Details

FT4020 L1830 P2A C15 D15

Part Number
Track Length 'L' = **1830** mm
Precision grade: options are **P1**, **P2A**, **P2B** & **P3**
Bespoke values of 'C' & 'D' dimensions
Leave blank if standard (see table)

(b) *The ordering details*

Part Number	Use With Track Roller	A		B		C*1	D*1	E	F	G Ø	Screw Size	H Ø	J ~	K (min)	L*1,2 (max)	Weight kg/m
		P1 & P2A	P2B & P3	P1 & P2B	P2A & P3											
FT 24 12	...R 18...	12	12.4	24	24.4	20.5	20.5	45	7.5	6	M5	10	5	0.4	2000	2.3
FT 32 16	...R 25...	16	16.4	32	32.4	43	43	90	8.75	7	M6	11	6	0.4	4020	4
FT 40 20	...R 34...	20	20.4	40	40.4	43	43	90	12	9	M8	15	8	0.4	4020	6.3
FT 66 33	...R 54...	33	33.4	66	66.4	88	88	180	17	14	M12	20	12	0.4	4020	17

(c) *the measurement*

Figure I.3. *The design of the flat tracks (a) the profile and grade, (b) the ordering details, (c) the measurement and the selected type.*

I.4. THE NARROW TRACK ROLLER

The Hepco Narrow Track Rollers are used in conjunction with Hepco Flat Tracks, and almost any type of running surface. Each use a high capacity single row deep groove ball bearing with a substantial and stiff outer ring and a crowned outer profile. Narrow track rollers of type of LRN25C (E) are chosen with the diameter of 25mm. The LRN25 series has also be divided into concentric and eccentric type with the similar purpose with the twin bearing for assembly (Figure I.4). The Wide Track Rollers, as an

alternative option in the manual are used for high load capacity application which is not necessary in this design.

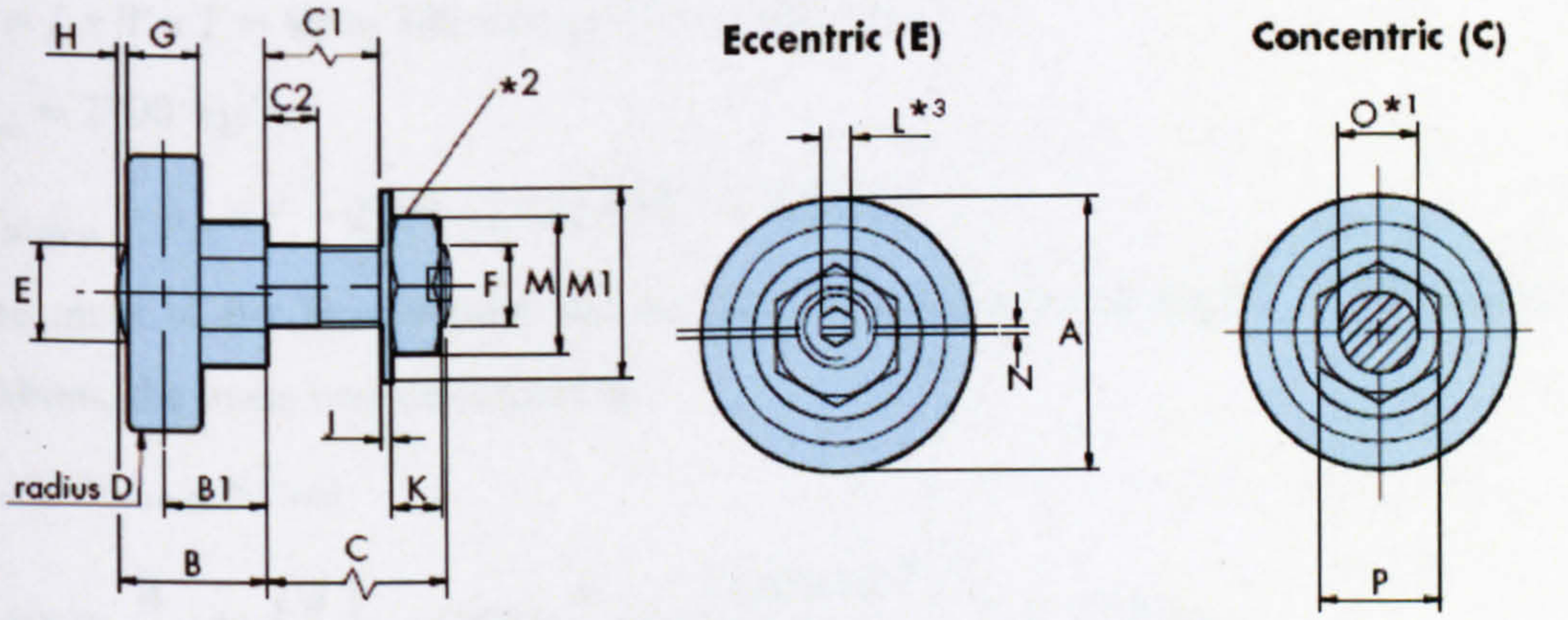

(a) *The profile of narrow track roller with eccentric and concentric type*

Ordering Details

LRN25 C (NS)

Part Number
LRN Indicates a Narrow Track Roller
25 denotes roller diameter in mm

Nitrile Sealed Bearings
Leave blank if metal shields are required
C = Concentric (fixed) or **E** = Eccentric (adjustable)

(b) *The ordering details*

Part Number	Use With Flat Track *5	A	B	B1	C	C1	C2	D	E	F Metric Fine	G	H	J	K
LRN 18 ...	FT 24 12	18	11.5	8	14	10	2.5	500	7	M6 x 0.75	5	1	0.8	3.2
LRN 25 ...	FT 32 16	25	14.5	10	19	13	5	500	10	M8 x 1	7	1	1	5
LRN 34 ...	FT 40 20	34	18.2	12.5	22	14.8	6	500	12	M10 x 1.25	9	1.2	1.25	6
LRN 54 ...	FT 66 33	54	29.5	21	30	20.4	8	500	23.5	M14 x 1.5	14	1.4	1.6	8

L*3	M	M1	N	+0 -0.03 O*1	P	Weight ~g	Max Working Load Capacity	Roller Static and Dynamic Radial Load Capacities (N)*4	
								Co	C
2.5	10	13	0.7	6	11	16	400	593	1438
3	13	17	0.75	8	13	40	1000	1333	3227
4	17	21	1	10	15	85	2000	2600	5921
6	22	28	1.5	14	27	310	5000	6657	13595

Part Number	Options Available	
	Metal Shields (-)	Nitrile Seals (NS)
LRN 18 ...	✗	✓
LRN 25 ...	✓	✓
LRN 34 ...	✓	✓
LRN 54 ...	✓	✓

(c) *The measurement*

Figure I.4. *The design of the flat track rollers, (a) profile, (b) ordering detail, (c) the measurement and the selected type.*

I.5. LOADING ON EACH BEARING

To calculate the life time distance of the system, the average loading on each bearing and roller has to be defined. The overall loading comes from the platform, and the experimental models as well as the support frames for camera mounted on the platform.

In the following calculation the platform was considered as a piece of aluminium bar with the dimension of length by width by thickness equal to 460mm by 300mm by 19mm:

$$V = L \times W \times T = 460 \times 300 \times 19 \times 10^{-9} = 2.622 \times 10^{-3} \text{ m}^3 \quad \text{(I.1)}$$

$$\rho_{Al} = 2700 \text{ kg/ m}^3 \quad \text{(I.2)}$$

$$m_{platform} = \rho_{Al} \times V = 2700 \times 2.622 \times 10^{-3} = 7.08 \text{ kg} \quad \text{(I.3)}$$

The mass of the head model can be considered as a water sphere, if the diameter is 100mm, the mass was calculated as:

$$m_{d100} = \rho_{water} \times V_{d100}$$

$$= 1000 \times \frac{4}{3} \times \pi \times \left(\frac{d}{2}\right)^3 = 1000 \times \frac{4}{3} \times \pi \times \left(\frac{100 \times 10^{-3}}{2}\right)^3 = 0.5236 \text{ kg} \quad \text{(I.4)}$$

Alternatively, the mass with diameter 150mm was calculated as:

$$m_{d150} = \rho_{water} \times V_{d150}$$

$$= 1000 \times \frac{4}{3} \times \pi \times \left(\frac{d}{2}\right)^3 = 1000 \times \frac{4}{3} \times \pi \times \left(\frac{150 \times 10^{-3}}{2}\right)^3 = 1.7671 \text{ kg} \quad \text{(I.5)}$$

Beside the model, an aluminium frame was designed as the support frame of the cameras. The mass of the frame is equal to the total length of the aluminium extrusion multiplied by 0.4 from the user's manual (Bosch Rexroth AG 2005).

$$l_{frame} = h \times 4 + l \times 4 + w \times 6 + l_1 \times 2$$

$$= 400 \times 4 + 290 \times 4 + 180 \times 6 + 180 \times 2 = 4200 \text{ mm} \quad \text{(I.6)}$$

Where l_{frame} is the total length of the aluminium extrusion.

$$m_{frame} = 0.4 \times l_{frame} = 0.4 \times 4.2 = 1.68 \text{kg} \quad \text{(I.7)}$$

Therefore the mass of the aluminium frame is 1.68kg.

Combining all the mass of aluminium bar, the model with 150mm diameter and the aluminium frame, the overall mass that the pneumatic system will sustain can be calculated as:

$$m_{\max} = m_{platform} + m_{d150} + m_{frame} = 7.08 + 1.77 + 1.68 = 10.53 \text{ kg} \quad \text{(I.8)}$$

$$L_R = 0.25 G_{\max} = 0.25 m_{\max} g = 0.25 \times 10.53 \times 9.81 = 25.82 \text{ N} \quad \text{(I.9)}$$

Hence the individual V bearing was calculated followed the Figure 4.9:

$$L_F = \frac{L_A}{L_{A(\max)}} + \frac{L_R}{L_{R(\max)}} = \frac{L_A}{100} + \frac{L_R}{200} = \frac{0}{100} + \frac{25.82}{200} = 0.13 \quad \text{(I.10)}$$

where J25 $L_{A(max)}$=100, $L_{R(max)}$=200.

$$L_{life} = \frac{BasicLife}{(0.03 + 0.97L_F)^2} = \frac{70}{(0.03 + 0.97 \times 0.13)^2} = 2872.71\,\text{km} \quad \text{(I.11)}$$

Where basic life is 70 km.

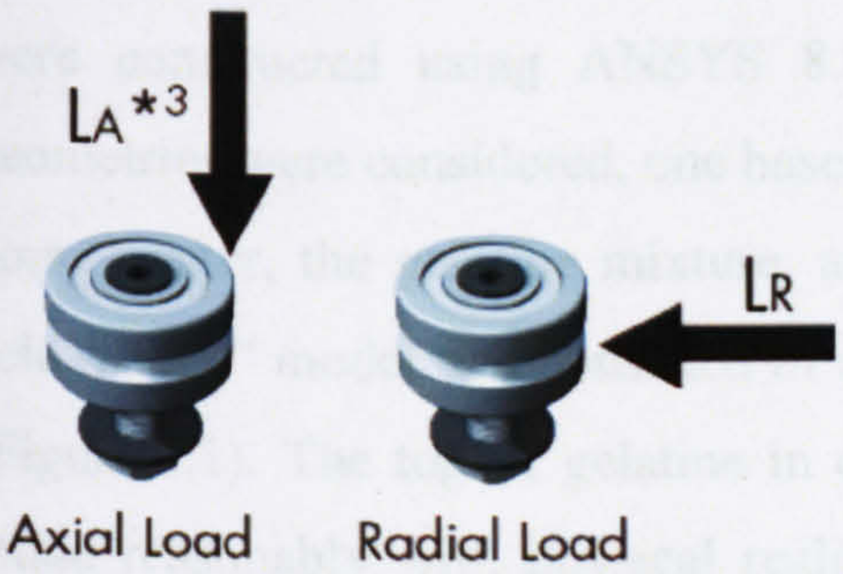

Load Capacities for Twin Standard Bearings				
Bearing Part Numbers	Dry		Lubricated	
	LA (max) N	LR (max) N	LA (max) N	LR (max) N
..J 13...	22.5	45	60	120
..J 18...	45	90	125	200
..J 25...	100	200	320	600
..J 34...	200	400	800	1400
..J 54...	450	900	1800	3200

Figure I.5. *V bearing calculation.*

The individual track roller was calculated following the Figure (I.6):

The load factor L_F for roller life should be calculated using the equation below.

$$L_F = \frac{L_R}{L_{R(\max)}} = \frac{25.82}{1000} = 0.025 < 1 \quad \text{(I.12)}$$

The L_F should not exceed 1.

With L_F determined for each roller, the life in km can be calculated using the equation below. The Basic Life for all Track Rollers is 1000 km.

$$L_{life} = \frac{1000}{L_F{}^3} = \frac{1000}{0.025^3} = 6.4 \times 10^7 \text{ km} \quad \text{(I.13)}$$

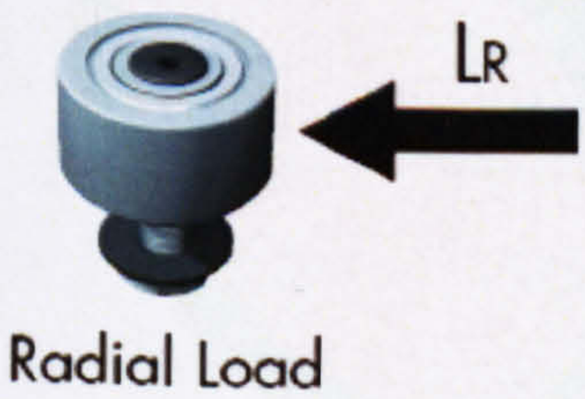

Load Capacities for Track Rollers				
Narrow Rollers	LR (max) N		Wide Rollers	LR (max) N
LRN 18...	400		...R 18...	600
LRN 25...	1000		...R 25...	1600
LRN 34...	2000		...R 34...	3200
LRN 54...	5000		...R 54...	8000

Figure I.6. *Track roller calculation.*

APPENDIX J: *FINITE ELEMENT METHODS OF THE RIG TESTS-3D MODEL*

J.1. FINITE ELEMENT METHOD OF THE RIG TESTS-3D MODELLING

The finite element (FE) models of the three-dimensional spherical rig head structures were constructed using ANSYS 8.0 (ANSYS Inc., Houston, PA) software. Two geometries were considered, one based on the "open top" model and consisted of a rigid dome, water, the gelatine mixture, and a latex membrane. The other is based on the "closed top" model and consisted of only a rigid dome, water, and the gelatine mixture (Figure J.1). The top of gelatine in open geometry was modelled as a flat surface to relate reasonably with physical reality and for ease of mesh generation. Inside both models, the water and gelatine were modelled by 10104 eight-noded linear brick elements. The rigid dome as well as the membrane in "open top" was modelled by using 695 four-noded shell elements.

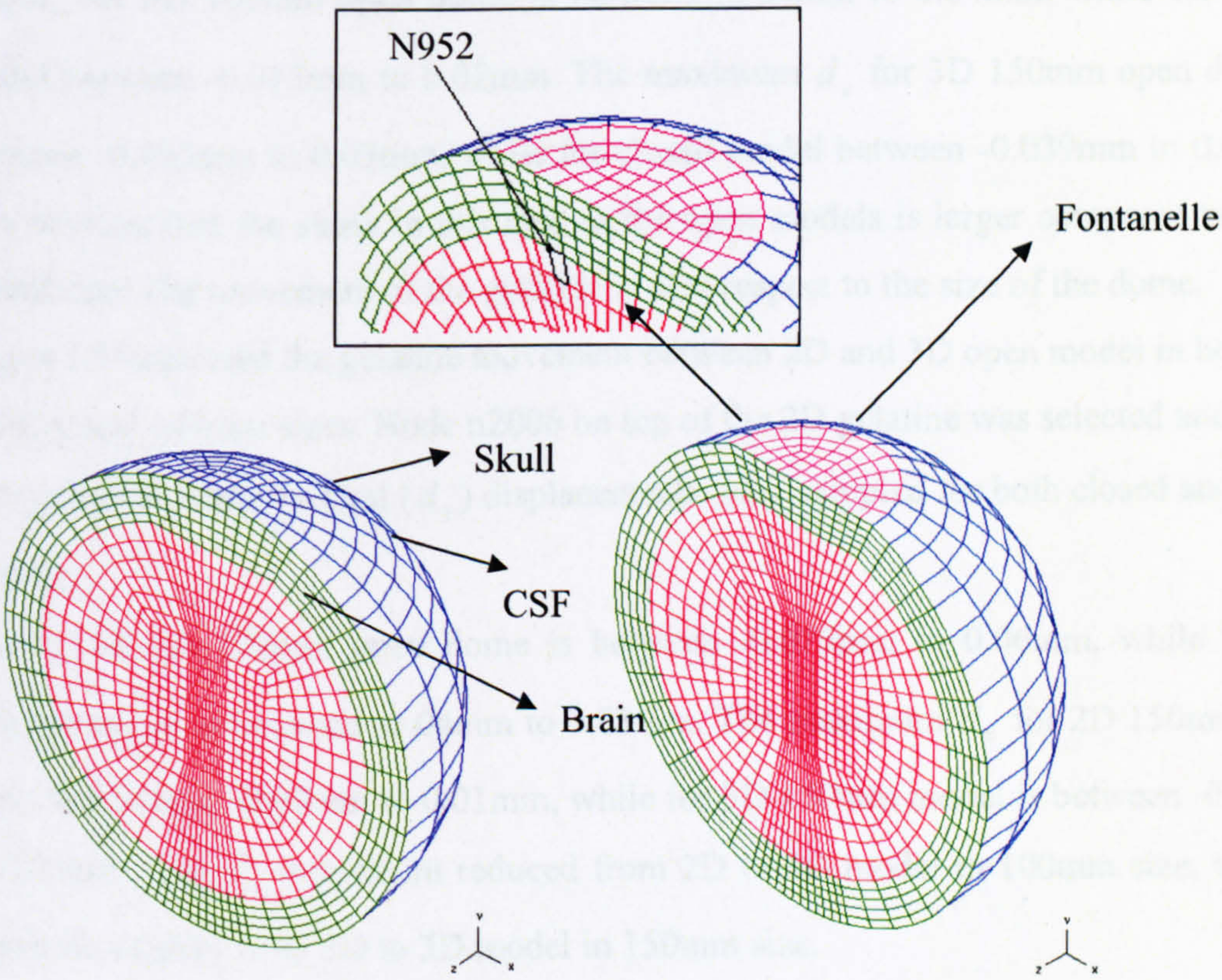

Figure J.1. *The cross section view of the 3D spherical model of open and closed dome.*

Two geometric sizes were involved, with one using the 100mm diameter and another using the 150mm diameter for both open and closed models.

The two-dimensional models of the sagittal plane of rig head structure were generated and had the same components, geometry, and fluid structure interaction with the 3D models (Chapter 8 Figure 8.1, page 175).

The material constitutive model and the loading condition are the same with the 2D model discussed in Chapter 7 (§7.1.2, §7.1.5), therefore the details will not be given in the appendix.

The 2D and the 3D model for 150mm diameter are discussed here.

J.2. RESULT

Figure J.2 shows the gelatine displacements predicted by the 3D FE models. Node n952 on top of the gelatine was selected and its horizontal (d_x) and vertical (d_y) displacements were sampled for both closed and open models.

The d_x for 3D 100mm open dome is between -0.04mm to 0.04mm, while for closed model between -0.015mm to 0.02mm. The maximum d_x for 3D 150mm open dome is between -0.055mm to 0.03mm, while for closed model between -0.039mm to 0.03mm. It is obvious that the strain in this area in the open models is larger compared with the closed one. The movement of the gelatine is also respect to the size of the dome.

Figure J.3 examined the gelatine movement between 2D and 3D open model in both 123mm and 144mm sizes. Node n2006 on top of the 2D gelatine was selected and its horizontal (d_x) and vertical (d_y) displacements were sampled for both closed and open models.

The d_x for 2D 100mm open dome is between -0.075mm to 0.06mm, while for 3D 100mm model is between -0.04mm to 0.03mm. The maximum d_x for 2D 150mm open dome is between -0.03mm to 0.01mm, while for 3D 150mm model is between -0.05mm to 0.02mm. The d_x movement reduced from 2D to 3D model in 100mm size, while it increases slightly from 2D to 3D model in 150mm size.

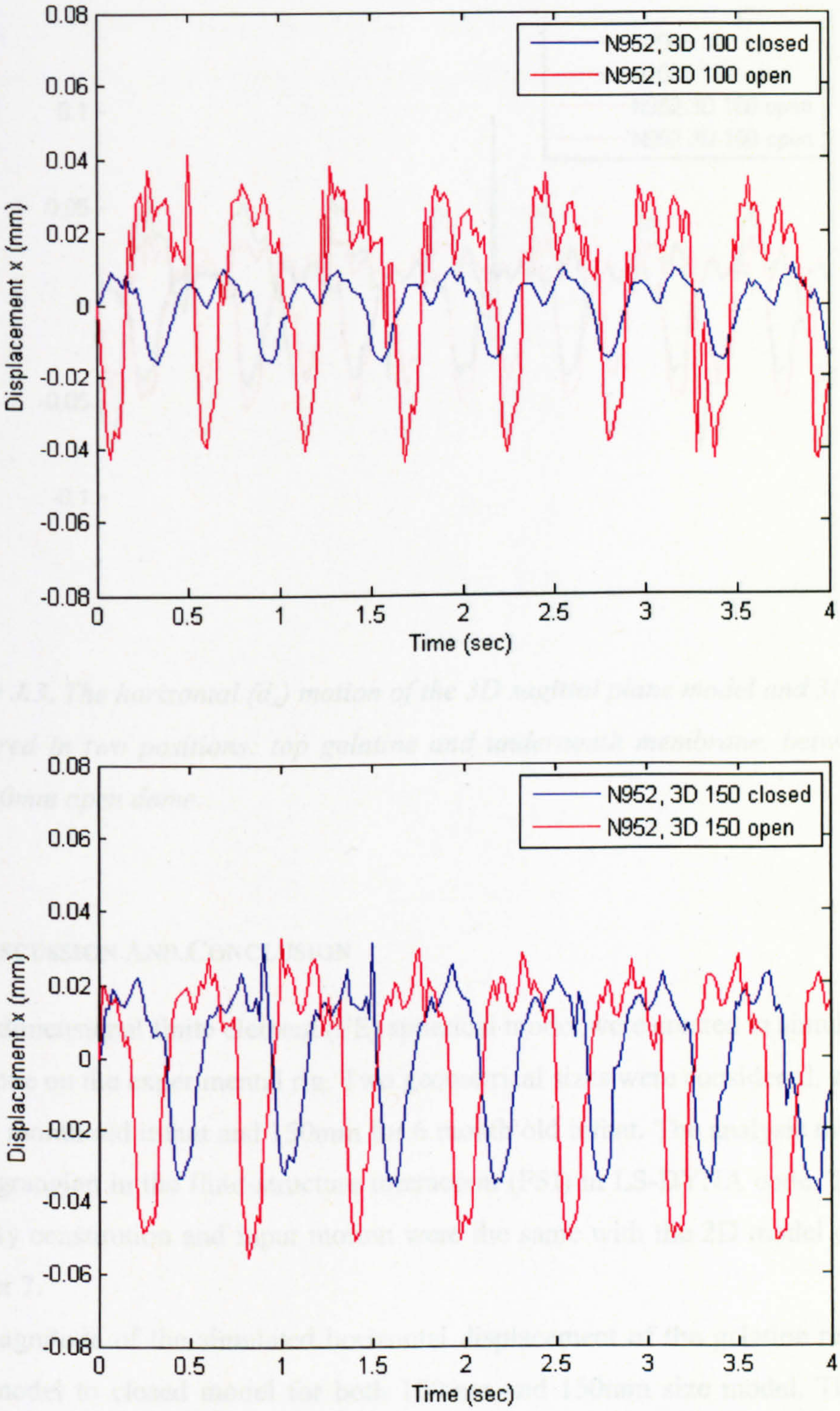

Figure J.2. *The x displacement of top gelatine n2006 and underneath membrane n952 in both 100mm and 150mm model, the domes with open and closed top are compared.*

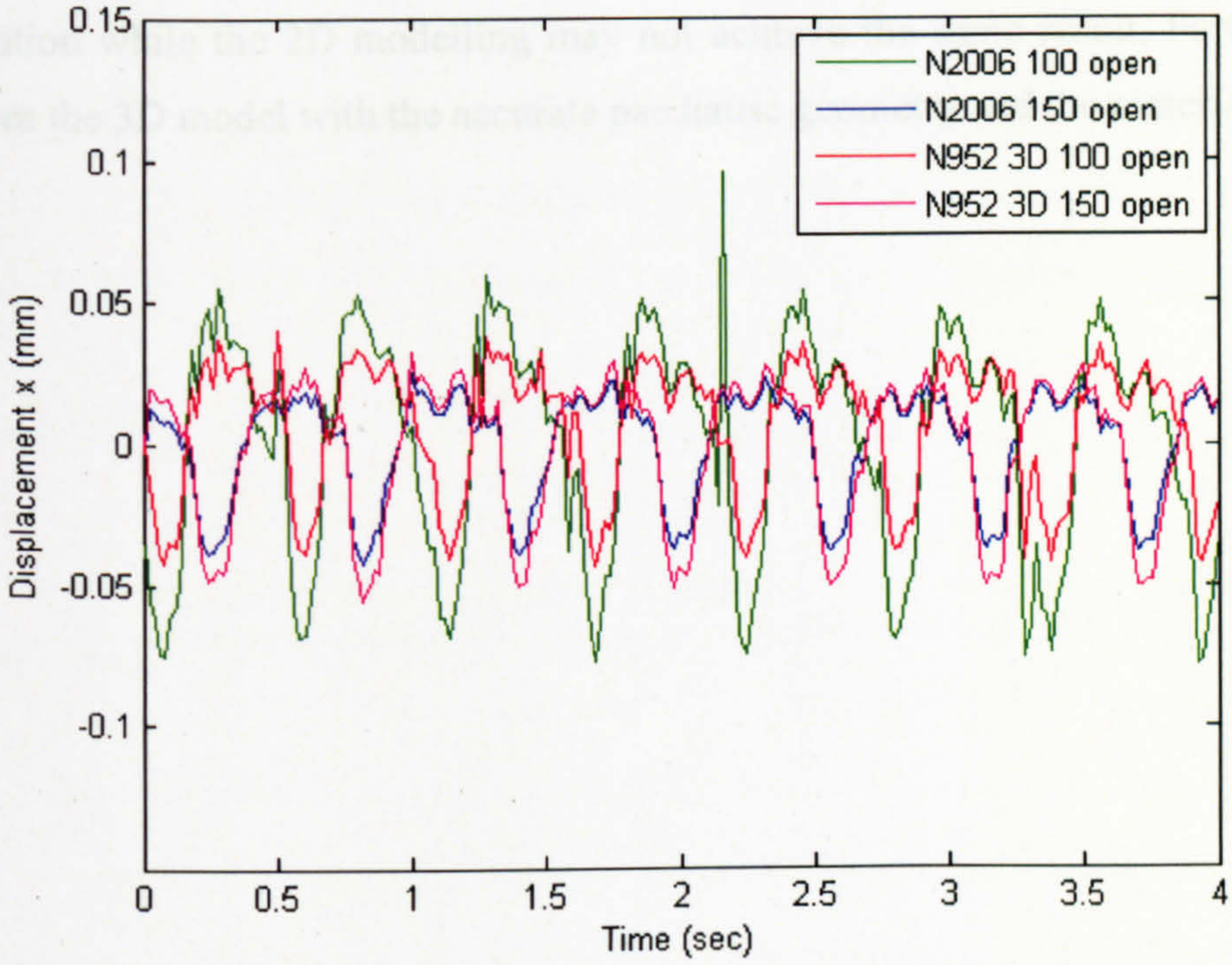

Figure J.3. *The horizontal (d_x) motion of the 3D sagittal plane model and 3D model are compared in two positions: top gelatine and underneath membrane, between 100mm and 150mm open dome.*

J.3. DISCUSSION AND CONCLUSION

Three-dimensional finite element (FE) spherical model were created in simulation of the tests done on the experimental rig. Two geometrical sizes were considered, with 100mm for 1.5 month old infant and 150mm for 6 month old infant. The analysis methods were the Lagrangian in the fluid-structure interaction (FSI) in LS-DYNA code. The material property constitution and input motion were the same with the 2D model discussed in Chapter 7.

The magnitude of the simulated horizontal displacement of the gelatine reduced from open model to closed model for both 100mm and 150mm size model. Therefore the strain in this area in the open models is larger than the closed model. The movement of the gelatine is also respect to the size of the dome. The magnitude of the horizontal displacement in 150mm model is larger than the 100mm model. The horizontal displacement of the gelatine reduced from 2D to 3D model in 100mm size, while it increases slightly from 2D to 3D model in 150mm size. The reduction of the strain from

2D to 3D model shows the importance of the 3D modelling during the complicated simulation while the 2D modelling may not achieve the same result. Further analysis requires the 3D model with the accurate paediatric geometry and the material property.

APPENDIX K: *MATERIAL PROPERTIES IN THE FINITE ELEMENT MODEL*

E=Young's modulus (MPa); ρ=mass density (kg/m^3); υ=Poisson's ratio; K=bulk modulus (MPa); G_0=short term shear modulus (MPa); G_∞=long term shear modulus (MPa); β=decay factor (s^{-1}) ; σ_y =yield stress (MPa); E_t = tagent stress (MPa)

Author	Brain						
	G_0 MPa	G_∞ MPa	ρ kg/m^3	β s^{-1}	E MPa	υ	K MPa
(1)Hardy 1973	-	-	-	-	-	-	-
(1)Nickell 1974	-	-	-	-	-	-	-
(1)Shugar (1975)	-	-	-	-	-	-	-
(1)Khalil (1977)	-	-	-	-	-	-	-
(1)Ward (1978)	66.7×10^{-3}	-	-	-	-	0.48	-
(1)Hosey (1982)	66.7×10^{-3}	-	-	-	-	0.499	-
Ruan (1991)	-	-	1040		6.67×10^{-2}	0.48	2190
Ruan(1994)	1.68	-	1040	-	-	0.4996	2190
Willinger (1995)	-	-	1140	-	6.67×10^{-2}	0.48	-
(1)Kumaresan (1996)	66.7×10^{-3}	-	-	-	-	0.499	-
Margulies (2000)	5.99×10^{-3}	2.32×10^{-3}	1000	0.09248	-	-	2110
Kleiven (2002)	-	-	-	1.04	Hyper-elastic	0.49999635	-
Aomura (2003)	-	-	-	-	-	-	-
Canaple(2003)	5.28×10^{-1}	1.68×10^{-1}	-	0.035	-	-	21.9
Horgan(2003)	-	-	1040	-	Hyper-elastic	0.4999981	-

(1) Cited from Voo (1996)

Table K.1. *The material properties of the brain in the FE models.*

Author	Skull						
	G MPa	K MPa	ρ kg/m^3	σ_y MPa	E MPa	ν	E_t Mpa
[1]Hardy(1973)	-	-	-	-	[2]3.4×10^3	-	-
	-	-	-	-	[3]1.0×10^3	-	-
[1]Nickell(1974)	-	-	2100	-	[2]4.14×10^3	-	-
	-	-	2100	-	[3]1.04×10^3	-	-
[1]Shugar(1975)	-	-	1400	-	5.66- 12.2×10^3	0.22	-
[1]Khalil (1977)	-	-	2997	-	[2]1.79×10^3	0.35	-
	-	-	1744	-	[3]0.73×10^3	0.05	-
[1]Ward (1978)	-	-	-	-	-	-	-
[1]Hosey (1982)	-	-	1410	-	4.46×10^3	0.21	
Ruan (1991)	-	-	1412	-	6.5×10^3	-	-
Ruan (1994)		7.3×10^3	3000	-	-	-	-
		3.4×10^3	1750	-	-	-	-
		7.3×10^3	3000	-	-	-	-
Willinger(1995)	-	-	1500	-	5.0×10^3	0.21	-
[1]Kumaresan (1996)			1410		4.46×10^3	0.21	
Margulies (2000)	-	-	2150	-	1.3×10^3	-	0.28
Kleiven (2002)	-	-	2000	-	1.5×10^4	0.22	-
Aomura (2003)	3.47×10^3	7.12×10^3	1456	41.8	-	-	4.62×10^3
Canaple(2003)	-	-		-		-	-
Horgan (2003)	-	-	2000	-	1.5×10^4	0.22	-

(1) Cited from Voo (1996); (2) Outer and inner layer; (3) diplöe

Table K.2. *The material properties of the skull in the FE models.*

Author	CSF						
	E MPa	K MPa	ρ kg/m^3	G_0 MPa	G_∞ MPa	υ	β S^{-1}
(1)Hardy (1973)	-	-	-	-	-	-	-
(1)Nickell (1974)	-	-	-	-	-	-	-
(1)Shugar (1975)	-	2190	-	-	-	-	-
(1)Khalil (1977)	-	2190	-	-	-	-	-
(1)Ward (1978)	-	-	-	-	-	0.48	-
(1)Hosey (1982)	-	-	-	-	-	0.499	-
Ruan (1991)	6.67×10^{-2}	-	1040	-	-	0.499	-
Ruan (1994)	-	21.9	1040	5.0×10^{-1}	-	0.489	-
	-	2190	1040	-	-	0.4996	-
Willinger (1995)	1.0×10^{-2}	-	1040	-	-	0.499	-
	1.0×10^{-1}	-	1040	-	-	0.49	-
(1)Kumaresan (1996)	-	-	-	-	-	0.499	-
Margulies(2000)	-	-	-	-	-	-	-
Kleiven (2002)	-	-	-	-	-	-	-
Aomura (2003)	-	2.19×10	1040	5.28×10^{-1}	5.00×10^{-1}	-	5
Canaple(2003)	-	2000	1000	-	-	0.49	-
Horgan (2003)	-	-	-	-	-	-	-

(1) Cited from Voo (1996)

Table K.3. *The material properties of the CSF in the FE models.*

Author	Membrane		
	E MPa	ρ kg/m^3	υ
[1]Hardy (1973)	-	-	-
[1]Nickell (1974)	-	-	-
[1]Shugar (1975)	-	1030	-
[1]Khalil (1977)	-	1030	-
[1]Ward (1978)	[2]31.5	1140	0.45
	[3]31.5	1040	0.45
[1]Hosey (1982)	31.5	1040	0.45
	-	1133	-
Ruan (1991)	31.5	1133	0.45
Ruan (1994)	-	1040	-
[1]Kumaresan (1996)	[3]31.5	1040	0.45
	-	1133	-
Margulies (2000)	200	2150	0.28
Kleiven (2002)	[2]16.7	1130	0.45
	[3]31.5	1130	0.45
Aomura (2003)	16.7	1200	0.42
Canaple (2003)	-	-	-
Horgan (2003)	[2]16.7	1000	0.42
	[3]31.5	1130	0.45
	[4]11.5	1130	0.45

(1) Cited from Voo (1996); (2)-Scalp; (3)-Dura; (4)-Pia

Table K.4. *Material properties of the membrane in the FE models.*

APPENDIX L: *LS-DYNA INPUT DECK FOR THE FE MODELS OF THE RIG TESTS*

L.1. LAGRANGIAN MODEL

```
*KEYWORD
$
*TITLE
$
$ =============
$ CONTROL cards
$ =============
$
*CONTROL_TERMINATION
      6.68          0        0.0        0.0        0.0
$
$ ==============
$ DATABASE cards
$ ==============
$
*DATABASE_BINARY_D3DUMP
    250000
*DATABASE_BINARY_D3PLOT
    2.0E-2          0          0          0
*DATABASE_BINARY_D3THDT
    2.0E-2          0
*DATABASE_BINARY_RUNRSF
    100000          0
*DATABASE_EXTENT_BINARY
         0          0          3          1          1          1          1          1
         0          0          0          0          0          0          0
$
$ Cross-reference summary for SET_NODE 1
$ ---------------------------------------
$ DATABASE_HISTORY <No label>
```

```
$
*SET_NODE_LIST
         1       0.0       0.0       0.0       0.0
       ...
      1264      1726      1278      1581      1670         2       509       253
$
$
*DATABASE_HISTORY_NODE_SET
         1
$
$ Cross-reference summary for SET_SHELL 1
$ ------------------------------------
$ DATABASE_HISTORY <No label>
$
*SET_SHELL_LIST
         1       0.0       0.0       0.0       0.0
      1242      1241      1240      1239      1238      1237      1236      1235
      1197      1233      1186      1207
$
$
*DATABASE_HISTORY_SHELL_SET
         1
$
$ Cross-reference summary for SET_SOLID 1
$ ------------------------------------
$ DATABASE_HISTORY <No label>
$
*SET_SOLID
         1
      1009      1001       993       985       977       969       961       953
      1033       552       576       600       929       905       881       857
       385       990      1046       926       658       721       792       664
       785
$
$
*DATABASE_HISTORY_SOLID_SET
         1
```

```
$
$
$ ====================
$ MAT (Material) cards
$ ====================
$
*MAT_VISCOELASTIC
         1   1.04E-9    2110.0   5.99E-3   2.32E-3  9.248E-2
$
*MAT_ELASTIC_FLUID
         2    1.0E-9       0.0       0.0       0.0       0.0    2110.0
       0.1    1.0E20
$
*MAT_RIGID
         3   2.15E-9    1300.0      0.28       0.0       0.0       0.0
       1.0       5.0       7.0
         0       0.0       0.0       0.0       0.0       0.0
$
*MAT_ELASTIC
         4   4.4E-10      0.42      0.42       0.0       0.0       0.0
$
$
$
$ =============
$ SECTION cards
$ =============
$
*SECTION_SHELL
         3         2       0.0         0       0.0       0.0         0         0
       2.0       2.0       2.0       2.0       0.0       0.0
$
         4         2       0.0         0       0.0       0.0         0         0
       0.1       0.1       0.1       0.1       0.0       0.0
$
*SECTION_SOLID
         1         1         0
$
```

```
         2          0          0
$
$
$
$ ==========
$ PART cards
$ ==========
$
*PART
$HMNAME COMPS        1FILL_EL
FILL_EL
         1          1          1          0          0          0          0          0
$
*PART
$HMNAME COMPS        2WATER_EL
WATER_EL
         2          2          2          0          0          0          0          0
$
*PART
$HMNAME COMPS        3COVER3_E
COVER3_E
         3          3          3          0          0          0          0          0
$
*PART
$HMNAME COMPS        4SKIN_EL
SKIN_EL
         4          4          4          0          0          0          0          0
$
$
$
$ ==========
$ NODE cards
$ ==========
$
*NODE
         1      -28.288544        28.288544              0.0          3          0
       ...
```

```
    6840       13.683820       44.405098      -5.0000000       3       0
$
$
$ =============
$ ELEMENT cards
$ =============
$
*ELEMENT_SHELL
    1179       3       45       61       76       46
      ...
    1242       4     2173     2186      218      213
*ELEMENT_SOLID
       1       2        1       19       20        3       77       84      145       85
      ...
    1088       2     2190     2218      222      217     2173     2186      218      213
$
$
$ ============
$ DEFINE cards
$ ============
$
$
*DEFINE_CURVE
$
$ Cross-reference summary for Load-curve 1
$ ------------------------------------------------
$
$ Usage: Transient analysis
$
         1          0       1.0       1.0       0.0       0.0          0
                  0.0          -1342.8000
                                  ...
             4.0000000           1147.4000
$
$
*DEFINE_CURVE
$
```

```
$ Cross-reference summary for Load-curve 2
$ ------------------------------------------
$
$ Boundary Prescribed Motion <No label>: Velocity vs time
$ X axis : Time                          (Units: Time)
$ Y axis : Prescribed velocity           (Units: Velocity)
$
$ Usage: Transient analysis
$
         2         0       1.0       1.0       0.0       0.0         0
                 0.0          -48.799999
                                  ...
           6.6799998          -1001.0000
$
$
$ ==============
$ BOUNDARY cards
$ ==============
$
*BOUNDARY_PRESCRIBED_MOTION_RIGID
         3         1         0         2       0.0         0       0.0       0.0
$
$
$ =============
$ INITIAL cards
$ =============
$
*INITIAL_VELOCITY_GENERATION
         0         0       0.0     -48.8       0.0       0.0
       0.0       0.0       0.0       0.0       0.0       0.0         0
$
$ =========
$ SET cards
$ =========
$
$
*END
```

L.2. 1-POINT ALE MODEL

```
*KEYWORD
$>
$
*TITLE
$
$ =============
$ CONTROL cards
$ =============
$
*CONTROL_ALE
         2        10         1       0.1       0.0       0.0       1.0       0.0
       0.0       0.0       0.0       0.0       0.0         0       0.0         0
*CONTROL_TERMINATION
       4.0         0       0.0       0.0       0.0
*CONTROL_TIMESTEP
       0.0      0.67         0       0.0       0.0         0         0         0
$
$
$ ==============
$ DATABASE cards
$ ==============
$
*DATABASE_BINARY_D3PLOT
    2.0E-3         0         0         0
*DATABASE_BINARY_D3THDT
    2.0E-3         0
*DATABASE_BINARY_RUNRSF
    100000         0
$
$ Cross-reference summary for SET_NODE 1
$ ---------------------------------------
$ DATABASE_HISTORY <No label>
$
*SET_NODE_LIST
         1       0.0       0.0       0.0       0.0
```

```
      ...
      1264       1726       1278       1581       1670          2        509        253
$
$
*DATABASE_HISTORY_NODE_SET
         1
$
$ Cross-reference summary for SET_SHELL 1
$ ---------------------------------------
$ DATABASE_HISTORY <No label>
$
*SET_SHELL_LIST
         1        0.0        0.0        0.0        0.0
      1242       1241       1240       1239       1238       1237       1236       1235
      1197       1233       1186       1207
$
$
*DATABASE_HISTORY_SHELL_SET
         1
$
$ Cross-reference summary for SET_SOLID 1
$ ---------------------------------------
$ DATABASE_HISTORY <No label>
$
*SET_SOLID
         1
      1009       1001        993        985        977        969        961        953
      1033        552        576        600        929        905        881        857
       385        990       1046        926        658        721        792        664
       785
$
$
*DATABASE_HISTORY_SOLID_SET
         1
$
$
$ ====================
```

```
$ MAT (Material) cards
$ ====================
$
*MAT_ELASTIC
         1    1.0E-9    2.7E-2     0.499       0.0       0.0       0.0
$
*MAT_NULL
         2    1.0E-9   -1.0E10    1.0E-9       0.0       0.0       0.0       0.0
$
*MAT_RIGID
         3   2.15E-9    1300.0      0.28       0.0       0.0       0.0
       1.0       5.0       7.0
         0       0.0       0.0       0.0       0.0       0.0
$
*MAT_ELASTIC
         4   4.4E-10      0.42      0.42       0.0       0.0       0.0
$
$
$
$ ========================
$ EOS (Eqn of state) cards
$ ========================
$
*EOS_GRUNEISEN
         1 1500000.0       0.0       0.0       0.0       0.0       0.0       0.0
       0.0
$
$
$
$ =============
$ SECTION cards
$ =============
$
*SECTION_SHELL
         3         2       0.0         0       0.0       0.0         0         0
       2.0       2.0       2.0       2.0       0.0       0.0
$
```

```
         4         2       0.0         0       0.0       0.0         0         0
       0.1       0.1       0.1       0.1       0.0       0.0
$
*SECTION_SOLID
         1         1         0
$
         2         5         0
$
$
$
$ ==========
$ PART cards
$ ==========
$
*PART
$HMNAME COMPS       1FILL_EL
FILL_EL
         1         1         1         0         0         0         0         0
$
*PART
$HMNAME COMPS       2WATER_EL
WATER_EL
         2         2         2         1         0         0         0         0
$
*PART
$HMNAME COMPS       3COVER3_E
COVER3_E
         3         3         3         0         0         0         0         0
$
*PART
$HMNAME COMPS       4SKIN_EL
SKIN_EL
         4         4         4         0         0         0         0         0
$
$
$
$ ==========
```

```
$ NODE cards
$ ==========
$
*NODE
       1      -28.288544        28.288544              0.0       3       0
     ...
    6840       13.683820        44.405098       -5.0000000       3       0
$
$
$ =============
$ ELEMENT cards
$ =============
$
*ELEMENT_SHELL
    1179       3       45       61       76       46
     ...
    1242       4     2173     2186      218      213
*ELEMENT_SOLID
       1       2        1       19       20        3       77       84      145       85
     ...
    1088       2     2190     2218      222      217     2173     2186      218      213
$
$
$ ============
$ DEFINE cards
$ ============
$
$
*DEFINE_CURVE
$
$ Cross-reference summary for Load-curve 1
$ ------------------------------------------
$
$ Boundary Prescribed Motion <No label>: Velocity vs time
$ X axis : Time                          (Units: Time)
$ Y axis : Prescribed velocity           (Units: Velocity)
$
```

```
$ Usage: Transient analysis
$
         1         0       1.0       1.0       0.0       0.0         0
               0.0          -1342.8000
                    ...
         4.0000000           1147.4000
$
$
$
$ ==============
$ BOUNDARY cards
$ ==============
$
*BOUNDARY_PRESCRIBED_MOTION_RIGID
         3         1         0         1       0.0         0       0.0       0.0
$
$
$ =============
$ INITIAL cards
$ =============
$
*INITIAL_VELOCITY_GENERATION
         0         0       0.0   -1342.8       0.0       0.0
       0.0       0.0       0.0       0.0       0.0       0.0         0
$
$
$ =========
$ ALE cards
$ =========
$
*ALE_REFERENCE_SYSTEM_GROUP
         1         0         5         1         0         0         0         0
       0.0       0.0       0.0       0.0       0.0
*ALE_REFERENCE_SYSTEM_NODE
         1
       534       608       300         0         0         0         0         0
         0         0         0         0
```

```
$
$
$ =========
$ SET cards
$ =========
$
$
$ Cross-reference summary for SET_PART 1
$ ---------------------------------------
$ ALE <No label>
$
*SET_PART_LIST
         1       0.0       0.0       0.0       0.0
         2
$
$
*END
```

L.3. EULERIAN MODEL

```
*KEYWORD
$
*TITLE
$
$ =============
$ CONTROL cards
$ =============
$
*CONTROL_ALE
         2         1         2      -1.0       0.0       0.0       0.0       0.0
       0.0       0.0       0.0       0.0       0.0         0       0.0         0
*CONTROL_TERMINATION
       4.0         0       0.0       0.0       0.0
*CONTROL_TIMESTEP
       0.0      0.67         0       0.0       0.0         0         0         0
$
$
$ ==============
$ DATABASE cards
$ ==============
$
*DATABASE_BINARY_D3PLOT
    2.5E-2         0         0         0
*DATABASE_BINARY_D3THDT
    2.5E-2         0
*DATABASE_BINARY_RUNRSF
   1000000         0
*DATABASE_EXTENT_BINARY
         0         0         3         1         1         1         1         1
         0         0         0         0         0         0         0
$
$ Cross-reference summary for SET_NODE 1
$ ---------------------------------------
$ DATABASE_HISTORY <No label>
```

```
$
*SET_NODE_LIST
         1       0.0       0.0       0.0       0.0
      ...
      3400      1449      1536
$
$
*DATABASE_HISTORY_NODE_SET
         1
$
$ Cross-reference summary for SET_SHELL 1
$ ---------------------------------------
$ DATABASE_HISTORY <No label>
$
*SET_SHELL_LIST
         1       0.0       0.0       0.0       0.0
       769       770       771       772       773       774       775       776
       777       778       779       780       706       705       752       751
$
$
*DATABASE_HISTORY_SHELL_SET
         1
$
$ Cross-reference summary for SET_SOLID 1
$ ---------------------------------------
$ DATABASE_HISTORY <No label>
$
*SET_SOLID
         1
      1593      1599      1605      1611      1617      1623      1641      1352
      1370      1382      1527      1539      1557      1575      1251      1449
      1413      1491      1652      1574      1418      1496      1614
$
$
*DATABASE_HISTORY_SOLID_SET
         1
$
```

```
$
$ ====================
$ MAT (Material) cards
$ ====================
$
*MAT_ELASTIC
         1    1.0E-9    2.7E-2     0.499       0.0       0.0       0.0
$
*MAT_NULL
         2    1.0E-9-1000000.0    1.0E-3       0.0       0.0       0.0       0.0
$
*MAT_ELASTIC
         3    1.0E-9       0.0       0.0       0.0       0.0       0.0
$
*MAT_RIGID
         4   2.15E-9    1300.0      0.28       0.0       0.0       0.0
       1.0       5.0       7.0
         0       0.0       0.0       0.0       0.0       0.0
$
*MAT_ELASTIC
         5   4.4E-10      0.42      0.42       0.0       0.0       0.0
$
$
$
$ ========================
$ EOS (Eqn of state) cards
$ ========================
$
*EOS_GRUNEISEN
         1 1500000.0       0.0       0.0       0.0       0.0       0.0       0.0
       0.0
$
$
$
$ =============
$ SECTION cards
$ =============
```

```
$
*SECTION_SHELL
         4         2       0.0         0       0.0       0.0         0         0
       2.0       2.0       2.0       2.0       0.0       0.0
$
         5         2       0.0         0       0.0       0.0         0         0
       1.0       1.0       1.0       1.0       0.0       0.0
$
*SECTION_SOLID
         1         0         0
$
         3         0         0
$
*SECTION_SOLID_ALE
         2        12         0
       0.0       0.0       0.0       0.0       0.0       0.0       0.0
$
$
$ ==========
$ PART cards
$ ==========
$
*PART
$HMNAME COMPS       1BRAIN_EL
BRAIN_EL
         1         1         1         0         0         0         0         0
$
*PART
$HMNAME COMPS       2WATER_EL
WATER_EL
         2         2         2         1         0         0         0         0
$
*PART
$HMNAME COMPS       3VOID_OUT
VOID_OUT
         3         2         2         1         0         0         0         0
```

```
$
*PART
$HMNAME COMPS        4COVER_EL
COVER_EL
         4          4          4          0          0          0          0          0
$
*PART
$HMNAME COMPS        5VOID_IN
VOID_IN
         5          2          2          1          0          0          0          0
$
*PART
$HMNAME COMPS        6SKIN_EL
SKIN_EL
         6          5          5          0          0          0          0          0
$
$
$
$ ==========
$ NODE cards
$ ==========
$
*NODE
       1      -28.288544        28.288544              0.0        3        0
      ...
    3512       12.036694        43.942543       -5.0000000        3        0
$
$
$ =============
$ ELEMENT cards
$ =============
$
*ELEMENT_SHELL
     689        4     1431     1433     1474     1473
      ...
     780        6     1593     1431     1473     1614
*ELEMENT_SOLID
```

```
       1       2       1      15      16       3      59      64      98      65
      ...
    1652       1    3445    3460    2616    2611    2943    2948    2567    2553
$
$
$ ============
$ DEFINE cards
$ ============
$
$
*DEFINE_CURVE
$
$ Cross-reference summary for Load-curve 1
$ ------------------------------------------
$
$ Usage: Transient analysis
$
         1         0       1.0       1.0       0.0       0.0         0
                 0.0                500.00000
           9.9999998E-3                   0.0
$
$
*DEFINE_CURVE
$
$ Cross-reference summary for Load-curve 2
$ ------------------------------------------
$
$ Boundary Prescribed Motion <No label>: Velocity vs time
$ X axis : Time                          (Units: Time)
$ Y axis : Prescribed velocity           (Units: Velocity)
$
$ Usage: Transient analysis
$
         2         0       1.0       1.0       0.0       0.0         0
                 0.0           -1342.8000
                              ...
             4.0000000            1147.4000
```

```
$
$
$
$ ==============
$ BOUNDARY cards
$ ==============
$
*BOUNDARY_PRESCRIBED_MOTION_RIGID
         4          1          0          2        0.0          0        0.0        0.0
$
$
$ =================
$ CONSTRAINED cards
$ =================
$
*CONSTRAINED_LAGRANGE_IN_SOLID
         2          1          0          0          4          4          2          1
       0.0        0.0          0        0.0        0.0          0          0        0.0
       0.0        0.0        0.0          0        0.1          0
$
$ Cross-reference summary for SET_PART 1
$ --------------------------------------
$ CONSTRAINED_LAGRANGE_IN_SOLID <No label>
$ CONSTRAINED_LAGRANGE_IN_SOLID <No label>
$ ALE <No label>
$
*SET_PART_LIST_TITLE
FLUID
         1        0.0        0.0        0.0        0.0
         2          3          5
$
$
$ Cross-reference summary for SET_PART 2
$ --------------------------------------
$ CONSTRAINED_LAGRANGE_IN_SOLID <No label>
$
*SET_PART_LIST_TITLE
```

```
COVER
         2       0.0       0.0       0.0       0.0
         4         6
$
*CONSTRAINED_LAGRANGE_IN_SOLID
         3         1         0         0         4         4         2         1
       0.0       0.0         0       0.0       0.0         0         0       0.0
       0.0       0.0       0.0         0       0.1         0
$
$ Cross-reference summary for SET_PART 3
$ ---------------------------------------
$ CONSTRAINED_LAGRANGE_IN_SOLID <No label>
$
*SET_PART_LIST_TITLE
BRAIN
         3       0.0       0.0       0.0       0.0
         1
$
$
$
$ =============
$ INITIAL cards
$ =============
$
*INITIAL_VELOCITY_GENERATION
         0         0       0.0   -1342.8       0.0       0.0
       0.0       0.0       0.0       0.0       0.0       0.0         0
*INITIAL_VOID_PART
         3
         5
$
$
$ =========
$ ALE cards
$ =========
$
*ALE_REFERENCE_SYSTEM_GROUP
```

```
         1         0         5         1         0         0         0         0
       0.0       0.0       0.0       0.0       0.0
*ALE_REFERENCE_SYSTEM_NODE
         1
      1432      1524      1533         0         0         0         0         0
         0         0         0         0
$
$
$ =========
$ SET cards
$ =========
$
$
*END
```